

Non-van der Waals Heterostructures

Anastasiia Nihei,^{1,2} Tom Barnowsky,^{1,2} and Rico Friedrich^{1,2,3,*}

¹*Theoretical Chemistry, Technische Universität Dresden, 01062 Dresden, Germany*

²*Institute of Ion Beam Physics and Materials Research,
Helmholtz-Zentrum Dresden-Rossendorf, 01328 Dresden, Germany*

³*Center for Extreme Materials, Duke University, Durham, NC 27708, USA*

(Dated: March 18, 2025)

Beyond the study of individual materials, their interfaces and arising functionality are crucial enablers of fundamental science and technological applications. Recently, the arena of two-dimensional (2D) materials was extended to so-called non-van der Waals (non-vdW) compounds derived from strongly bonded non-layered bulk crystals. These nanosystems with their active surfaces complement now – through their chemically bonded heterostructure (HS) interfaces – the established space of weakly interacting vdW HSs. Here, we study a wide range of 55 candidate non-vdW HSs with autonomous density functional calculations and find that the resulting interfacial chemical hybridization and bonding is *the* key factor determining their electronic and magnetic properties. It gives rise to the formation of hybrid interface bands, strong magnetic coupling, and substantial electronic as well as magnetic moiré surface property modulations upon twisting. Our work thus provides a significant step towards charting the new interface class of non-vdW HSs.

Keywords: 2D materials, non-van der Waals compounds, heterostructures, interface design, magnetism, data-driven research, computational materials science, high-throughput computing

Interfaces of materials are at the heart of technologies by creating decisive functionalities such as in electronics, catalysis, batteries, and data storage media – or as Herbert Kroemer put it: “the interface is the device” [1]. In addition to lateral junctions [2, 3], stacked two-dimensional (2D) materials in the form of both homobilayers [4] and heterostructures (HSs) have emerged as a versatile implementation of functional interface design. They can host unique excitonic effects, special (tunneling) transport behavior as well as optical, plasmonic, magnetic, topological, and optoelectronic properties [5–9]. Particular progress has been made towards reliable and scalable manufacturing of HSs down to atomically sharp interfaces both from top down and bottom up growth approaches [5, 6, 10–13].

The twist angle between stacked sheets has been pointed out as an important additional degree of freedom. The interfacing can then bring about qualitatively new and even at first sight unexpected features for which the observation of unconventional superconductivity in twisted bilayer graphene is a striking example [14]. Beyond that long-range moiré patterns in large twisted bilayers of MoS₂ can, for instance, initiate emerging features in the band structures resembling signatures of graphene or hexagonal boron nitride albeit at a much smaller dispersive energy scale [15].

The zoo of traditional 2D systems derived from layered crystals bonded by weak van der Waals (vdW) forces [16–18] provides a range of possibilities for the associated vdW HSs. Nevertheless, the weak dispersive interactions between the layers in the stack pose also a restriction as the corresponding interlayer interaction energy is intrinsically low.

The recently discovered new class of non-van der Waals 2D materials [19, 20] derived from strongly bonded non-layered bulk crystals offers qualitatively new opportunities. A decent amount of representatives has already been found by both top down exfoliation as well as more recently also bottom up growth approaches [21–42] supplemented by data-driven computational studies suggesting a few dozen additional candidates [43–45].

The advent of these systems came as a surprise as it was intuitively thought that chemically bonded materials cannot be exfoliated easily. Their active surfaces [46] resulting from the dangling bonds and surface states generated during exfoliation give now rise to different behavior compared to traditional 2D systems. As such, they have already been demonstrated to show exceptional catalytic activity [21] as well as substantial surface magnetism with almost perfect spin polarization [43]. These (re-)active surfaces of non-vdW 2D materials foreshadow now also a qualitatively new behavior for their HS interfaces: hybridization of electronic states and interfacial chemical bonding between the 2D components can lead to strong coupling inaccessible in vdW HSs.

Remarkably, strong interfacial coupling is already known from thin film oxide interfaces giving rise to emerging metallicity [47], superconductivity [48], and magnetism [49] due to new interfacial states such as 2D electron gases [50–55]. These can also lead to a localization of states tuning for instance the conductivity or magnetic ordering. An encouraging strong indication that also specific rotations can be achieved is the recent report of experimentally realized stacked and twisted oxide films [56]. Well defined chemical bonds were detected at the interface and even signatures of emerging moiré patterns were identified. While these findings were obtained with oxide films of several ten nanometer thickness, the interfacial interactions are still strongly confined to the 2D limit.

* rico.friedrich@tu-dresden.de

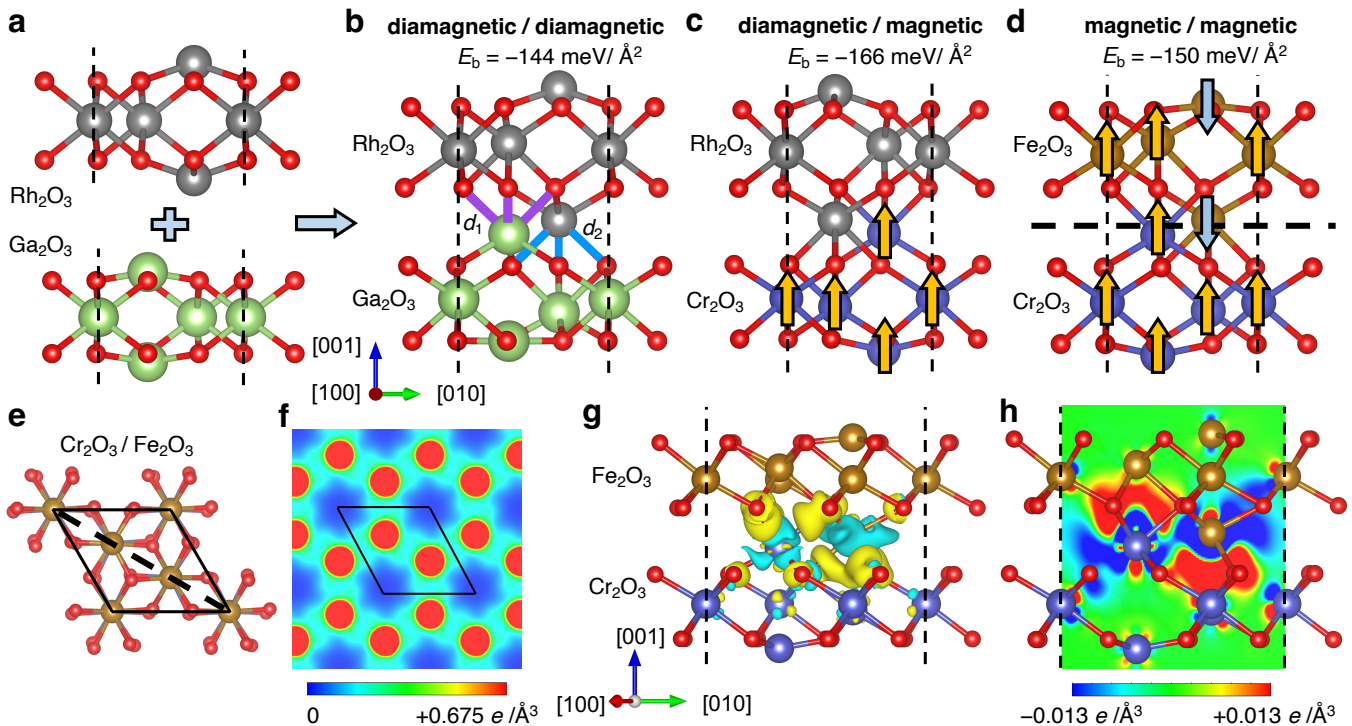


FIG. 1. **Interfacial bonding in non-vdW HSs.** HSs are built from stacking and matching non-vdW 2D sheets (a) leading to interfacial bonding (highlighted in purple and light blue) in optimized structures for combinations of two diamagnetic (b), a diamagnetic and a magnetic (c), and two magnetic (d) systems. Distances d_1 and d_2 of interfacial bonds are marked in (b). Arrows indicate moments in magnetic layers. Binding energies E_b are also indicated. The compass indicating crystal directions refers to all top row subfigures. (e) Top view of the representative $\text{Cr}_2\text{O}_3/\text{Fe}_2\text{O}_3$ HS. (f) Top view of the charge density in an extended region on the plane indicated by the black dashed line in (d). The unit cell is given by the black frame. (g) Isosurface plot of the charge density difference for $\text{Cr}_2\text{O}_3/\text{Fe}_2\text{O}_3$ with charge gain/loss indicated by yellow/bluish parts (isosurface value: $\pm 0.027 e/\text{\AA}^3$). (h) Cut through the charge density difference on the (110) plane indicated by the black dashed line in (e). The compass in (g) refers also to (h). Dashed vertical black lines represent unit cell boundaries. Colors: O, red; Ga, light green; Rh, gray; Cr, blue; Fe, gold.

Here, we perform an exhaustive computational investigation of a large set of over 50 such non-vdW HS candidates. Based on density functional theory (DFT) we demonstrate that their properties and potential active electronic and magnetic functionality is determined by the strong interfacial interactions. Study of the optimized structures, densities, and interlayer binding energies clearly indicates substantial interfacial bonding for most systems stemming from ionic and covalent contributions. These strong interactions also give rise to the formation of hybrid interface bands with sizable contributions on both 2D components. The interfacial chemical bonding mediates furthermore a strong magnetic coupling that stabilizes specific magnetic configurations. Eventually, also twisted non-vdW HSs can be generated exhibiting characteristic local atomic (moiré) patterns that lead to long-range signatures in the surface charge and magnetization densities. Our large-scale screening showcases the rich variety of features to be expected from non-vdW HSs. It thus offers the prospect of converging major concepts of 2D materials and oxide thin films research.

I. RESULTS

The HSs are built out of 36 non-van der Waals 2D materials outlined previously [43, 44] (see Fig. 1(a)). The entries (V_2O_3 and Ti_2O_3) exhibiting broken symmetry are excluded so that all 2D materials have the same hexagonal structure as the experimentally realized hematene [21] and ilmenene [22] systems. Out of the remaining 34 single layers, a total of 561 combinations can be formed. During the search for matching cell sizes at different twist angles (for details see Methods section), the total strain is limited to at max 2 % as larger values are considered generally unfeasible, resulting in the generation of in total 1217 HSs.

Here, we are interested in outlining the fundamental effects arising from the strong interfacial interactions in these non-vdW HSs. Hence we focus first on the smallest cells possible with a zero degree twist angle, aligned in such a way that cations do not face each other, yielding a total of 53 systems. These HSs are further categorized into three groups: combinations of (i) two diamagnetic layers (21 HSs, example structure in Fig. 1(b)),

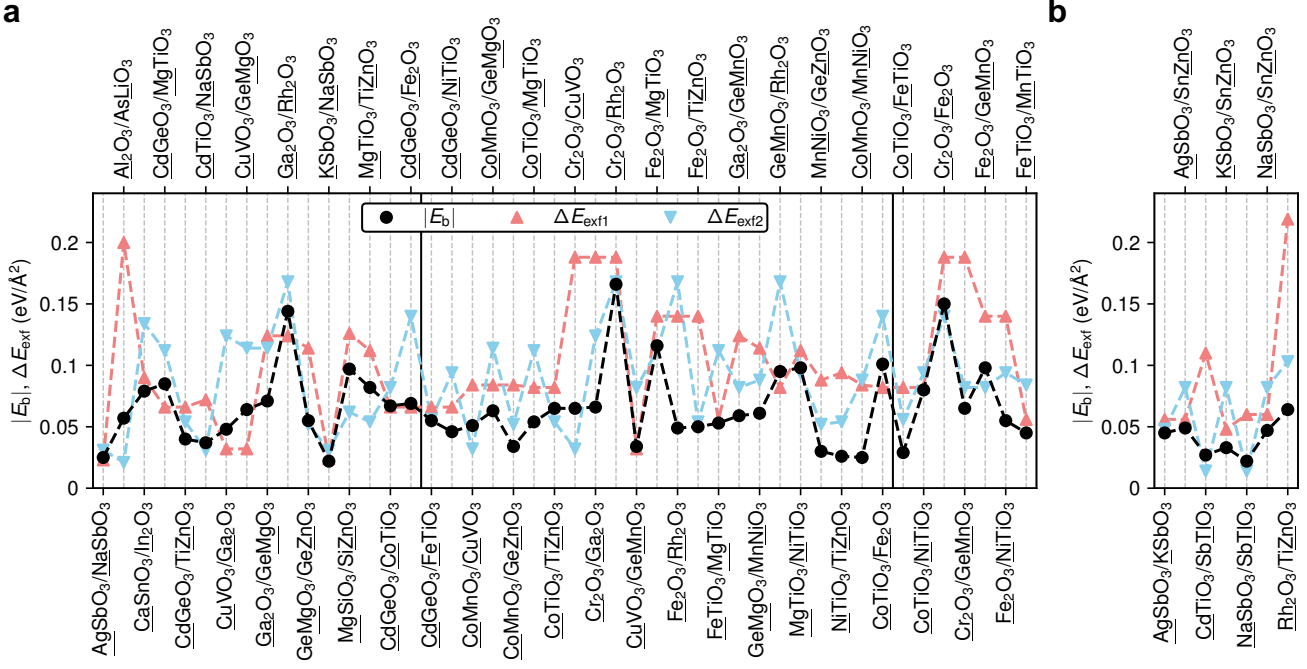


FIG. 2. **Binding energies.** Comparison of HS binding energies and exfoliation energies of the individual 2D components calculated with plain PBE+ U (a) and with D3 dispersion correction (b). $\Delta E_{\text{exf}1/2}$ refers to the exfoliation energy of the first/second component in the formula of the HS. Vertical black lines separate results for the different groups. As a guide to the reader, elements at the surface of the isolated 2D sheets are underlined. These are then on one side located at the interface of the respective HS.

(ii) a diamagnetic and a magnetic layer with a sizeable magnetic moment for at least one cation species (23 HSs, Fig. 1(c)), and (iii) two magnetic layers (9 HSs, Fig. 1(d)). A representative top view of $\text{Cr}_2\text{O}_3/\text{Fe}_2\text{O}_3$ is presented in Fig. 1(e). Table I lists the nominal strain for all systems as obtained from the initial HS setup and the “relaxed strain” of the optimized structure. The second varies from the nominal value due to specific relaxations for each system albeit not strongly in most cases. Note that the tabulated total strain is the sum of the (tensile and compressive) strains on both 2D materials. Analysis of the relaxed strain on each individual 2D component showed that the maximum value per spatial direction is 1.25% for TiZnO_3 in $\text{Rh}_2\text{O}_3/\text{TiZnO}_3$.

Interfacial bonding: Upon relaxation of the structures, the individual 2D layers bind strongly (highlighted interfacial bonds in Fig. 1(b)). This is clearly visible in all representative optimized geometries in Fig. 1(b-d). The bond formation at the interface indicates chemical compatibility and enhances the overall stability of the HS beyond traditional vdW stacks crucially determining its properties. This chemical bonding can already be detected for the example of $\text{Cr}_2\text{O}_3/\text{Fe}_2\text{O}_3$ from an inspection of the charge density on the interfacial plane provided in Fig. 1(f). While the main charge is concentrated at the transition metals, there is also significant density in the regions between these centers indicative of electronic delocalization and coupling. An even more insightful picture emerges from the charge density difference computed as

the change of the electronic density between the HS and its isolated 2D components with the same atomic positions (see Methods section for details). The isosurface/cut through the density difference in Fig. 1(g)/(h) clearly indicates that, upon interfacial interaction, charge is transferred from around the central cations towards the neighboring oxygens of the other 2D sheet with which bonding occurs. A comparison of the charge density differences for all the three HSs in Fig. 1(b-d) is presented in section I. of the supporting information (SI).

Binding energies: To quantify the interfacial interaction strength, the binding energy E_b is computed as the difference in total energy between the HS and the isolated relaxed 2D systems normalized per area. The binding energy has a negative sign as energy is gained upon bonding the individual sheets. The values of all systems are included in Table I and the absolute numbers in comparison to the exfoliation energies of the respective 2D component sheets [43, 44] are presented in Fig. 2 with a separation according to the three groups. The exfoliation energy ΔE_{exf} is the (positive) energy required to delaminate a 2D material of given thickness from the surface of its bulk parent material which has also been proven to coincide with the interlayer binding energy of the bulk [57].

The energy gain resulting from the bonding within the HS ranges from only a few $\text{meV}/\text{\AA}^2$ in a small number of cases to $-166 \text{ meV}/\text{\AA}^2$ ($\text{Cr}_2\text{O}_3/\text{Rh}_2\text{O}_3$), *i.e.*, for most systems (around two third), a large binding energy of at least around $-50 \text{ meV}/\text{\AA}^2$ is ob-

TABLE I. **Key properties of non-vdW HSs.** List of HSs with nominal (relaxed) strain, binding energy E_b per area and per bond, bond lengths at the interface (d_1/d_2 is the interfacial cation-O bond length of the first/second component in the formula of the HS), band gaps, and interfacial magnetic coupling energies. For the entries marked by ‘*’, the properties computed for the structure optimized with D3 dispersion correction are reported. Elements at the surface of the isolated 2D sheets are underlined. These are then on one side located at the interface of the respective HS.

System	Strain (%) (Relaxed)	E_b per Area (meV/Å ²)	E_b per bond (meV)	d_1 (Å)	d_2 (Å)	Band gap (eV)	E_c (meV)
diamagnetic/diamagnetic combinations							
AgSbO ₃ / <u>K</u> SbO ₃ *	0.06 (0.71)	-45	-190	2.86	2.82	1.79	—
AgSbO ₃ / <u>Na</u> SbO ₃	1.92 (1.81)	-25	-107	2.73	2.73	1.94	—
AgSbO ₃ / <u>SnZn</u> O ₃ *	0.04 (1.59)	-49	-210	2.65	2.98	1.44	—
<u>Al</u> ₂ O ₃ / <u>AsLi</u> O ₃	0.29 (1.18)	-57	-200	2.45	2.16	1.73	—
<u>Ca</u> SnO ₃ / <u>In</u> ₂ O ₃	0.07 (2.18)	-79	-363	2.43	2.52	1.33	—
<u>Cd</u> GeO ₃ / <u>Mg</u> TiO ₃	0.51 (0.85)	-85	-337	2.44	2.31	2.11	—
<u>Cd</u> GeO ₃ / <u>TiZn</u> O ₃	0.91 (2.09)	-40	-155	2.52	2.48	2.30	—
<u>Cd</u> TiO ₃ / <u>Na</u> SbO ₃	1.10 (1.76)	-37	-153	2.80	2.53	1.73	—
<u>Cd</u> TiO ₃ / <u>SbTi</u> O ₃ *	0.39 (0.81)	-27	-112	4.13	3.32	2.24	—
<u>Cu</u> VO ₃ / <u>Ga</u> ₂ O ₃	1.12 (2.12)	-48	-178	2.25	2.36	0.54	—
<u>Cu</u> VO ₃ / <u>GeMg</u> O ₃	0.64 (2.52)	-64	-238	2.32	2.30	0.67	—
<u>Ga</u> ₂ O ₃ / <u>GeMg</u> O ₃	1.76 (2.47)	-71	-263	2.41	2.23	2.41	—
<u>Ga</u> ₂ O ₃ / <u>Rh</u> ₂ O ₃	0.93 (0.93)	-144	-547	2.08	2.12	1.22	—
<u>GeMg</u> O ₃ / <u>GeZn</u> O ₃	1.50 (2.31)	-55	-200	2.33	2.37	2.70	—
<u>KSb</u> O ₃ / <u>Na</u> SbO ₃	1.92 (1.93)	-22	-93	2.85	2.93	2.39	—
<u>KSb</u> O ₃ / <u>SnZn</u> O ₃ *	0.03 (0.70)	-33	-143	2.85	3.36	0.99	—
<u>Mg</u> SiO ₃ / <u>SiZn</u> O ₃	1.43 (1.43)	-97	-325	2.22	2.25	3.98	—
<u>Mg</u> TiO ₃ / <u>TiZn</u> O ₃	1.42 (2.58)	-82	-320	2.23	2.26	3.42	—
<u>Na</u> SbO ₃ / <u>SbTi</u> O ₃ *	0.71 (0.84)	-22	-94	3.56	3.17	2.21	—
<u>Na</u> SbO ₃ / <u>SnZn</u> O ₃ *	1.88 (2.18)	-47	-197	2.63	2.99	1.82	—
<u>Rh</u> ₂ O ₃ / <u>TiZn</u> O ₃ *	1.99 (2.50)	-64	-244	2.45	2.34	0.88	—
diamagnetic/magnetic combinations							
<u>Cd</u> GeO ₃ / <u>Co</u> TiO ₃	0.68 (1.52)	-67	-262	2.45	2.37	2.09	—
<u>Cd</u> GeO ₃ / <u>Fe</u> ₂ O ₃	1.30 (1.30)	-69	-271	3.86	2.39	0.91	—
<u>Cd</u> GeO ₃ / <u>Fe</u> TiO ₃	1.78 (1.78)	-55	-217	2.46	2.40	1.23	—
<u>Cd</u> GeO ₃ / <u>Ni</u> TiO ₃	0.53 (2.44)	-46	-177	2.51	2.46	2.25	—
<u>Co</u> MnO ₃ / <u>Cu</u> VO ₃	1.15 (2.63)	-51	-186	2.35	2.28	0.44	—
<u>Co</u> MnO ₃ / <u>GeMg</u> O ₃	0.51 (2.15)	-63	-234	2.44	2.37	1.64	—
<u>Co</u> MnO ₃ / <u>GeZn</u> O ₃	0.99 (2.13)	-34	-126	2.51	2.48	1.73	—
<u>Co</u> TiO ₃ / <u>Mg</u> TiO ₃	0.18 (3.12)	-54	-210	2.48	2.40	2.89	—
<u>Co</u> TiO ₃ / <u>TiZn</u> O ₃	1.60 (2.78)	-65	-252	2.26	2.25	3.11	—
<u>Cr</u> ₂ O ₃ / <u>Cu</u> VO ₃	1.72 (3.08)	-65	-241	2.24	2.21	0.07	—
<u>Cr</u> ₂ O ₃ / <u>Ga</u> ₂ O ₃	0.60 (4.00)	-66	-248	2.19	2.19	1.52	—
<u>Cr</u> ₂ O ₃ / <u>Rh</u> ₂ O ₃	0.33 (0.97)	-166	-631	2.08	2.11	1.16	—
<u>Cu</u> VO ₃ / <u>GeMn</u> O ₃	1.76 (2.02)	-34	-126	2.45	2.53	0.82	—
<u>Fe</u> ₂ O ₃ / <u>Mg</u> TiO ₃	1.81 (1.80)	-116	-454	2.27	2.17	1.65	—
<u>Fe</u> ₂ O ₃ / <u>Rh</u> ₂ O ₃	1.60 (1.77)	-49	-186	2.18	2.28	0.95	—
<u>Fe</u> ₂ O ₃ / <u>TiZn</u> O ₃	0.39 (3.00)	-50	-192	2.34	2.26	1.59	—
<u>Fe</u> TiO ₃ / <u>Mg</u> TiO ₃	1.28 (3.25)	-53	-208	2.35	2.30	2.64	—
<u>Ga</u> ₂ O ₃ / <u>GeMn</u> O ₃	0.64 (2.09)	-59	-223	2.46	2.33	1.73	—
<u>GeMg</u> O ₃ / <u>MnNi</u> O ₃	1.85 (2.52)	-61	-221	2.31	2.37	1.78	—
<u>GeMn</u> O ₃ / <u>Rh</u> ₂ O ₃	0.30 (0.47)	-95	-361	2.21	2.26	1.01	—
<u>Mg</u> TiO ₃ / <u>Ni</u> TiO ₃	1.04 (2.99)	-98	-381	2.20	2.22	2.84	—
<u>MnNi</u> O ₃ / <u>GeZn</u> O ₃	0.35 (2.27)	-30	-110	2.44	2.41	1.86	—
<u>Ni</u> TiO ₃ / <u>TiZn</u> O ₃	0.38 (3.33)	-26	-100	2.44	2.44	2.83	—
magnetic/magnetic combinations							
<u>Co</u> MnO ₃ / <u>MnNi</u> O ₃	1.34 (1.34)	-25	-94	2.46	2.31	0.88	-72
<u>Co</u> TiO ₃ / <u>Fe</u> ₂ O ₃	1.99 (2.09)	-101	-392	2.19	2.25	1.59	+30
<u>Co</u> TiO ₃ / <u>Fe</u> TiO ₃	1.10 (2.95)	-29	-112	2.51	2.49	2.31	-7
<u>Co</u> TiO ₃ / <u>Ni</u> TiO ₃	1.22 (3.15)	-80	-310	2.23	2.21	2.77	+13
<u>Cr</u> ₂ O ₃ / <u>Fe</u> ₂ O ₃	1.93 (1.92)	-150	-575	2.10	2.13	0.95	-74
<u>Cr</u> ₂ O ₃ / <u>GeMn</u> O ₃	0.06 (2.91)	-65	-244	2.39	2.31	1.30	-61
<u>Fe</u> ₂ O ₃ / <u>GeMn</u> O ₃	1.90 (1.89)	-98	-376	2.32	2.26	1.52	+10
<u>Fe</u> ₂ O ₃ / <u>Ni</u> TiO ₃	0.77 (3.27)	-55	-212	2.36	2.32	1.62	+15
<u>Fe</u> TiO ₃ / <u>Mn</u> TiO ₃	1.09 (3.26)	-45	-177	2.39	2.38	2.59	-27

served. Five systems even have an absolute E_b exceeding $100 \text{ meV}/\text{\AA}^2$: $\text{Ga}_2\text{O}_3/\text{Rh}_2\text{O}_3$, $\text{Cr}_2\text{O}_3/\text{Rh}_2\text{O}_3$, $\text{Fe}_2\text{O}_3/\text{MgTiO}_3$, $\text{CoTiO}_3/\text{Fe}_2\text{O}_3$, and $\text{Cr}_2\text{O}_3/\text{Fe}_2\text{O}_3$. This energy scale is much larger as in case of vdW bonded layers. For example, the absolute binding energy of a vdW bonded graphene homobilayer is computed to $16 \text{ meV}/\text{\AA}^2$ which is in the same well-known energy range as typical exfoliation energies of vdW bonded (layered) materials [16, 18, 58]. An exfoliation or absolute binding energy of $\sim 20 \text{ meV}/\text{\AA}^2$ was even pointed out to be a universal value for layered systems [58].

The large E_b of non-vdW HSs stem from covalent and ionic interactions at the interface between the 2D sheets. To underscore this point, we also compute average binding energies per bond at the interface. As depicted in Figs. 1(b)-(d), for essentially all structures, six new cation-oxygen bonds are formed between the surface cation of one component and O^{2-} anions of the other component in the HS. As outlined in Table I, these values per bond are in almost all cases on the order of several hundred meV reaching the highest energy gain again for $\text{Cr}_2\text{O}_3/\text{Rh}_2\text{O}_3$ with -631 meV indicative of ionic and/or covalent interactions.

Also the individual interfacial bond lengths d_1 and d_2 labelled in Fig. 1(b) for each cation-O pair included in Table I corroborate this picture. These are almost exclusively between 2 and 3 \AA and hence typical for covalent and ionic bonds for the elements involved.

When compared to the exfoliation energies of their 2D components in Fig. 2, the absolute binding energies of the HSs are generally on the same order of magnitude with a slight tendency towards lower values. Thus, most HSs are bound about as strongly as each of the components is bound to its respective bulk parent compound. There are, however, a few cases where the coupling in the HS is significantly smaller for which $\text{Fe}_2\text{O}_3/\text{Rh}_2\text{O}_3$ is a representative example with its absolute E_b of $49 \text{ meV}/\text{\AA}^2$ being about $90 \text{ meV}/\text{\AA}^2$ smaller than the lower of the two exfoliation energies ($140 \text{ meV}/\text{\AA}^2$ for Fe_2O_3). This signifies that for strong bonding proper electronic compatibility is required.

There are a few HSs in our set with small absolute E_b . For these cases and a few others with higher binding energies, the role of including dispersive interactions via established extensions to DFT (D3 [59], SCAN+rVV10 [60, 61]) is validated with details discussed in section II. in the SI. Based on this analysis, the binding energies of the HSs marked with an asterisk in Table I (the cases where plain PBE+ U yields $|E_b| < 20 \text{ meV}/\text{\AA}^2$) are presented with the dispersion correction as only then proper negative values are obtained. Their binding energies compared to the respective exfoliation energies are presented in Fig. 2(b). Also here the HS shows a tendency towards weaker bonding compared to exfoliation from the parent compounds. In all other cases, negative E_b exceeding the typical energy scale of dispersive interactions [58] is already achieved with plain DFT. For the HSs with high binding energies more negative than $-50 \text{ meV}/\text{\AA}^2$, which we are mostly

interested in, the effect of the dispersion on the energetics and in particular bond lengths is minor as expected and properties can be computed reliably from plain PBE+ U .

The systems including SbTiO_3 deserve a special note. This compound has been classified as a non-vdW 2D material due to its structural similarity to all the other systems in the set with the Tl cations at the surface of the sheet. The bulk form of SbTiO_3 is, however, a layered crystal held together mostly by vdW interactions. This system was therefore pointed out to be in the transition region between vdW and non-vdW materials [44]. Consequently, also in HSs involving SbTiO_3 , interfacial interactions are expected to be weaker than in the other cases with mostly dispersive contributions as corroborated by the small E_b values.

Band gaps and hybrid interface bands: Computed band gaps of the HSs compared to the respective 2D components [43, 44] are presented in Fig. 3(a). The values for all HSs are included in Table I. While absolute band gaps are usually underestimated by standard DFT, PBE+ U values often provide a good semi-quantitative estimate for oxidic systems and in particular the trends between chemically similar systems, *i.e.*, the HS and its 2D components, are typically accurate and insightful. All oxidic non-vdW HSs are hence insulating or semiconducting systems including, however, a two cases ($\text{CoMnO}_3/\text{CuVO}_3$, and $\text{Cr}_2\text{O}_3/\text{CuVO}_3$) with very small band gaps (below 0.5 eV). In general, non-vdW HSs show a trend towards smaller gaps with respect to their 2D components. While this is often related to the specific band alignment, for the present non-vdW stacks, the interfacial bonding creates new hybrid interface bands that can appear in or around the original band gap. A complete list of all band structures and densities of states (DOSs) together with a direct comparison to the bands of the component 2D systems can be found in section III. in the SI. Here, we focus on selected example cases to demonstrate unique features of the new interface class of non-vdW HSs.

Such hybrid interface bands at the edges of the band gap can be found for several systems. In Fig. 3(b,c) this is visible in the band structures with color-coded projection contributions from the atoms of the individual components for the example HSs $\text{CuVO}_3/\text{Ga}_2\text{O}_3$ and $\text{Fe}_2\text{O}_3/\text{Rh}_2\text{O}_3$ (band structures with projection contributions for all systems are also included in section III. in the SI). While in the first case the highest occupied bands show strongly mixed character with respect to contributions from the individual 2D components, the second case depicts a hybridization of the hematene surface state with Rh_2O_3 bands in the conduction band region. To further underline the mixed interfacial character, isosurfaces of the partial charge density of the hybrid bands marked by the red arrows are shown in the insets of Fig. 3(b,c). There, the d -states of the transition metal of one 2D component hybridize with the oxygen p -states of the other with which interfacial bonding occurs. In the second case, contributions at both the interfacial Rh and Fe ions are visible together with ones at the Rh at the top of the

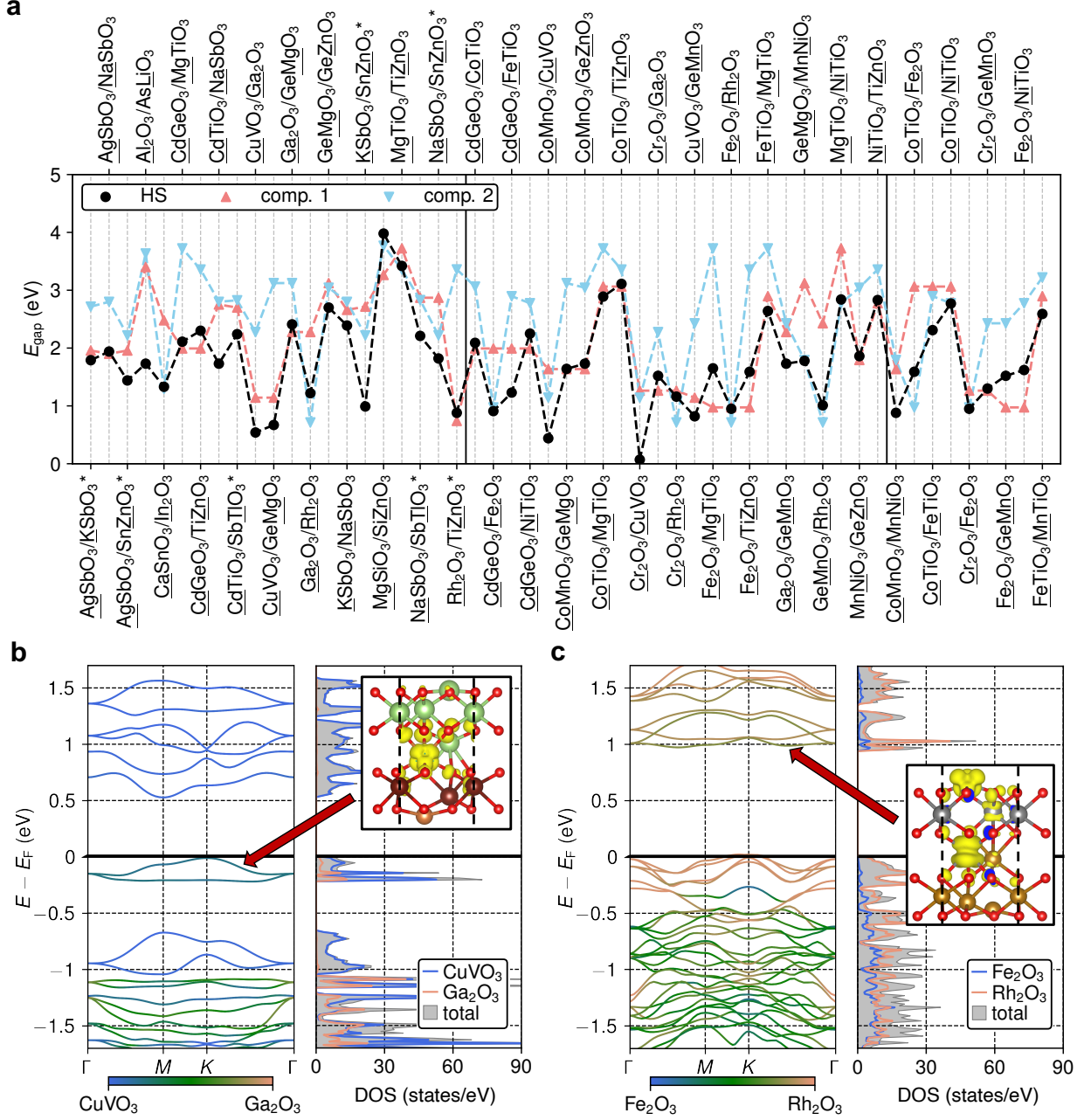


FIG. 3. **Band gaps and hybrid interface bands.** Overview of the band gaps of all HSs in comparison to their isolated 2D components (a). Comp. 1/2 refers to the first/second component in the formula of the HS. For systems marked by ‘*’, the structure is optimized with D3 dispersion correction. The HS band gap is found to vary only slightly (at max by about 0.2 eV) depending on whether the weakly bonded HSs are optimized with or without dispersion correction and hence the results are presented in one combined plot. Elements at the surface of the isolated 2D sheets are underlined. These are then on one side located at the interface of the respective HS. Representative band structures with projection contributions from the atoms of each 2D sheet of $\text{CuVO}_3/\text{Ga}_2\text{O}_3$ (b), and $\text{Fe}_2\text{O}_3/\text{Rh}_2\text{O}_3$ (c) exhibiting hybrid interface bands close to the gap. The insets show isosurfaces of the partial charge density of the hybrid interface bands marked by the respective arrows (isosurface value: $0.034 e/\text{\AA}^3$). Colors: same as in Fig. 1 and V, brown; Cu, orange.

structure. These hybrid interface bands signify that the electronic properties of the HSs are not just a simple superposition of their 2D components but showcase qualitatively new hybrid features.

Interfacial magnetic coupling: The chemical bond-

ing translates now also into a strong interfacial magnetic coupling between the 2D components. Several coupling paths for superexchange between the transition metal ions mediated via oxygen anions are initiated through the interfacial bonds. In HSs from group three composed of two

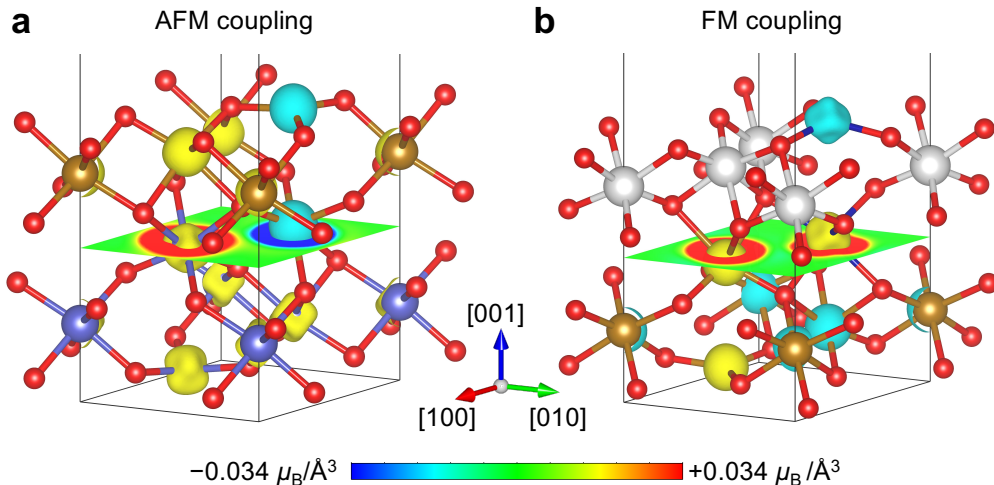


FIG. 4. **Interfacial magnetic coupling.** Perspective view of $\text{Cr}_2\text{O}_3/\text{Fe}_2\text{O}_3$ (a) and $\text{CoTiO}_3/\text{Fe}_2\text{O}_3$ (b) with magnetization density isosurfaces as well as a visualization of this quantity on the interfacial plane indicating AFM and FM interfacial coupling, respectively (isosurface value: $0.88 \mu_B/\text{\AA}^3$). Yellow/bluish parts of the isosurface correspond to positive/negative values. The black line indicates unit cell boundaries. Colors: same as in Fig. 1 and Co, dark blue; Ti, light gray.

magnetic 2D systems, the relative alignment of the magnetic moments at the interface is a key factor determining the magnetic characteristics of the hybrid material. The moments themselves change by less than $0.2 \mu_B$ upon HS formation.

The moments can be aligned or antialigned, *i.e.* the interfacial magnetic coupling can be ferromagnetic (FM) or antiferromagnetic (AFM). As such, calculations with the interfacial moments in both component systems aligned and for all moments of the second component flipped can quantify the strength of the magnetic interactions initiated upon interfacial bonding. The corresponding coupling energies E_c included in Table I computed as the energy difference between aligned and anti-aligned states are substantial on the order of several 10 meV/cell. Positive/negative values indicate preference of the FM/AFM state. We are mainly interested in the interfacial magnetic coupling and thus assume that the magnetic alignment within each 2D component is not affected by formation of the HS. Among the studied nine combinations, four exhibit a preference for FM alignment ($\text{CoTiO}_3/\text{Fe}_2\text{O}_3$, $\text{CoTiO}_3/\text{NiTiO}_3$, $\text{Fe}_2\text{O}_3/\text{GeMnO}_3$, $\text{Fe}_2\text{O}_3/\text{NiTiO}_3$) whereas the five others ($\text{CoMnO}_3/\text{MnNiO}_3$, $\text{CoTiO}_3/\text{FeTiO}_3$, $\text{Cr}_2\text{O}_3/\text{Fe}_2\text{O}_3$, $\text{Cr}_2\text{O}_3/\text{GeMnO}_3$, $\text{FeTiO}_3/\text{MnTiO}_3$) favor an AFM configuration.

For the cases with strongest AFM and FM interfacial couplings ($\text{Cr}_2\text{O}_3/\text{Fe}_2\text{O}_3$ and $\text{CoTiO}_3/\text{Fe}_2\text{O}_3$) represented by the most negative and positive coupling energies of -74 and $+30$ meV/cell, the magnetization densities are visualized in Fig. 4. These clearly indicate the localized positive and negative moments originating from the transition metal d -states. The cut through the magnetisation density at the interfacial planes in Fig. 4 highlights once again the type of magnetic coupling and signifies the strong in-

terfacial spin polarization. Remarkably, these two HSs also show the largest binding energies among all group three systems more negative than -100 meV/ \AA^2 .

Note that deducing a magnetic stability of the interfacial coupling with respect to temperature by comparing these effective coupling energies through the interface to the thermal energy scale is complicated by the fact that several new interfacial couplings are initiated. Moreover the couplings inside the individual 2D components can be weak such that their magnetization will not switch as one entity [44, 46, 62]. Nevertheless, the sizeable E_c underscore the strong interfacial magnetic interactions in non-vdW HSs.

Twisted non-vdW HSs: In addition to minimal commensurate cells, especially the study of twisted HSs and homobilayers of vdW materials has attracted strong interest as they can give rise to novel and enhanced properties such as superconductivity. Such twisted 2D sheets lead to moiré patterns: large-scale interference effects resulting from different local arrangements of the underlying lattices. For 2D nanoscale systems, these are associated with characteristic density and magnetisation density variations that can, for instance, be measured via high resolution electron and scanning tunneling microscopy. Thus, twisted HSs emerge as an appealing platform for discovering and engineering functional materials properties (twistronics) which we anticipate to be even more pronounced in non-vdW HSs due to the significant interfacial chemical interaction. Note that twisted oxide thin film interfaces have recently been experimentally realized by Li and coworkers [56] also hinting at moiré signatures.

Introducing specific twist angles between non-vdW materials can create interfacial structures with both bonded (spatially separated cations) and non-bonded (confronting cations) regions, leading to a combination of weak and

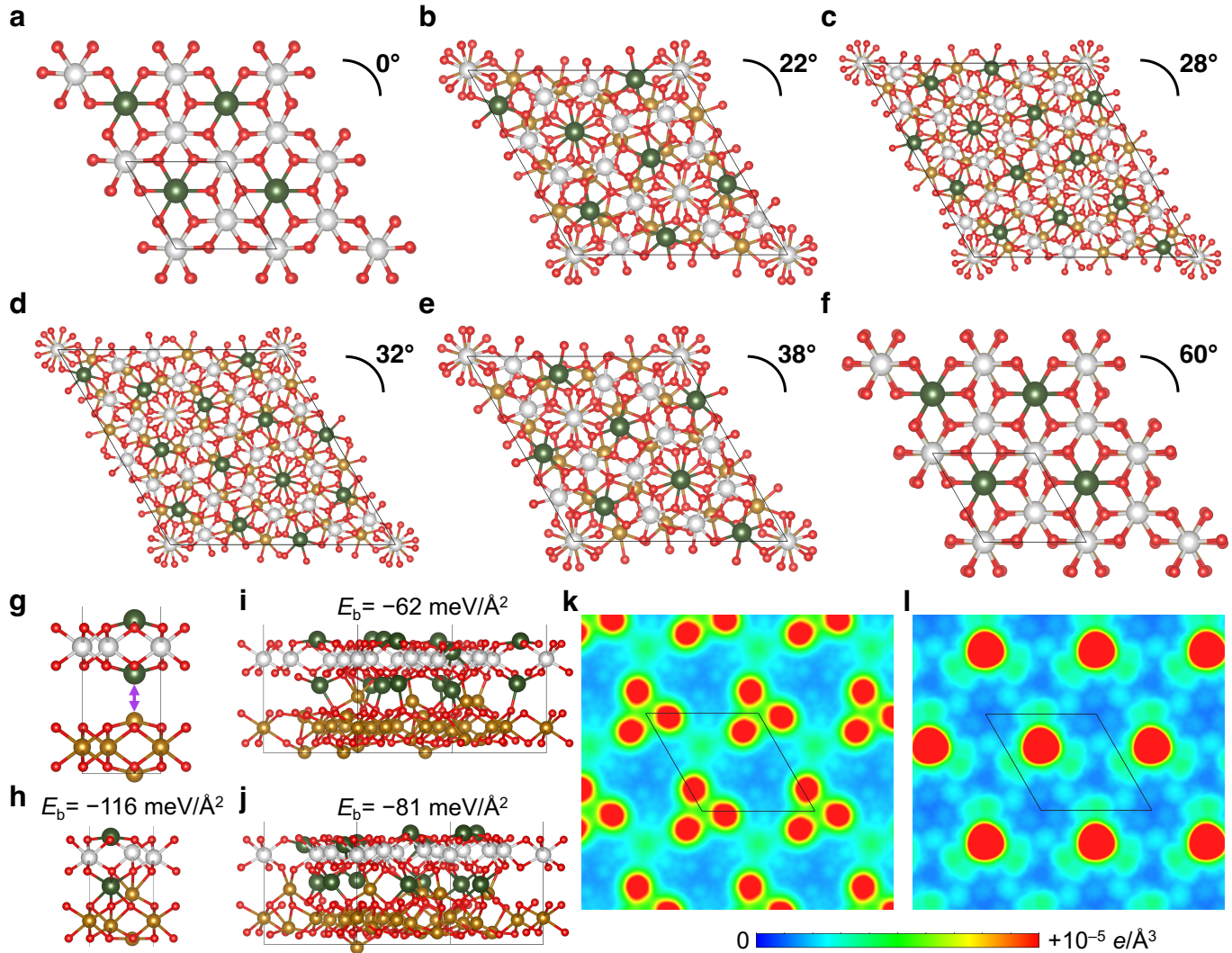


FIG. 5. **Non-vdW HSs at different twist angles.** (a-f) Top views of $\text{Fe}_2\text{O}_3/\text{MgTiO}_3$ HSs obtained at different twist angles showcasing different local atomic moiré patterns for the cases different from 0 and 60°. (g/h) Side view of the initial/relaxed structures with 0/60° twist. (i/j) Side view of the relaxed structures with 22/38° twist. (k/l) Top view of the charge density variation on a plane 3.69/3.15 Å below the bottom surface (below Fe_2O_3) for 22/38°. The unit cell is indicated by the black frame. Colors: same as in Fig. 1 and 4 and Mg, dark green.

strong interfacial interactions. However, these systems often require supercells with thousands of atoms, making them challenging to handle computationally with *ab initio* methods. Here, we give an outlook onto twisted non-vdW HSs by focusing on carefully chosen systems of moderate size generated from the hetbuilder tool that can still be treated within DFT.

In Fig. 5(a-f) representative $\text{Fe}_2\text{O}_3/\text{MgTiO}_3$ HSs (with $\sim 1.81\%$ total nominal strain) obtained from a systematic twist angle scan are depicted. The systems at angles different from 0 and 60° are modelled by larger unit cells containing 140 (22 and 38°) or 260 (28 and 32°) atoms. From a visual inspection of the atomic structures it is already clear that the twisted HSs can give rise to moiré patterns due to the different local stacking arrangements. Note that although the structures in Fig. 5(a) and (f) ap-

pear equivalent from their top views, they differ in the relative arrangement of the 2D components. While for 0° (side view in Fig. 5(g)) cations would face each other leading to a repulsive setup, for 60° (Fig. 5(h)), the arrangement is preferable and bonding can be achieved in a commensurate structure as investigated above.

We explicitly consider the cases in Fig. 5(b) and (e) as electronic structure calculations were performed for them. The side views of the relaxed geometries at 22 and 38° twist in Fig. 5(g) and (h) clearly indicate substantially different interfacial interactions and bonding patterns (the relaxed strain amounts to 1.81 and 2.79%). This strong change of the atomic structure upon twisting is also mirrored by the binding energies. While the commensurate HS at 60° has an E_b of $-116 \text{ meV}/\text{Å}^2$ (see Table I), this value reduces to $-62 \text{ meV}/\text{Å}^2$ at 22°. At 38° the binding

is reinforced to $-81 \text{ meV}/\text{\AA}^2$ hinting at more preferential inter-layer bonds between the 2D components as is also visible when comparing the relaxed side views in Fig. 5(i) and (j). In general, reduced binding energies for larger twisted structures compared to the minimal commensurate cells are found as always less preferential interfacial arrangements need to be accommodated.

To underscore the strong (local) long-range property variation for the different angles, the charge density on a plane below the bottom surface of the HS is visualized in Fig. 5(k/l) for $22/38^\circ$. We focus on the bottom surface density as it depicts the clearest effects. An equivalent analysis for the top surface (above MgTiO_3) can be found in section IV. in the SI. There are distinct angle specific patterns in the densities that correspond to the long-range height variation of the transition metal Fe ions. The pronounced red features can be associated with the Fe atoms sticking out of the HS surface. These substantial moiré like density variations observed are thus strongly structure related and should as such be readily observable with experimental techniques such as electron microscopy and scanning tunneling microscopy. The associated magnetisation density also shows strong long-range angle specific variations as provided in section V. in the SI. These findings prove that non-vdW HSs can also host – once more based on their interfacial interaction – particularly strong local and twist dependent property modulations.

II. DISCUSSION

We have presented an extensive study of the new class of non-vdW HSs by comprehensive computational screening of a large set of 55 representatives. A characteristic signature of these novel interfaces is the strong chemical bonding between the 2D components – a feature distinguishing them from weakly interacting vdW HSs. Based on investigation of the binding energies, the interactions clearly reveal covalent and/or ionic character reaching values of several hundred $\text{meV}/\text{\AA}^2$. The HSs are thus bound almost as strongly as each individual 2D component is to the bulk surface of its parent compound. The strong interfacial interaction leaves also clear signatures in the electronic structure. While all HSs remain insulating as their individual 2D components, in most cases a narrowing of the band gap is found. The emergence of hybrid interface bands is demonstrated as an imprint of the interfacial bonding in the electronic properties. Inspection of corresponding partial charge densities of these bands unambiguously reveals the delocalized character of these features exhibiting contributions on both 2D components.

The interfacial bonding translates then also into a substantial magnetic coupling between the 2D components. We observe both ferromagnetic and antiferromagnetic interfacial coupling with the details depending on the individual HS.

Finally, also an outlook towards twisted non-vdW HSs is provided as such systems can host new and enhanced

effects. Keeping the sizes tractable for density functional electronic structure calculations, a strong dependence of the binding energy and electronic as well as magnetic properties on the twist angle are found. Different local atomic arrangements reveal moiré patterns due to stacking and twisting and thus lead to characteristic long-range variations of the (magnetisation) density above the HS surfaces – readily observable with different experimental techniques.

For unlocking and leveraging the versatility of non-vdW HSs, the present work goes beyond the study and design of individual (nanoscale) materials and moves towards the systematic data-driven autonomous design of functional interfaces. Non-vdW HSs are a prime example of such a new class of interfaces that – due to their unique interfacial bonding characteristics – can host many appealing effects and phenomena ranging from charge delocalisation over interfacial magnetic coupling down to correlated flatband physics.

III. METHODS

Hetbuilder: HSs are generated by a custom “hetbuilder” implementation of the coincidence lattice method following the work of Koda *et al.* [63, 64]. The initial structures for the input 2D sheets are sourced from the dataset of previously proposed non-van der Waals 2D materials [43, 44]. The components are initially placed 2 \AA apart in the vertical direction perpendicular to the sheets and duplicate structure removal is based on structure comparison and energy evaluation due to force fields. The mismatch criterion (tolerance) is set to 0.2 \AA and the maximum number of unit cell repetitions is limited to five ensuring that the HS cell contains less than 500 atoms. The hetbuilder tool automatically calculates the nominal strain for the resulting HSs.

For a HS out of two 2D components, the strain is calculated as the sum of the relative deformations in both individual systems:

$$\text{strain} = 2 \left(\left| 1 - \frac{a_{\text{HS}}}{a_1} \right| + \left| 1 - \frac{a_{\text{HS}}}{a_2} \right| \right),$$

where a_{HS} is the lattice constant of the initial or relaxed HS and $a_{1/2}$ is the lattice constant of the relaxed first/second 2D component. The factor of two accounts for the two equivalent hexagonal directions.

Density functional calculations: For all HSs, DFT calculations including structural relaxations as well as evaluation of band structure and DOS are performed. The computations for the exchange-correlation functional PBE+ U [65–68] are executed with AFLOW [69, 70] commanding the Vienna Ab-initio Simulation Package (VASP) [71, 72] with settings according to the AFLOW standard [73], and internal VASP precision set to ACCURATE. Electrostatic dipole corrections for energies, potentials, and forces are included [74], along with non-spherical

contributions from gradient corrections inside projector-augmented wave (PAW) spheres. For systems with an absolute binding energy smaller than $20 \text{ meV}/\text{\AA}^2$ from plain PBE+ U , the D3 dispersion correction [59] is applied. The AFLOW internal automatic determination of k -point sets is used in conjunction with an extension for 2D systems enabling only in-plane sampling to be released in a future version. The number of k -points per reciprocal atom is set to 2500 for static calculations which is reduced to 400 for structural relaxations.

The charge density difference is computed as:

$$n_{\text{diff}}(\mathbf{r}) = n_{\text{HS}}(\mathbf{r}) - n_1^{\text{static}}(\mathbf{r}) - n_2^{\text{static}}(\mathbf{r}), \quad (1)$$

where $n_{\text{HS}}(\mathbf{r})$ is the charge density of the relaxed HS and $n_{1/2}^{\text{static}}(\mathbf{r})$ is the density of 2D component 1/2 with the same atomic positions as in the HS obtained from a single self-consistent electronic calculation.

The binding energy E_b per unit area is calculated as:

$$E_b = \frac{E_{\text{HS}} - E_1 - E_2}{A}, \quad (2)$$

where E_{HS} is the total energy of the HS, E_1/E_2 is the energy of the individual 2D component 1/2, and A is the area of the relaxed HS. The graphene homobilayer binding energy is computed with both D3 dispersion correction and SCAN+rVV10 vdW functional [60, 61] to $-16 \text{ meV}/\text{\AA}^2$.

All systems are rigorously checked for magnetism. For systems formed from diamagnetic components, both spin-polarized and non spin-polarized calculations are conducted. However, none of the systems developed a magnetic ground state significantly lower in energy than the diamagnetic one. In HSs involving one magnetic 2D component, the magnetic configuration is initialized as known from our previous studies [43, 44] of the individual sheets and still trying for five different sizes of all magnetic moments from 1 to $5 \mu_B$ in the spirit of the procedure introduced in Ref. [75]. For systems with two magnetic components, the magnetic configurations are again as before

guided by the individual cases and initiated in two different ways considering both parallel (ferromagnetic) and antiparallel (antiferromagnetic) alignment of the spins at the interface. The resulting coupling energy E_c is calculated as the difference between the corresponding antiferromagnetic (E_{AFM}) and ferromagnetic (E_{FM}) states:

$$E_c = E_{\text{AFM}} - E_{\text{FM}}. \quad (3)$$

A positive coupling energy thus indicates that the ferromagnetic alignment is energetically preferred.

IV. DATA AVAILABILITY

The primary research data of this study are available from the Rossendorf Data Repository (RODARE) via <https://doi.org/10.14278/rodare.3621> [76].

ACKNOWLEDGMENTS

The authors thank Agnieszka Kuc for fruitful discussions. R.F. acknowledges funding from the German Research Foundation (DFG), project FR 4545/2-1, the collaborative research center ‘‘Chemistry of Synthetic Two-Dimensional Materials’’ SFB-1415-417590517, and for the ‘‘Autonomous Materials Thermodynamics’’ (AutoMaT) project by Technische Universitat Dresden and Helmholtz-Zentrum Dresden-Rossendorf within the DRESDEN-concept alliance. The authors thank the HZDR Computing Center, HLRS Stuttgart (HAWK cluster), the Paderborn Center for Parallel Computing (PC2, Noctua 2 cluster), and TU Dresden ZIH (Taurus cluster) for generous grants of CPU time.

V. AUTHOR CONTRIBUTIONS

R.F. initiated and supervised the project. A.N. built the HSs and performed all DFT calculations. A.N., T.B., and R.F. analyzed the data and performed all post-processing. A.N. wrote the initial draft of the manuscript which was then refined by R.F. All authors contributed to the writing and discussion of the final manuscript.

[1] H. Kroemer, *Nobel Lecture: Quasielectric fields and band offsets: teaching electrons new tricks*, Rev. Mod. Phys. **73**, 783–793 (2001), doi:10.1103/RevModPhys.73.783.

[2] M. P. Levendorf, C.-J. Kim, L. Brown, P. Y. Huang, R. W. Havener, D. A. Muller, and J. Park, *Graphene and boron nitride lateral heterostructures for atomically thin circuitry*, Nature **488**, 627–632 (2012), doi:10.1038/nature11408.

[3] K. Mehlich, M. Ghorbani-Asl, D. Sahn, T. Chagas, D. Weber, C. Grover, D. Dombrowski, A. V. Krasheninnikov, and C. Busse, *Dislocation-free two-dimensional concentric lateral heterostructures: MoS₂-TaS₂/Au(111)*, 2D Materials **11**, 035035 (2024), doi:10.1088/2053-

1583/ad5737.

[4] S. Pakdel, A. Rasmussen, A. Taghizadeh, M. Kruse, T. Olsen, and K. S. Thygesen, *High-throughput computational stacking reveals emergent properties in natural van der Waals bilayers*, Nat. Commun. **15**, 932 (2024), doi:10.1038/s41467-024-45003-w.

[5] A. K. Geim and I. V. Grigorieva, *Van der Waals heterostructures*, Nature **499**, 419–425 (2013), doi:10.1038/nature12385.

[6] Y. Liu, N. O. Weiss, X. Duan, H.-C. Cheng, Y. Huang, and X. Duan, *Van der Waals heterostructures and devices*, Nat. Rev. Mater. **1**, 16042 (2016), doi:10.1038/natrevmats.2016.42.

- [7] K. S. Novoselov, A. Mishchenko, A. Carvalho, and A. H. Castro Neto, *2D materials and van der Waals heterostructures*, *Science* **353**, aac9439 (2016), doi:10.1126/science.aac9439.
- [8] M. Gibertini, M. Koperski, A. F. Morpurgo, and K. S. Novoselov, *Magnetic 2D materials and heterostructures*, *Nat. Nanotechnol.* **14**, 408–419 (2019), doi:10.1038/s41565-019-0438-6.
- [9] P. V. Pham, S. C. Bodepudi, K. Shehzad, Y. Liu, Y. Xu, B. Yu, and X. Duan, *2D Heterostructures for Ubiquitous Electronics and Optoelectronics: Principles, Opportunities, and Challenges*, *Chem. Rev.* **122**, 6514–6613 (2022), doi:10.1021/acs.chemrev.1c00735.
- [10] H. Wang, F. Liu, W. Fu, Z. Fang, W. Zhou, and Z. Liu, *Two-dimensional heterostructures: fabrication, characterization, and application*, *Nanoscale* **6**, 12250–12272 (2014), doi:10.1039/c4nr03435j.
- [11] K. Kim, M. Yankowitz, B. Fallahzad, S. Kang, H. C. P. Movva, S. Huang, S. Larentis, C. M. Corbet, T. Taniguchi, K. Watanabe, S. K. Banerjee, B. J. LeRoy, and E. Tutuc, *van der Waals Heterostructures with High Accuracy Rotational Alignment*, *Nano Lett.* **16**, 1989–1995 (2016), doi:10.1021/acs.nanolett.5b05263.
- [12] M.-Y. Li, C.-H. Chen, Y. Shi, and L.-J. Li, *Heterostructures based on two-dimensional layered materials and their potential applications*, *Mater. Today* **19**, 322–335 (2016), doi:10.1016/j.mattod.2015.11.003.
- [13] A. Castellanos-Gomez, X. Duan, Z. Fei, H. R. Gutierrez, Y. Huang, X. Huang, J. Queda, Q. Qian, E. Sutter, and P. Sutter, *Van der Waals heterostructures*, *Nat. Rev. Methods Primers* **2**, 58 (2022), doi:10.1038/s43586-022-00139-1.
- [14] Y. Cao, V. Fatemi, S. Fang, K. Watanabe, T. Taniguchi, E. Kaxiras, and P. Jarillo-Herrero, *Unconventional superconductivity in magic-angle graphene superlattices*, *Nature* **556**, 43–50 (2018), doi:10.1038/nature26160.
- [15] F. M. Arnold, A. Ghasemifard, A. Kuc, and T. Heine, *Implementing electronic signatures of graphene and hexagonal boron nitride in twisted bilayer molybdenum disulfide*, *Mater. Today* **73**, 96–104 (2024), doi:10.1016/j.mattod.2024.01.012.
- [16] S. Lebègue, T. Björkman, M. Klintonberg, R. M. Nieminen, and O. Eriksson, *Two-Dimensional Materials from Data Filtering and Ab Initio Calculations*, *Phys. Rev. X* **3**, 031002 (2013), doi:10.1103/PhysRevX.3.031002.
- [17] G. Cheon, K.-A. N. Duerloo, A. D. Sendek, C. Porter, Y. Chen, and E. J. Reed, *Data Mining for New Two- and One-Dimensional Weakly Bonded Solids and Lattice-Commensurate Heterostructures*, *Nano Lett.* **17**, 1915–1923 (2017), doi:10.1021/acs.nanolett.6b05229.
- [18] N. Mounet, M. Gibertini, P. Schwaller, D. Campi, A. Merkys, A. Marrazzo, T. Sohier, I. E. Castelli, A. Cappelletti, G. Pizzi, and N. Marzari, *Two-dimensional materials from high-throughput computational exfoliation of experimentally known compounds*, *Nat. Nanotechnol.* **13**, 246–252 (2018), doi:10.1038/s41565-017-0035-5.
- [19] A. P. Balan, A. B. Puthirath, S. Roy, G. Costin, E. F. Oliveira, M. A. S. R. Saadi, V. Sreepal, R. Friedrich, P. Serles, A. Biswas, S. A. Iyengar, N. Chakingal, S. Bhattacharyya, S. K. Saju, S. C. Pardo, L. M. Sassi, T. Filleter, A. Krasheninnikov, D. S. Galvao, R. Vajtai, R. R. Nair, and P. M. Ajayan, *Non-van der Waals quasi-2D materials; recent advances in synthesis, emergent properties and applications*, *Mater. Today* **58**, 164 (2022), doi:10.1016/j.mattod.2022.07.007.
- [20] H. Kaur and J. N. Coleman, *Liquid-Phase Exfoliation of Nonlayered Non-Van-Der-Waals Crystals into Nanoplatelets*, *Adv. Mater.* **34**, 2202164 (2022), doi:10.1002/adma.202202164.
- [21] A. Puthirath Balan, S. Radhakrishnan, C. F. Woellner, S. K. Sinha, L. Deng, C. d. l. Reyes, B. M. Rao, M. Paulose, R. Neupane, A. Apte, V. Kochat, R. Vajtai, A. R. Harutyunyan, C.-W. Chu, G. Costin, D. S. Galvao, A. A. Martí, P. A. van Aken, O. K. Varghese, C. S. Tiwary, A. Malie Madom Ramaswamy Iyer, and P. M. Ajayan, *Exfoliation of a non-van der Waals material from iron ore hematite*, *Nat. Nanotechnol.* **13**, 602–609 (2018), doi:10.1038/s41565-018-0134-y.
- [22] A. Puthirath Balan, S. Radhakrishnan, R. Kumar, R. Neupane, S. K. Sinha, L. Deng, C. A. de los Reyes, A. Apte, B. M. Rao, M. Paulose, R. Vajtai, C. W. Chu, G. Costin, A. A. Martí, O. K. Varghese, A. K. Singh, C. S. Tiwary, M. R. Anantharaman, and P. M. Ajayan, *A Non-van der Waals Two-Dimensional Material from Natural Titanium Mineral Ore Ilmenite*, *Chem. Mater.* **30**, 5923–5931 (2018), doi:10.1021/acs.chemmater.8b01935.
- [23] G. Guan, J. Xia, S. Liu, Y. Cheng, S. Bai, S. Y. Tee, Y.-W. Zhang, and M.-Y. Han, *Electrostatic-Driven Exfoliation and Hybridization of 2D Nanomaterials*, *Adv. Mater.* **29**, 1700326 (2017), doi:10.1002/adma.201700326.
- [24] T. P. Yadav, S. N. Shirodkar, N. Lertcumfu, S. Radhakrishnan, F. N. Sayed, K. D. Malviya, G. Costin, R. Vajtai, B. I. Yakobson, C. S. Tiwary, and P. M. Ajayan, *Chromiteen: A New 2D Oxide Magnetic Material from Natural Ore*, *Adv. Mater. Interfaces* **5**, 1800549 (2018), doi:10.1002/admi.201800549.
- [25] S. Liu, L. Xie, H. Qian, G. Liu, H. Zhong, and H. Zeng, *Facile preparation of novel and active 2D nanosheets from non-layered and traditionally non-exfoliable earth-abundant materials*, *J. Mater. Chem. A* **7**, 15411–15419 (2019), doi:10.1039/C9TA04442F.
- [26] A. B. Puthirath, S. N. Shirodkar, G. Gao, F. C. R. Hernandez, L. Deng, R. Dahal, A. Apte, G. Costin, N. Chakingal, A. P. Balan, L. M. Sassi, C. S. Tiwary, R. Vajtai, C.-W. Chu, B. I. Yakobson, and P. M. Ajayan, *Scale-Enhanced Magnetism in Exfoliated Atomically Thin Magnetite Sheets*, *Small* **16**, 2004208 (2020), doi:10.1002/smll.202004208.
- [27] H. Kaur, R. Tian, A. Roy, M. McCrystal, D. V. Horvath, G. Lozano Onrubia, R. Smith, M. Ruether, A. Griffin, C. Backes, V. Nicolosi, and J. N. Coleman, *Production of Quasi-2D Platelets of Nonlayered Iron Pyrite (FeS₂) by Liquid-Phase Exfoliation for High Performance Battery Electrodes*, *ACS Nano* **14**, 13418–13432 (2020), doi:10.1021/acsnano.0c05292.
- [28] A. B. Puthirath, A. P. Balan, E. F. Oliveira, V. Sreepal, F. C. Robles Hernandez, G. Gao, N. Chakingal, L. M. Sassi, P. Thibeorchews, G. Costin, R. Vajtai, D. S. Galvao, R. R. Nair, and P. M. Ajayan, *Apparent Ferromagnetism in Exfoliated Ultrathin Pyrite Sheets*, *J. Phys. Chem. C* **125**, 18927–18935 (2021), doi:10.1021/acs.jpcc.1c04977.
- [29] M. G. Moinuddin, S. Srinivasan, and S. K. Sharma, *Probing Ferrimagnetic Semiconductor with Enhanced Negative Magnetoresistance: 2D Chromium Sulfide*, *Adv. Electron. Mater.* **7**, 2001116 (2021), doi:10.1002/aelm.202001116.
- [30] L. Hu, L. Cao, L. Li, J. Duan, X. Liao, F. Long, J. Zhou, Y. Xiao, Y.-J. Zeng, and S. Zhou, *Two-dimensional magneto-photoconductivity in non-van der Waals man-*

- ganese selenide*, Mater. Horiz. **8**, 1286–1296 (2021), doi:10.1039/D1MH00009H.
- [31] A. Yousaf, M. S. Gilliam, S. L. Y. Chang, M. Augustin, Y. Guo, F. Tahir, M. Wang, A. Schwindt, X. S. Chu, D. O. Li, S. Kale, A. Debnath, Y. Liu, M. D. Green, E. J. G. Santos, A. A. Green, and Q. H. Wang, *Exfoliation of Quasi-Two-Dimensional Nanosheets of Metal Diborides*, J. Phys. Chem. C **125**, 6787–6799 (2021), doi:10.1021/acs.jpcc.1c00394.
- [32] Y. Guo, A. Gupta, M. S. Gilliam, A. Debnath, A. Yousaf, S. Saha, M. D. Levin, A. A. Green, A. K. Singh, and Q. H. Wang, *Exfoliation of boron carbide into ultra-thin nanosheets*, Nanoscale **13**, 1652–1662 (2021), doi:10.1039/D0NR07971E.
- [33] C. Gibaja, D. Rodríguez-San-Miguel, W. S. Paz, I. Torres, E. Salagre, P. Segovia, E. G. Michel, M. Assebban, P. Ares, D. Hernández-Maldonado, Q. Ramasse, G. Abellán, J. Gómez-Herrero, M. Varela, J. J. Palacios, and F. Zamora, *Exfoliation of Alpha-Germanium: A Covalent Diamond-Like Structure*, Adv. Mater. **33**, 2006826 (2021), doi:10.1002/adma.202006826.
- [34] J. Xu, W. Li, B. Zhang, L. Zha, W. Hao, S. Hu, J. Yang, S. Li, S. Gao, and Y. Hou, *Free-standing 2D non-van der Waals antiferromagnetic hexagonal FeSe semiconductor: halide-assisted chemical synthesis and Fe²⁺ related magnetic transitions*, Chem. Sci. **13**, 203–209 (2021), doi:10.1039/D1SC04122C.
- [35] J. Peng, Y. Liu, H. Lv, Y. Li, Y. Lin, Y. Su, J. Wu, H. Liu, Y. Guo, Z. Zhuo, X. Wu, C. Wu, and Y. Xie, *Stoichiometric two-dimensional non-van der Waals AgCrS₂ with superionic behaviour at room temperature*, Nat. Chem. **13**, 1235–1240 (2021), doi:10.1038/s41557-021-00800-4.
- [36] S. Homkar, B. Chand, S. S. Rajput, S. Gorantla, T. Das, R. Babar, S. Patil, R. Klingeler, S. Nair, M. Kabir, and A. Bajpai, *Few-Layer SrRu₂O₆ Nanosheets as Non-Van der Waals Honeycomb Antiferromagnets: Implications for Two-Dimensional Spintronics*, ACS Appl. Nano Mater. **4**, 9313–9321 (2021), doi:10.1021/acsnm.1c01788.
- [37] S. Chahal, S. M. Kauzlarich, and P. Kumar, *Microwave Synthesis of Hematene and Other Two-Dimensional Oxides*, ACS Materials Lett. **3**, 631–640 (2021), doi:10.1021/acsmaterialslett.1c00102.
- [38] B. Y. Zhang, K. Xu, Q. Yao, A. Jannat, G. Ren, M. R. Field, X. Wen, C. Zhou, A. Zavabeti, and J. Z. Ou, *Hexagonal metal oxide monolayers derived from the metal-gas interface*, Nat. Mater. **20**, 1073–1078 (2021), doi:10.1038/s41563-020-00899-9.
- [39] T. Chen, H. Kaur, M. McCrystall, R. Tian, A. Roy, R. Smith, D. V. Horvath, J. Maughan, B. Konkena, M. Venkatesan, K. Synnatschke, T. Carey, J. Liu, J. Pepper, R. Zhang, C. Backes, V. Nicolosi, H. Xia, and J. N. Coleman, *Liquid phase exfoliation of nonlayered non-van der Waals iron trifluoride (FeF₃) into 2D-platelets for high-capacity lithium storing cathodes*, FlatChem **33**, 100360 (2022), doi:10.1016/j.flatc.2022.100360.
- [40] A. N. Toksumakov, G. A. Ermolaev, A. S. Slavich, N. V. Doroshina, E. V. Sukhanova, D. I. Yakubovsky, A. V. Syuy, S. M. Novikov, R. I. Romanov, A. M. Markeev, A. S. Oreshonkov, D. M. Tsymbarenko, Z. I. Popov, D. G. Kvashnin, A. A. Vyshnevyy, A. V. Arsenin, D. A. Ghazaryan, and V. S. Volkov, *High-refractive index and mechanically cleavable non-van der Waals InGaS₃*, npj 2D Materials and Applications **6**, 85 (2022), doi:10.1038/s41699-022-00359-9.
- [41] A. Puthirath Balan, E. F. Oliveira, G. Costin, T. Gray, N. Chakingal, A. Biswas, and A. B. Puthirath, *Magnetostructural phase transition in exfoliated pyrrhotite (Fe₇S₈) ultra-thin sheets*, Oxford Open Materials Science **3**, 1–7 (2023), doi:10.1093/oxfmat/itac020.
- [42] K. Jiang, J. Ji, W. Gong, L. Ding, J. Li, P. Li, B. Li, and F. Geng, *Mechanical cleavage of non-van der Waals structures towards two-dimensional crystals*, Nat. Synth. **2**, 58–66 (2023), doi:10.1038/s44160-022-00182-6.
- [43] R. Friedrich, M. Ghorbani-Asl, S. Curtarolo, and A. V. Krashennnikov, *Data-Driven Quest for Two-Dimensional Non-van der Waals Materials*, Nano Lett. **22**, 989–997 (2022), doi:10.1021/acs.nanolett.1c03841.
- [44] T. Barnowsky, A. V. Krashennnikov, and R. Friedrich, *A New Group of 2D Non-van der Waals Materials with Ultra Low Exfoliation Energies*, Adv. Electron. Mater. **9**, 2201112 (2023), doi:10.1002/aelm.202201112.
- [45] M. Bagheri, E. Berger, and H.-P. Komsa, *Identification of Material Dimensionality Based on Force Constant Analysis*, J. Phys. Chem. Lett. **14**, 7840–7847 (2023), doi:10.1021/acs.jpcclett.3c01635.
- [46] T. Barnowsky, S. Curtarolo, A. V. Krashennnikov, T. Heine, and R. Friedrich, *Magnetic State Control of Non-van der Waals 2D Materials by Hydrogenation*, Nano Lett. **24**, 3874–3881 (2024), doi:10.1021/acs.nanolett.3c04777.
- [47] Y. Chen, N. Pryds, J. E. Kleibeuker, G. Koster, J. Sun, E. Stamate, B. Shen, G. Rijnders, and S. Linderorth, *Metallic and Insulating Interfaces of Amorphous SrTiO₃-Based Oxide Heterostructures*, Nano Lett. **11**, 3774–3778 (2011), doi:10.1021/nl201821j.
- [48] N. Reyren, S. Thiel, A. D. Caviglia, L. Fitting Kourkoutis, G. Hammerl, C. Richter, C. W. Schneider, T. Kopp, A.-S. Rüetschi, D. Jaccard, M. Gabay, D. A. Müller, J.-M. Triscone, and J. Mannhart, *Superconducting Interfaces Between Insulating Oxides*, Science **317**, 1196–1199 (2007), doi:10.1126/science.1146006.
- [49] A. Brinkman, M. Huijben, M. van Zalk, J. Huijben, U. Zeitler, J. C. Maan, W. G. van der Wiel, G. Rijnders, D. H. A. Blank, and H. Hilgenkamp, *Magnetic effects at the interface between non-magnetic oxides*, Nat. Mater. **6**, 493–496 (2007), doi:10.1038/nmat1931.
- [50] Y. Z. Chen, N. Bovet, F. Trier, D. V. Christensen, F. M. Qu, N. H. Andersen, T. Kasama, W. Zhang, R. Giraud, J. Dufouleur, T. S. Jespersen, J. R. Sun, A. Smith, J. Nygård, L. Lu, B. Büchner, B. G. Shen, S. Linderorth, and N. Pryds, *A high-mobility two-dimensional electron gas at the spinel/perovskite interface of γ -Al₂O₃/SrTiO₃*, Nat. Commun. **4**, 1371 (2013), doi:10.1038/ncomms2394.
- [51] Y. Z. Chen, F. Trier, T. Wijnands, R. J. Green, N. Gauquelin, R. Egoavil, D. V. Christensen, G. Koster, M. Huijben, N. Bovet, S. Macke, F. He, R. Sutarto, N. H. Andersen, J. A. Sulpizio, M. Honig, G. E. D. K. Prawiroatmodjo, T. S. Jespersen, S. Linderorth, S. Ilani, J. Verbeeck, G. Van Tendeloo, G. Rijnders, G. A. Sawatzky, and N. Pryds, *Extreme mobility enhancement of two-dimensional electron gases at oxide interfaces by charge-transfer-induced modulation doping*, Nat. Mater. **14**, 801–806 (2015), doi:10.1038/nmat4303.
- [52] F. Cossu, H.-S. Kim, B. Sanyal, and I. Di Marco, *Persistent half-metallic ferromagnetism in a (111)-oriented manganite superlattice*, npj Comput. Mater. **8**, 77 (2022), doi:10.1038/s41524-022-00759-x.

- [53] R. Erlandsen, R. T. Dahm, F. Trier, M. Scuderi, E. Di Gennaro, A. Sambri, C. K. Reffeldt Kirchert, N. Pryds, F. M. Granozio, and T. S. Jespersen, *A Two-Dimensional Superconducting Electron Gas in Freestanding LaAlO₃/SrTiO₃ Micromembranes*, *Nano Lett.* **22**, 4758–4764 (2022), doi:10.1021/acs.nanolett.2c00992.
- [54] A. V. Bjørlig, D. V. Christensen, R. Erlandsen, N. Pryds, and B. Kalisky, *Current Mapping of Amorphous LaAlO₃/SrTiO₃ near the Metal-Insulator Transition*, *ACS Appl. Electron. Mater.* **4**, 3421–3427 (2022), doi:10.1021/acsaem.2c00264.
- [55] H. Li, Y. Gan, M.-A. Husanu, R. T. Dahm, D. V. Christensen, M. Radovic, J. Sun, M. Shi, B. Shen, N. Pryds, and Y. Chen, *Robust Electronic Structure of Manganite-Buffered Oxide Interfaces with Extreme Mobility Enhancement*, *ACS Nano* **16**, 6437–6443 (2022), doi:10.1021/acsnano.2c00609.
- [56] Y. Li, C. Xiang, F. M. Chiabrera, S. Yun, H. Zhang, D. J. Kelly, R. T. Dahm, C. K. R. Kirchert, T. E. Le Cozannet, F. Trier, D. V. Christensen, T. J. Booth, S. B. Simonsen, S. Kadkhodazadeh, T. S. Jespersen, and N. Pryds, *Stacking and Twisting of Freestanding Complex Oxide Thin Films*, *Adv. Mater.* **34**, 2203187 (2022), doi:10.1002/adma.202203187.
- [57] J. H. Jung, C.-H. Park, and J. Ihm, *A Rigorous Method of Calculating Exfoliation Energies from First Principles*, *Nano Lett.* **18**, 2759–2765 (2018), doi:10.1021/acs.nanolett.7b04201.
- [58] T. Björkman, A. Gulans, A. V. Krasheninnikov, and R. M. Nieminen, *van der Waals Bonding in Layered Compounds from Advanced Density-Functional First-Principles Calculations*, *Phys. Rev. Lett.* **108**, 235502 (2012), doi:10.1103/PhysRevLett.108.235502.
- [59] S. Grimme, J. Antony, S. Ehrlich, and H. Krieg, *A consistent and accurate ab initio parametrization of density functional dispersion correction (DFT-D) for the 94 elements H-Pu*, *J. Chem. Phys.* **132**, 154104 (2010), doi:10.1063/1.3382344.
- [60] J. Sun, A. Ruzsinszky, and J. P. Perdew, *Strongly Constrained and Appropriately Normed Semilocal Density Functional*, *Phys. Rev. Lett.* **115**, 036402 (2015), doi:10.1103/PhysRevLett.115.036402.
- [61] H. Peng, Z.-H. Yang, J. P. Perdew, and J. Sun, *Versatile van der Waals Density Functional Based on a Meta-Generalized Gradient Approximation*, *Phys. Rev. X* **6**, 041005 (2016), doi:10.1103/PhysRevX.6.041005.
- [62] V. Heß, R. Friedrich, F. Matthes, V. Caciuc, N. Atodiresei, D. E. Bürgler, Stefan Blügel, and C. M. Schneider, *Magnetic subunits within a single molecule-surface hybrid*, *New J. Phys.* **19**, 053016 (2017), doi:10.1088/1367-2630/aa6ece.
- [63] D. S. Koda, F. Bechstedt, M. Marques, and L. K. Teles, *Coincidence Lattices of 2D Crystals: Heterostructure Predictions and Applications*, *J. Phys. Chem. C* **120**, 10895–10908 (2016), doi:10.1021/acs.jpcc.6b01496.
- [64] R. Kempt, *romankempt/hetbuilder: Zenodo Release*, Zenodo (2021), doi:10.5281/zenodo.4721346.
- [65] J. P. Perdew, K. Burke, and M. Ernzerhof, *Generalized Gradient Approximation Made Simple*, *Phys. Rev. Lett.* **77**, 3865–3868 (1996), doi:10.1103/PhysRevLett.77.3865.
- [66] V. I. Anisimov, J. Zaanen, and O. K. Andersen, *Band theory and Mott insulators: Hubbard U instead of Stoner I*, *Phys. Rev. B* **44**, 943–954 (1991), doi:10.1103/PhysRevB.44.943.
- [67] A. I. Liechtenstein, V. I. Anisimov, and J. Zaanen, *Density-functional theory and strong interactions: Orbital ordering in Mott-Hubbard insulators*, *Phys. Rev. B* **52**, R5467–R5470 (1995), doi:10.1103/PhysRevB.52.R5467.
- [68] S. L. Dudarev, G. A. Botton, S. Y. Savrasov, C. J. Humphreys, and A. P. Sutton, *Electron-energy-loss spectra and the structural stability of nickel oxide: An LSDA+U study*, *Phys. Rev. B* **57**, 1505–1509 (1998), doi:10.1103/PhysRevB.57.1505.
- [69] C. Oses, M. Esters, D. Hicks, S. Divilov, H. Eckert, R. Friedrich, M. J. Mehl, A. Smolyanyuk, X. Campilongo, A. van de Walle, J. Schroers, A. G. Kusne, I. Takeuchi, E. Zurek, M. B. Nardelli, M. Fornari, Y. Lederer, O. Levy, C. Toher, and S. Curtarolo, *afLOW++: A C++ framework for autonomous materials design*, *Comput. Mater. Sci.* **217**, 111889 (2023), doi:10.1016/j.commatsci.2022.111889.
- [70] M. Esters, C. Oses, S. Divilov, H. Eckert, R. Friedrich, D. Hicks, M. J. Mehl, F. Rose, A. Smolyanyuk, A. Calzolari, X. Campilongo, C. Toher, and S. Curtarolo, *afLOW.org: A web ecosystem of databases, software and tools*, *Comput. Mater. Sci.* **216**, 111808 (2023), doi:10.1016/j.commatsci.2022.111808.
- [71] G. Kresse and J. Furthmüller, *Efficient iterative schemes for ab initio total-energy calculations using a plane-wave basis set*, *Phys. Rev. B* **54**, 11169–11186 (1996), doi:10.1103/PhysRevB.54.11169.
- [72] G. Kresse and D. Joubert, *From ultrasoft pseudopotentials to the projector augmented-wave method*, *Phys. Rev. B* **59**, 1758–1775 (1999), doi:10.1103/PhysRevB.59.1758.
- [73] C. E. Calderon, J. J. Plata, C. Toher, C. Oses, O. Levy, M. Fornari, A. Natan, M. J. Mehl, G. L. W. Hart, M. Buongiorno Nardelli, and S. Curtarolo, *The AFLOW standard for high-throughput materials science calculations*, *Comput. Mater. Sci.* **108 Part A**, 233–238 (2015), doi:10.1016/j.commatsci.2015.07.019.
- [74] J. Neugebauer and M. Scheffler, *Adsorbate-substrate and adsorbate-adsorbate interactions of Na and K adlayers on Al(111)*, *Phys. Rev. B* **46**, 16067–16080 (1992), doi:10.1103/PhysRevB.46.16067.
- [75] R. Friedrich, D. Usanmaz, C. Oses, A. Supka, M. Fornari, M. Buongiorno Nardelli, C. Toher, and S. Curtarolo, *Coordination corrected ab initio formation enthalpies*, *npj Comput. Mater.* **5**, 59 (2019), doi:10.1038/s41524-019-0192-1.
- [76] A. Nihei, T. Barnowsky, and R. Friedrich, *Data publication: Non-van der Waals Heterostructures*, *Rodare* (2025), doi:10.14278/rodare.3621.

Non-van der Waals Heterostructures Supporting Information

Anastasiia Nihei,^{1,2} Tom Barnowsky,^{1,2} and Rico Friedrich^{1,2,3,*}

¹Theoretical Chemistry, Technische Universität Dresden, 01062 Dresden, Germany

²Institute of Ion Beam Physics and Materials Research,

Helmholtz-Zentrum Dresden-Rossendorf, 01328 Dresden, Germany

³Center for Extreme Materials, Duke University, Durham, NC 27708, USA

(Dated: March 14, 2025)

I. Charge density differences for non-vdW HSs

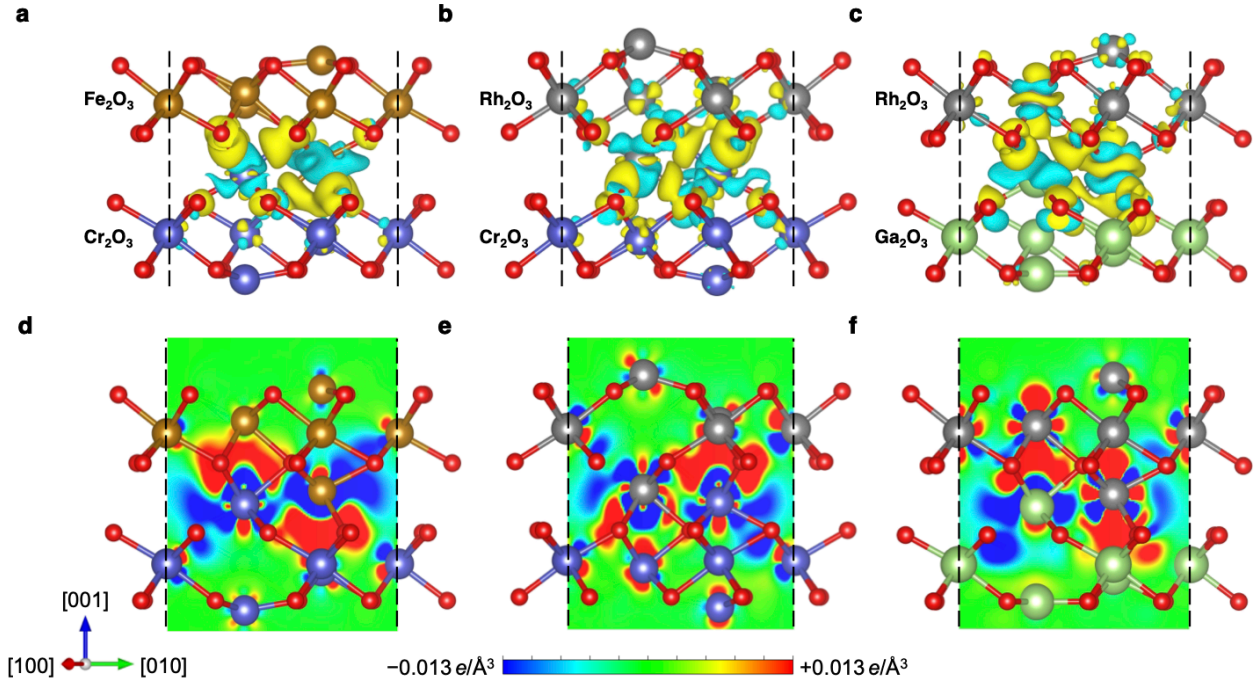


FIG. S1: Isosurface plots of the charge density difference for $\text{Cr}_2\text{O}_3/\text{Fe}_2\text{O}_3$ (a), $\text{Cr}_2\text{O}_3/\text{Rh}_2\text{O}_3$ (b), and $\text{Ga}_2\text{O}_3/\text{Rh}_2\text{O}_3$ (c) with charge gain/loss indicated by yellow/bluish parts (isosurface value: $\pm 0.027 \text{ e}/\text{\AA}^3$). (d-f) Cut through the charge density difference on the (110) plane. The compass indicating crystal directions applies to all subfigures.

II. Assessing the role of dispersion contributions

The influence of including a D3 [1] dispersion correction to PBE+ U [2–5] or employing the SCAN+rVV10 vdW functional [6, 7] on the optimized interfacial bond lengths and binding energies is benchmarked for thirteen HSs (Table I). As expected, for systems with a high binding energy from plain PBE+ U more negative than $-70 \text{ meV}/\text{\AA}^2$, the effect of dispersion is very small as they are already strongly bonded with changes in bond lengths of maximally 0.04 \AA being negligible. The increase in binding energy appears to be rather large of the order of -30 to $-50 \text{ meV}/\text{\AA}^2$. This dispersion-induced contribution stems, however, from the fact that the 2D layers are not atomically thin as graphene and then the vdW interactions between several atoms add up but the net effect on the structure and even electronic properties is very minor.

* rico.friedrich@tu-dresden.de

On the other hand, slightly larger (relative) changes are found for systems with binding energies between $-20 \text{ meV}/\text{\AA}^2$ and $-70 \text{ meV}/\text{\AA}^2$ where both D3 inclusion and SCAN+rVV10 consistently cause bonds to shorten by typically more than $\sim 0.05 \text{ \AA}$ and binding energies increase by close to a factor of two. However, we still see no drastic change in the electronic properties.

Dispersion should be included for systems where plain DFT yields absolute binding energies below $20 \text{ meV}/\text{\AA}^2$ – the typical energy scale of vdW interactions [8]. This is clearly the case for the seven HSs with the smallest absolute E_b at the top of the table. For these systems, we also note that the absolute binding energy from plain PBE+ U increases by more than 100% for both dispersion approaches setting them apart from all other systems where the influence is weaker. The bond lengths shorten in almost all cases drastically by up to 0.68 \AA for both vdW approaches and also the binding energies reach a proper negative dispersive energy range. A particularly special case is the $\text{Rh}_2\text{O}_3/\text{TiZnO}_3$ system where the small binding energy of $-10 \text{ meV}/\text{\AA}^2$ increases by a factor of six upon dispersion correction.

TABLE I: Comparison of interfacial bond lengths d_1 and d_2 as well as binding energies E_b for different systems with and without dispersion correction (D3) as well as with SCAN+rVV10 functional.

System	PBE(+ U)			PBE(+ U)+D3			SCAN+rVV10		
	d_1 (Å)	d_2 (Å)	E_b per Area (meV/Å ²)	d_1 (Å)	d_2 (Å)	E_b per Area (meV/Å ²)	d_1 (Å)	d_2 (Å)	E_b per Area (meV/Å ²)
CdTiO ₃ /SbTiO ₃	4.32	3.50	-3	4.13	3.32	-27	3.64	3.02	-22
NaSbO ₃ /SbTiO ₃	4.06	3.52	-4	3.56	3.17	-22	3.74	3.26	-15
KSbO ₃ /SnZnO ₃	3.02	3.73	-10	2.85	3.36	-33	2.81	3.37	-29
Rh ₂ O ₃ /TiZnO ₃	2.60	2.53	-10	2.45	2.34	-64	2.42	2.32	-60
AgSbO ₃ /SnZnO ₃	2.78	3.19	-13	2.65	2.98	-49	2.66	2.96	-44
NaSbO ₃ /SnZnO ₃	2.70	3.10	-16	2.63	2.99	-47	2.54	2.87	-40
AgSbO ₃ /KSbO ₃	2.90	2.86	-19	2.86	2.82	-45	2.78	2.77	-42
KSbO ₃ /NaSbO ₃	2.85	2.93	-22	2.81	2.85	-46	2.75	2.78	-38
AgSbO ₃ /NaSbO ₃	2.73	2.73	-25	2.69	2.68	-54	2.65	2.64	-47
CdTiO ₃ /NaSbO ₃	2.80	2.53	-37	2.74	2.48	-72	2.67	2.41	-67
Ga ₂ O ₃ /GeMgO ₃	2.41	2.23	-71	2.39	2.21	-108	2.38	2.21	-110
CaSnO ₃ /In ₂ O ₃	2.43	2.52	-79	2.41	2.50	-108	2.40	2.48	-119
MgSiO ₃ /SiZnO ₃	2.22	2.25	-97	2.19	2.22	-145	2.20	2.25	-144

III. Band structures and densities of states of HSs in comparison to their 2D components as well as band structures with projection contributions

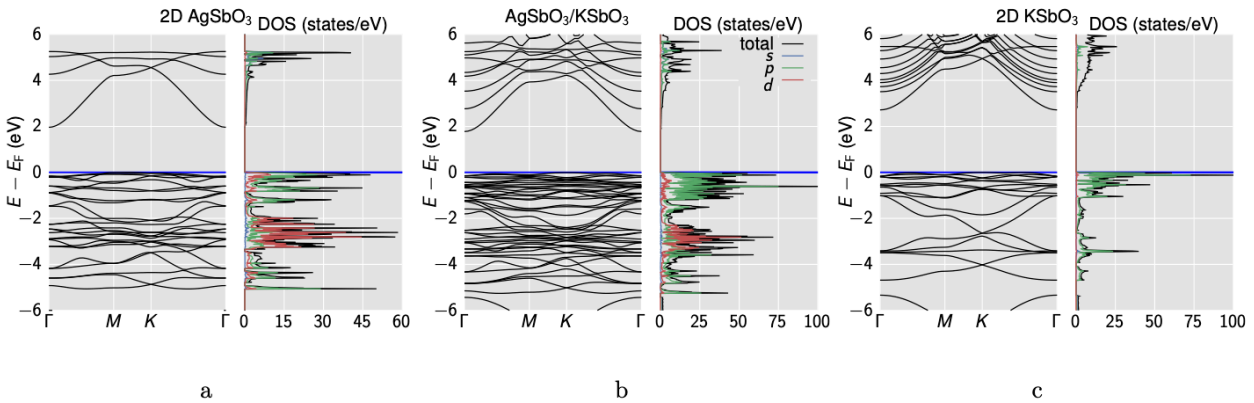


FIG. S2: Band structure and DOS for the individual 2D (a) AgSbO_3 , (c) KSbO_3 systems, and (b) the HS. The energies are aligned at the respective Fermi energy E_F . Note that the band structures are computed for geometries optimized with D3 dispersion correction.

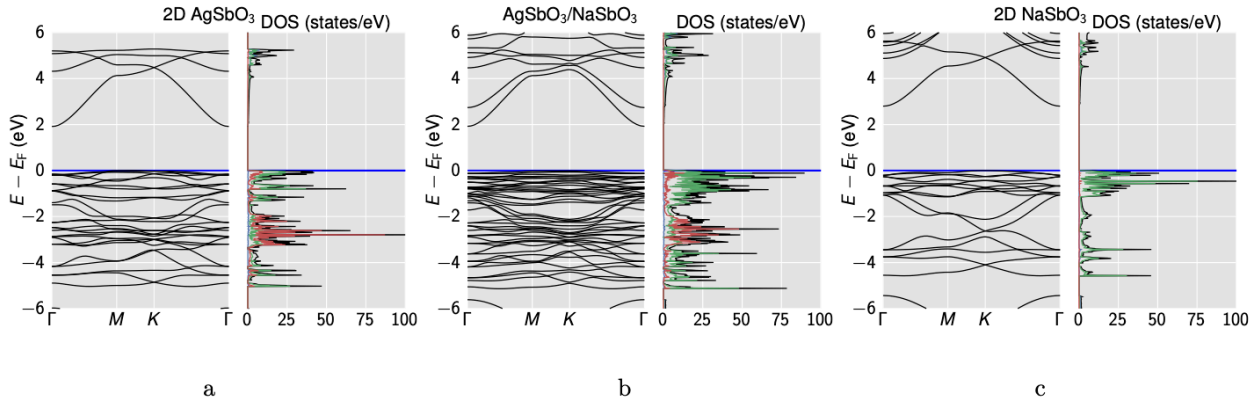


FIG. S3: Band structure and DOS for the individual 2D (a) AgSbO_3 , (c) NaSbO_3 systems, and (b) the HS. The energies are aligned at the respective Fermi energy E_F .

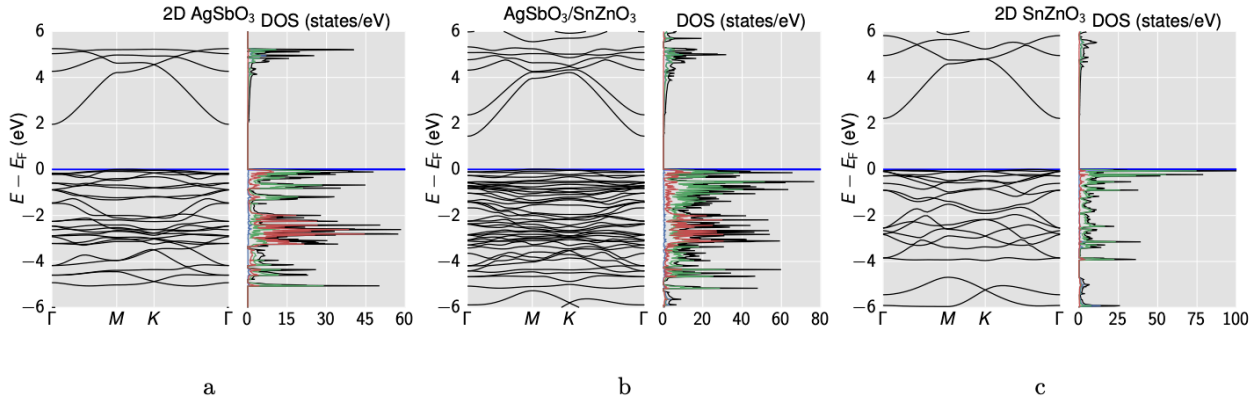


FIG. S4: Band structure and DOS for the individual 2D (a) AgSbO_3 , (c) SnZnO_3 systems, and (b) the HS. The energies are aligned at the respective Fermi energy E_F . Note that the band structures are computed for geometries optimized with D3 dispersion correction.

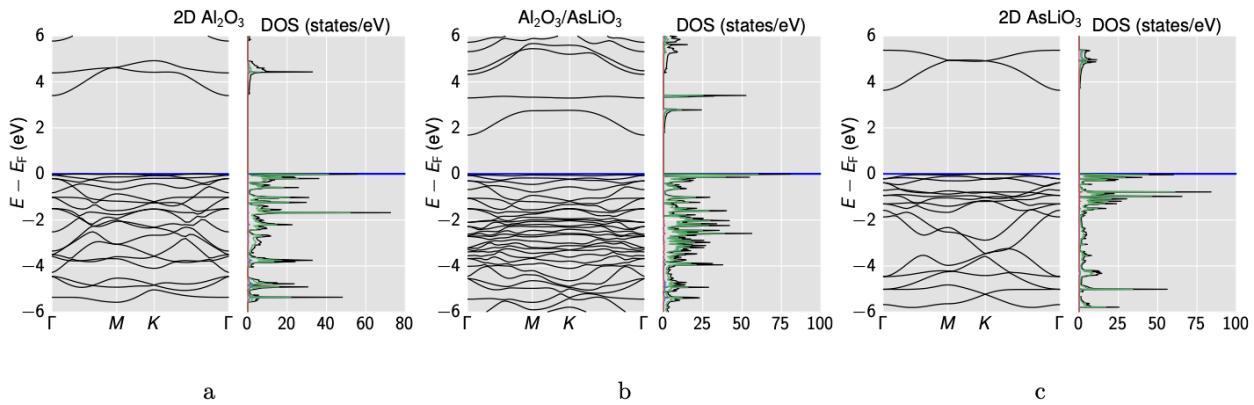


FIG. S5: Band structure and DOS for the individual 2D (a) Al_2O_3 , (c) AsLiO_3 systems, and (b) the HS. The energies are aligned at the respective Fermi energy E_F .

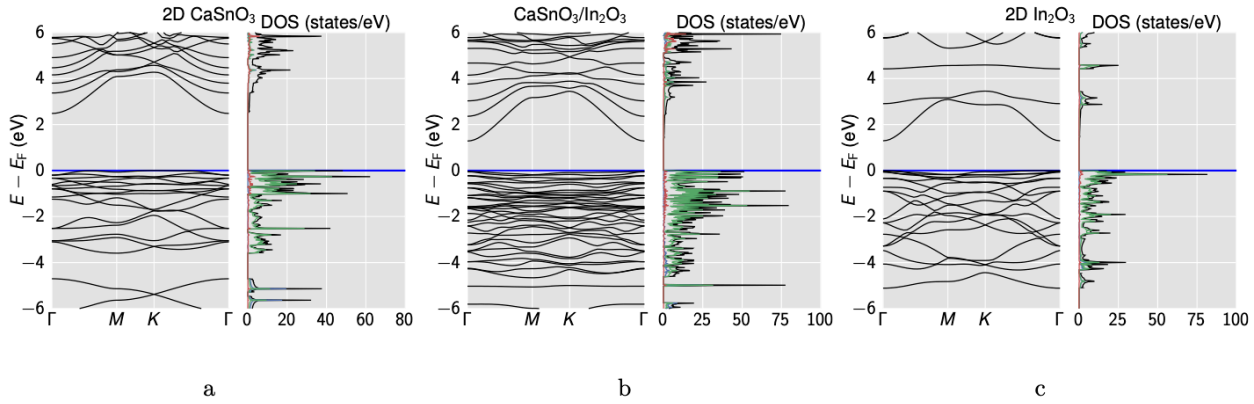


FIG. S6: Band structure and DOS for the individual 2D (a) CaSnO₃, (c) In₂O₃ systems, and (b) the HS. The energies are aligned at the respective Fermi energy E_F .

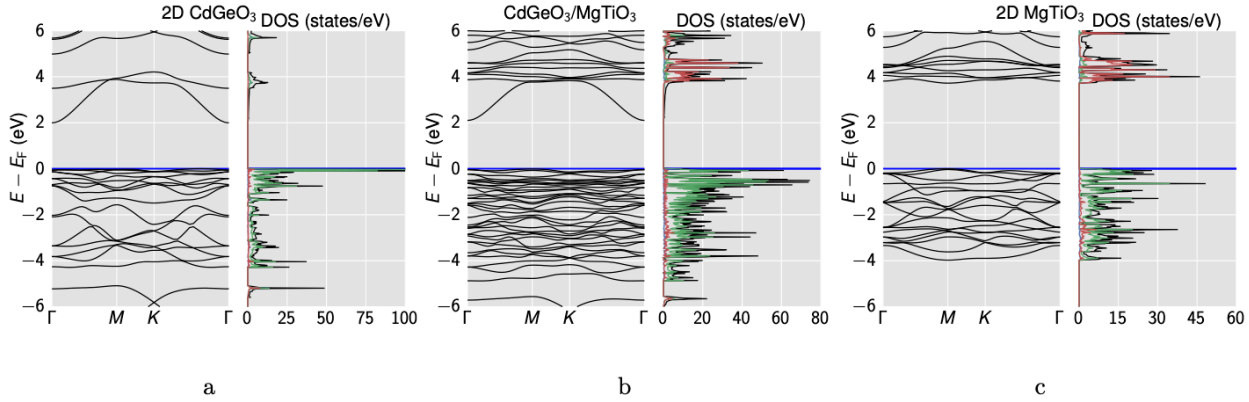


FIG. S7: Band structure and DOS for the individual 2D (a) CdGeO₃, (c) MgTiO₃ systems, and (b) the HS. The energies are aligned at the respective Fermi energy E_F .

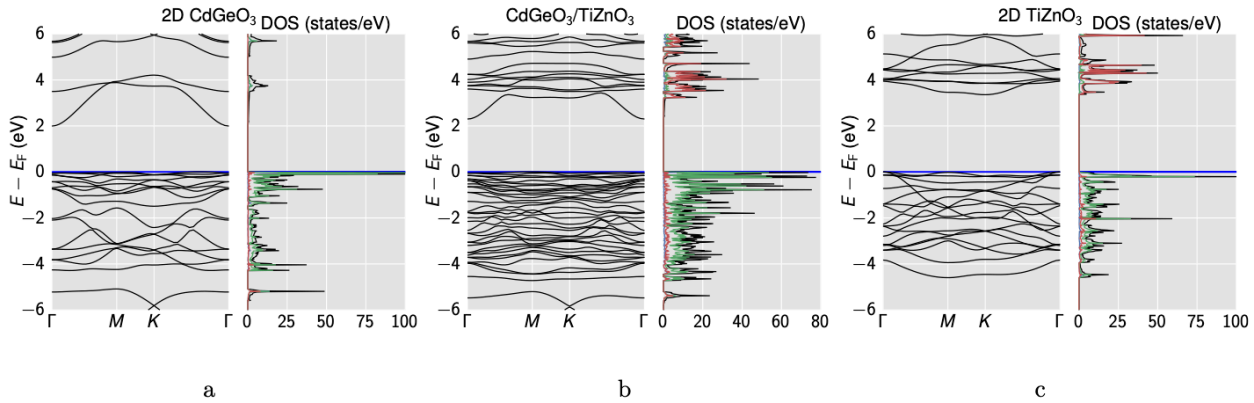


FIG. S8: Band structure and DOS for the individual 2D (a) CdGeO₃, (c) TiZnO₃ systems, and (b) the HS. The energies are aligned at the respective Fermi energy E_F .

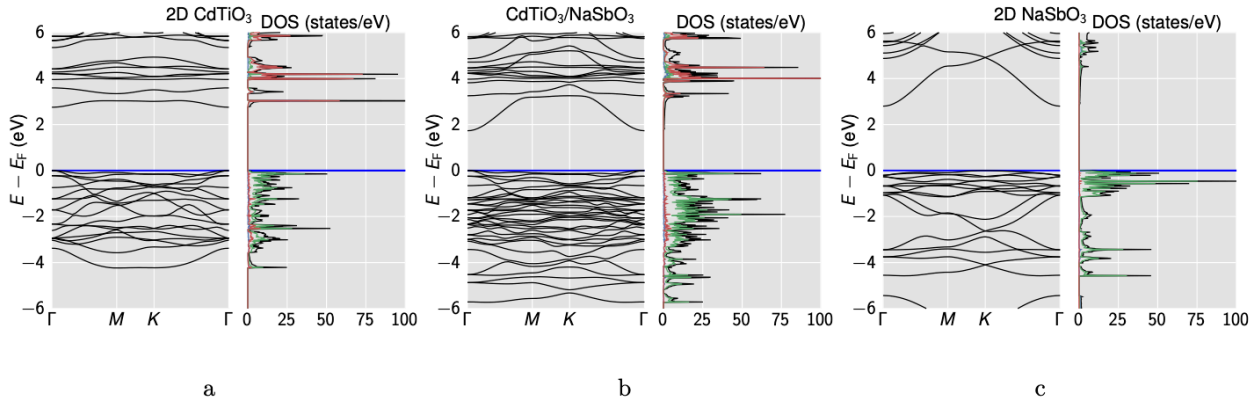


FIG. S9: Band structure and DOS for the individual 2D (a) CdTiO₃, (c) NaSbO₃ systems, and (b) the HS. The energies are aligned at the respective Fermi energy E_F .

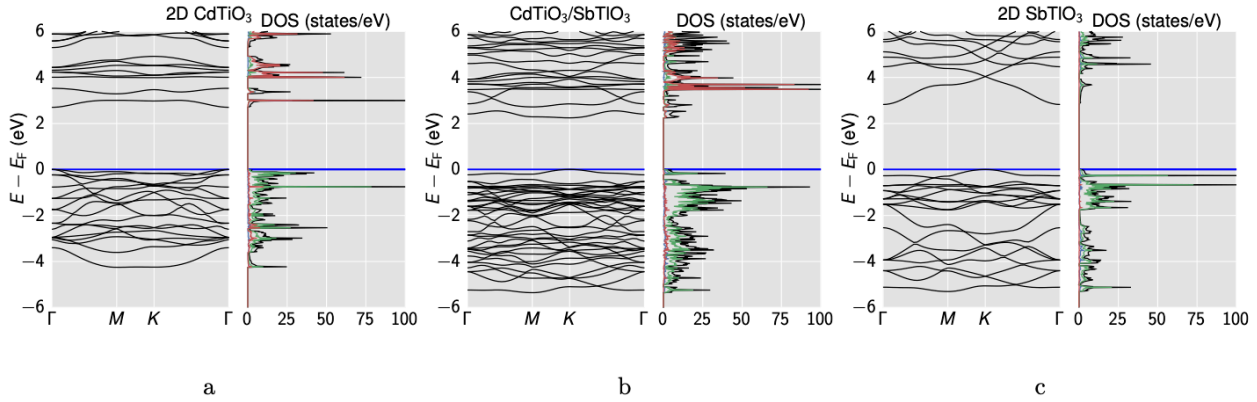


FIG. S10: Band structure and DOS for the individual 2D (a) CdTiO₃, (c) SbTiO₃ systems, and (b) the HS. The energies are aligned at the respective Fermi energy E_F . Note that the band structures are computed for geometries optimized with D3 dispersion correction.

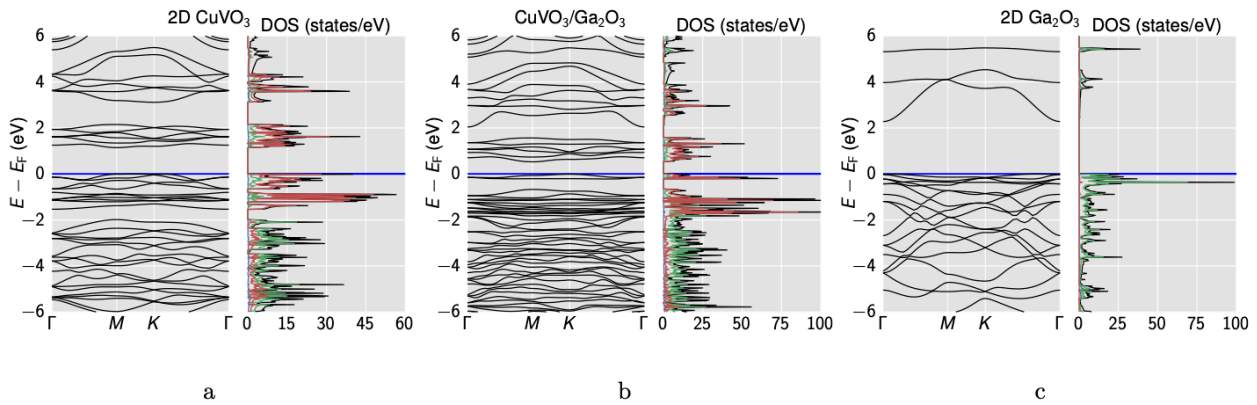


FIG. S11: Band structure and DOS for the individual 2D (a) CuVO₃, (c) Ga₂O₃ systems, and (b) the HS. The energies are aligned at the respective Fermi energy E_F .

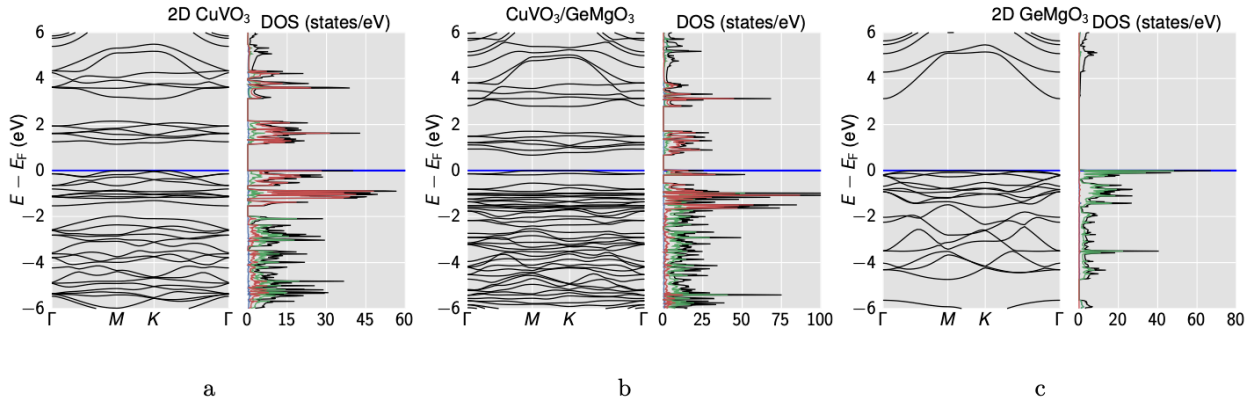


FIG. S12: Band structure and DOS for the individual 2D (a) CuVO₃, (c) GeMgO₃ systems, and (b) the HS. The energies are aligned at the respective Fermi energy E_F .

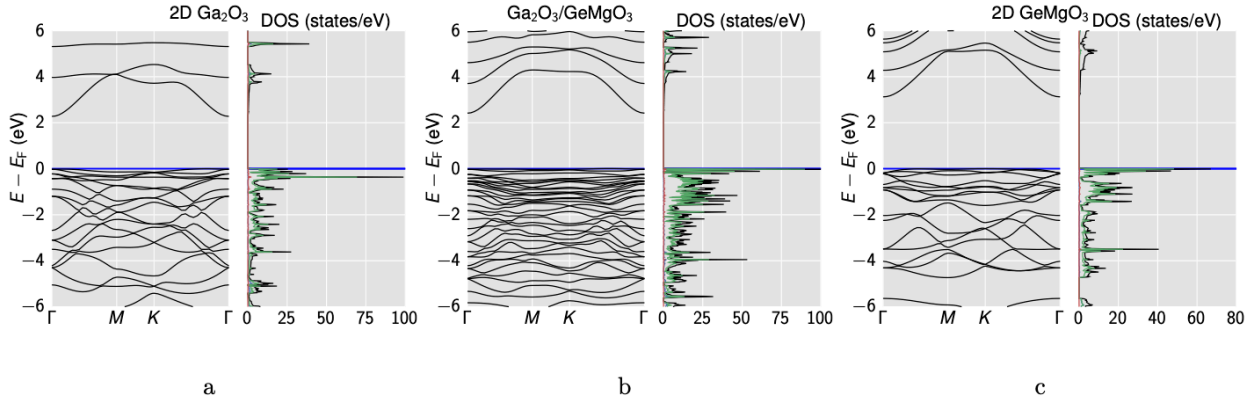


FIG. S13: Band structure and DOS for the individual 2D (a) Ga₂O₃, (c) GeMgO₃ systems, and (b) the HS. The energies are aligned at the respective Fermi energy E_F .

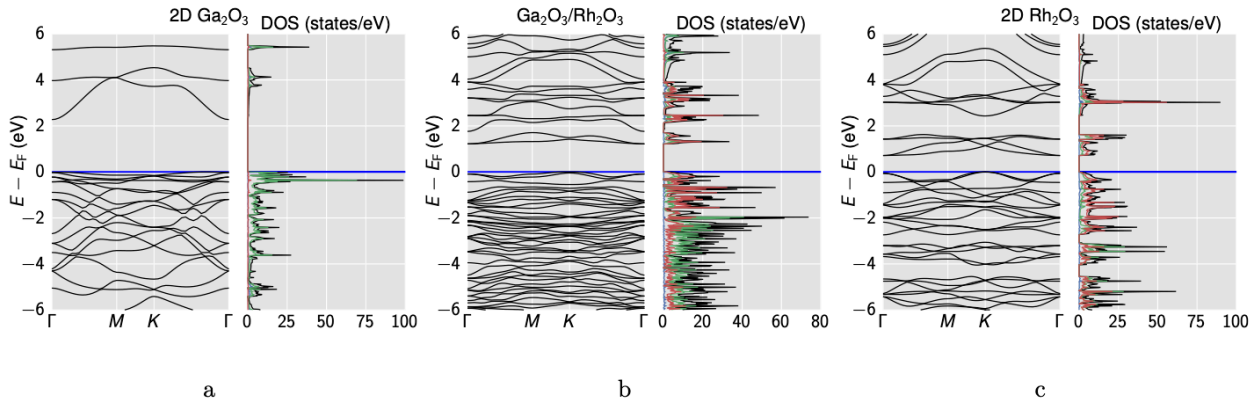


FIG. S14: Band structure and DOS for the individual 2D (a) Ga₂O₃, (c) Rh₂O₃ systems, and (b) the HS. The energies are aligned at the respective Fermi energy E_F .

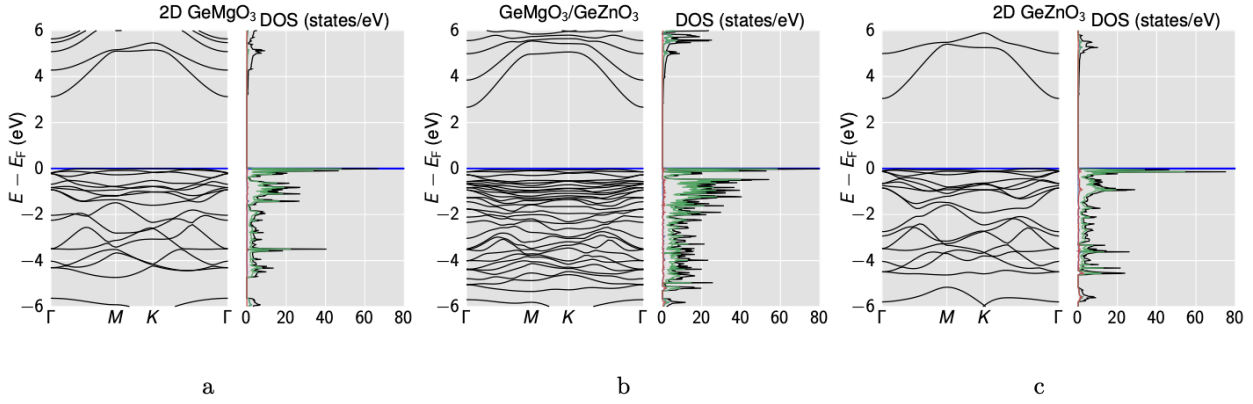


FIG. S15: Band structure and DOS for the individual 2D (a) GeMgO₃, (c) GeZnO₃ systems, and (b) the HS. The energies are aligned at the respective Fermi energy E_F .

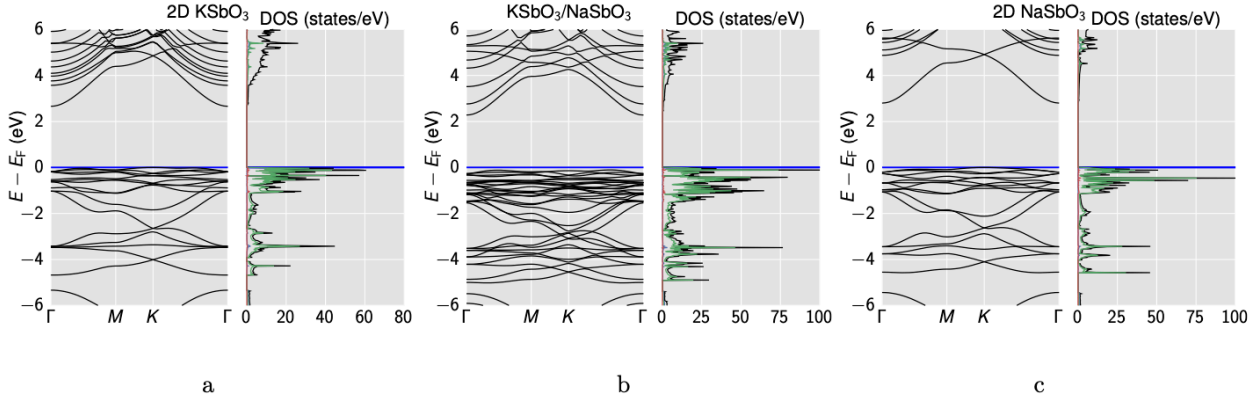


FIG. S16: Band structure and DOS for the individual 2D (a) KSbO₃, (c) NaSbO₃ systems, and (b) the HS. The energies are aligned at the respective Fermi energy E_F .

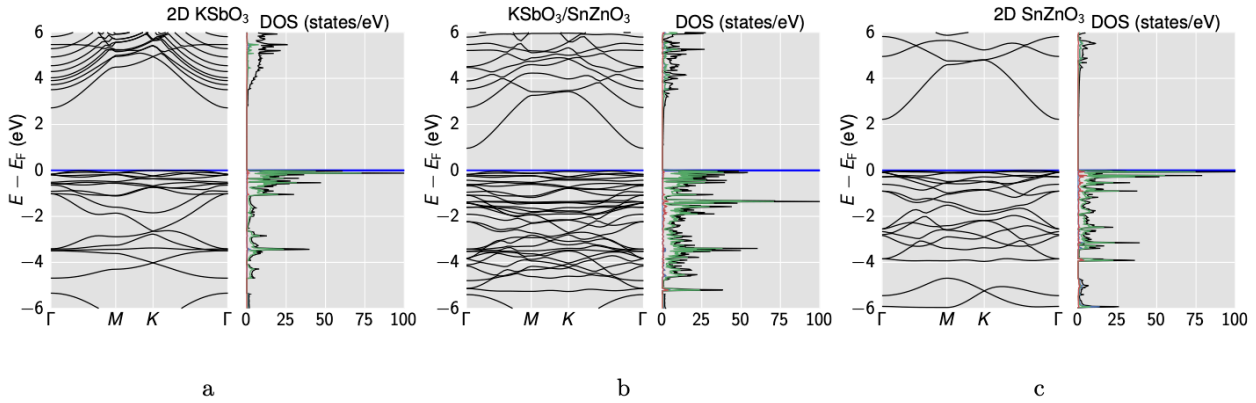


FIG. S17: Band structure and DOS for the individual 2D (a) KSbO₃, (c) SnZnO₃ systems, and (b) the HS. The energies are aligned at the respective Fermi energy E_F . Note that the band structures are computed for geometries optimized with D3 dispersion correction.

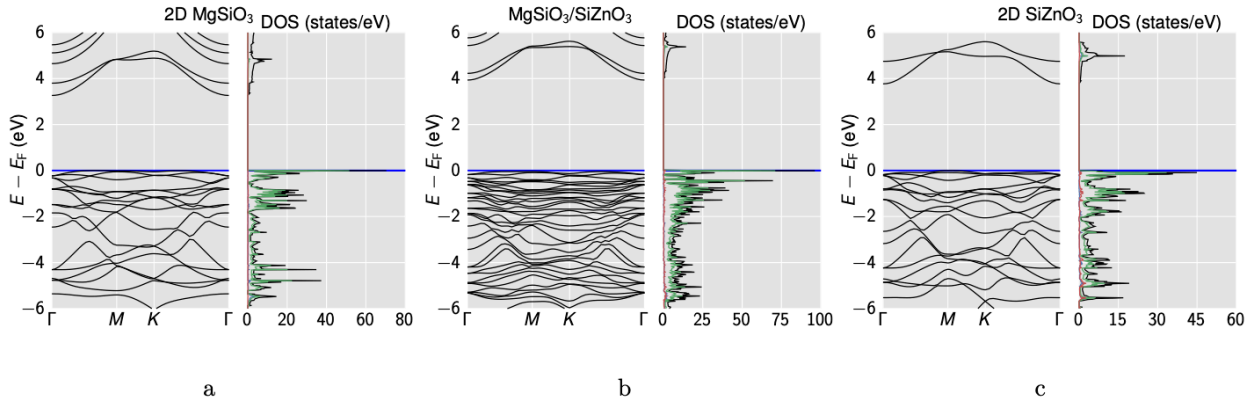


FIG. S18: Band structure and DOS for the individual 2D (a) MgSiO_3 , (c) SiZnO_3 systems, and (b) the HS. The energies are aligned at the respective Fermi energy E_F .

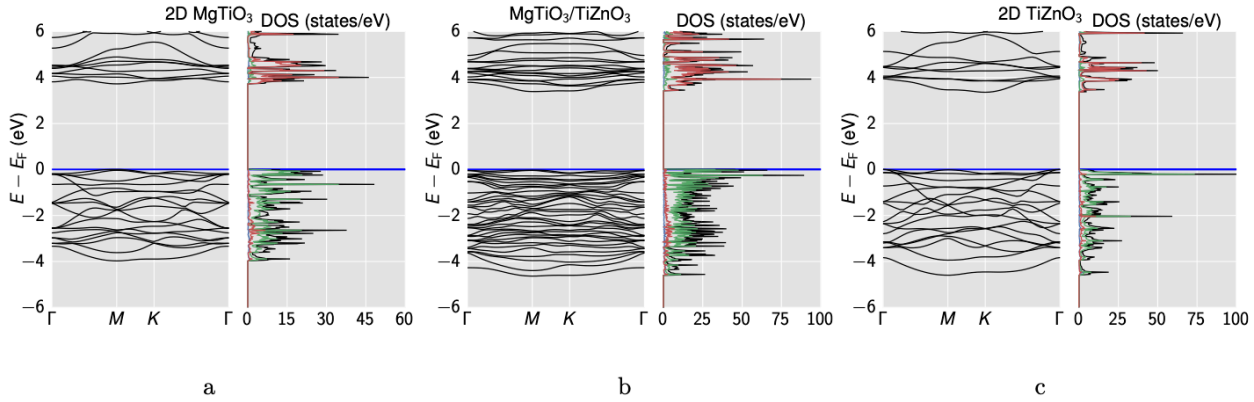


FIG. S19: Band structure and DOS for the individual 2D (a) MgTiO_3 , (c) TiZnO_3 systems, and (b) the HS. The energies are aligned at the respective Fermi energy E_F .

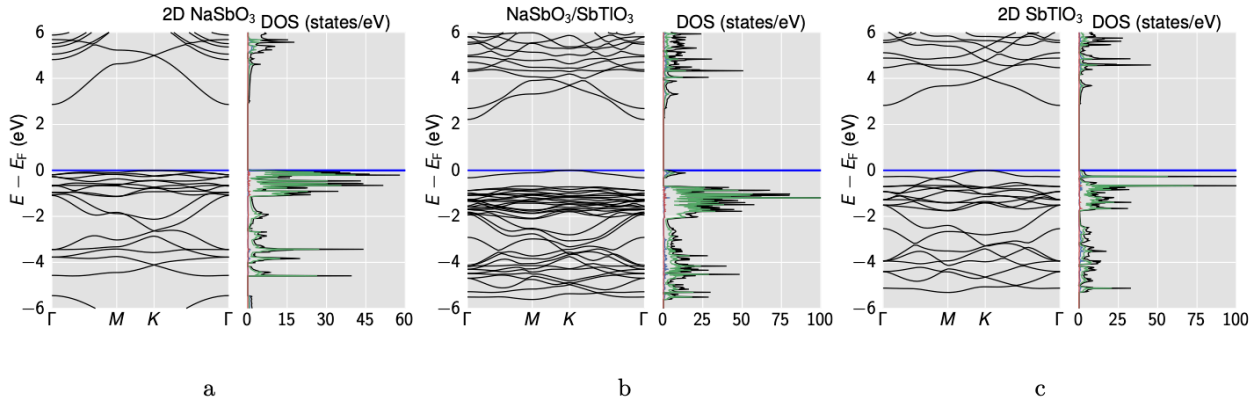


FIG. S20: Band structure and DOS for the individual 2D (a) NaSbO_3 , (c) SbTiO_3 systems, and (b) the HS. The energies are aligned at the respective Fermi energy E_F . Note that the band structures are computed for geometries optimized with D3 dispersion correction.

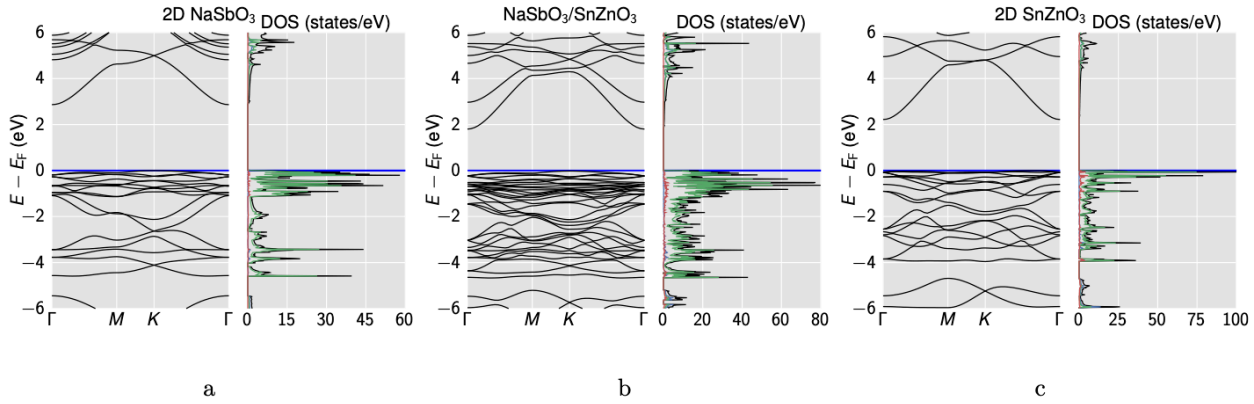


FIG. S21: Band structure and DOS for the individual 2D (a) NaSbO_3 , (c) SnZnO_3 systems, and (b) the HS. The energies are aligned at the respective Fermi energy E_F . Note that the band structures are computed for geometries optimized with D3 dispersion correction.

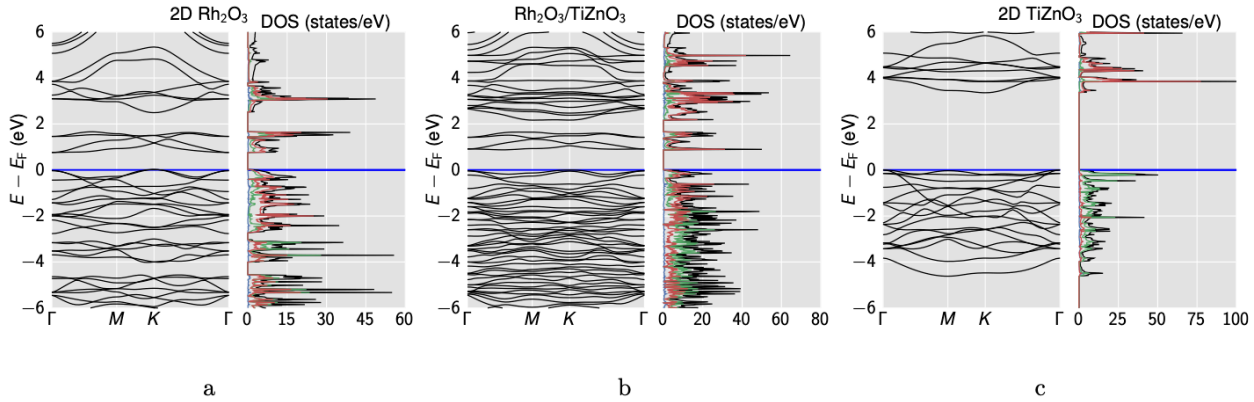


FIG. S22: Band structure and DOS for the individual 2D (a) Rh_2O_3 , (c) TiZnO_3 systems, and (b) the HS. The energies are aligned at the respective Fermi energy E_F . Note that the band structures are computed for geometries optimized with D3 dispersion correction.

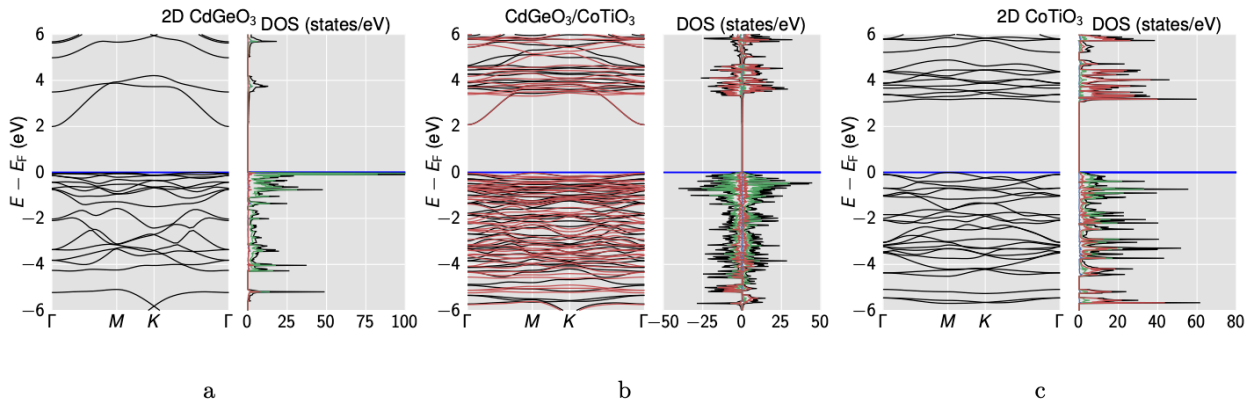


FIG. S23: Band structure and DOS for the individual 2D (a) CdGeO_3 , (c) CoTiO_3 systems, and (b) the HS. The energies are aligned at the respective Fermi energy E_F . For the spin polarized band structure, majority spin bands (positive DOS) are indicated in black while minority spin bands (negative DOS) are in red.

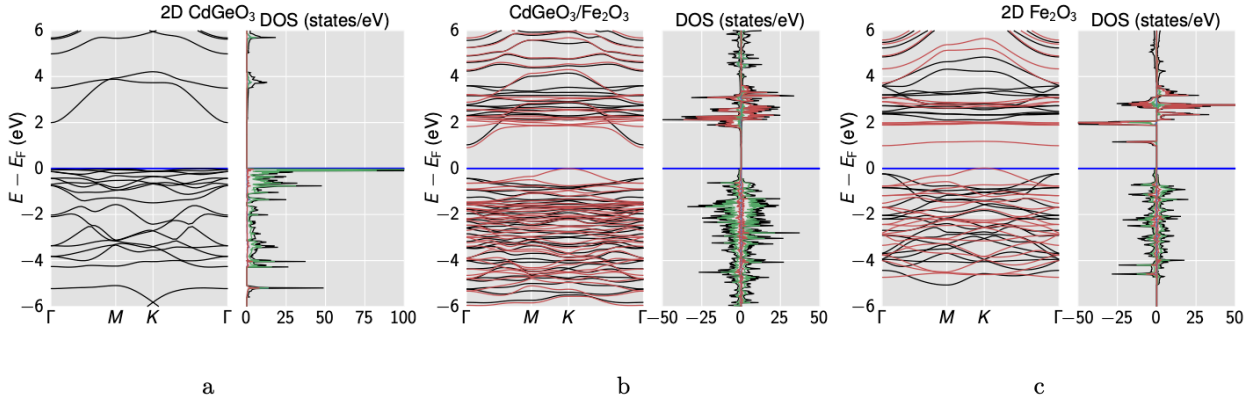


FIG. S24: Band structure and DOS for the individual 2D (a) CdGeO₃, (c) Fe₂O₃ systems, and (b) the HS. The energies are aligned at the respective Fermi energy E_F .

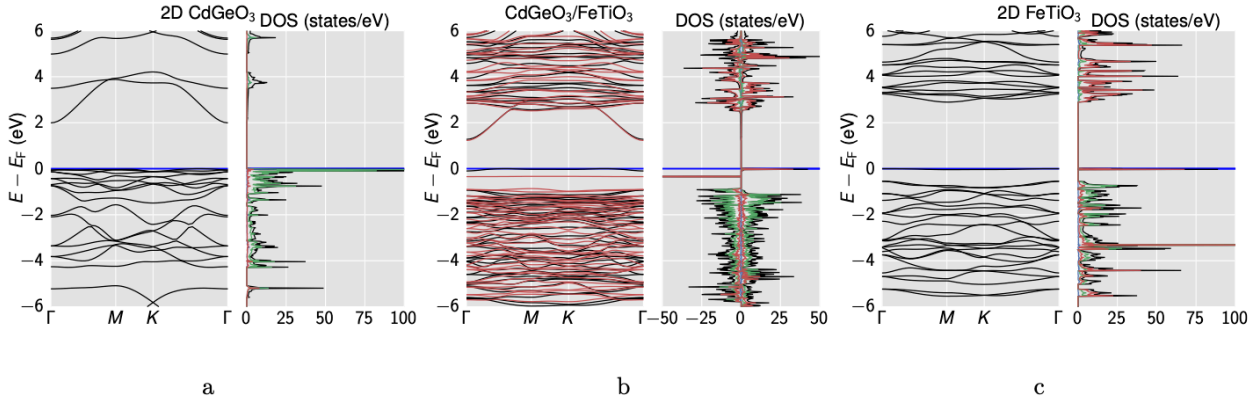


FIG. S25: Band structure and DOS for the individual 2D (a) CdGeO₃, (c) FeTiO₃ systems, and (b) the HS. The energies are aligned at the respective Fermi energy E_F .

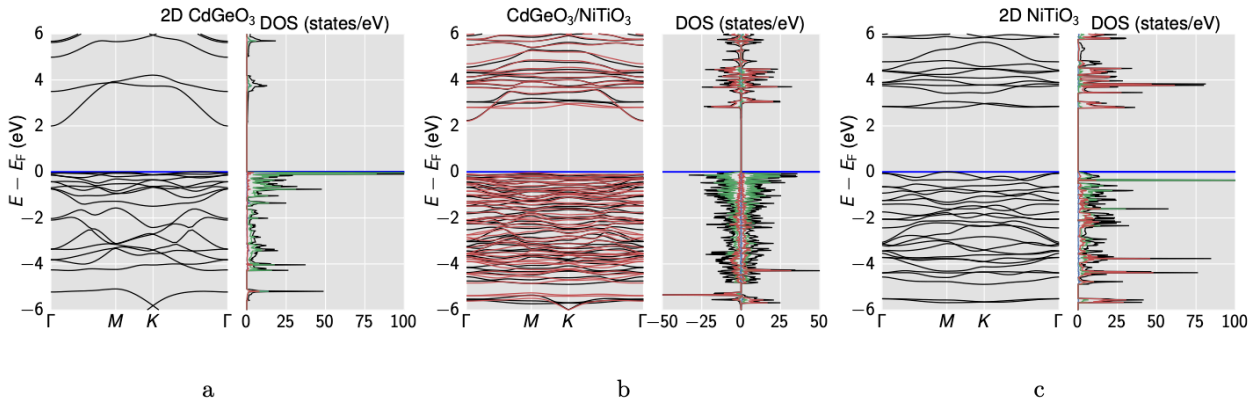


FIG. S26: Band structure and DOS for the individual 2D (a) CdGeO₃, (c) NiTiO₃ systems, and (b) the HS. The energies are aligned at the respective Fermi energy E_F .

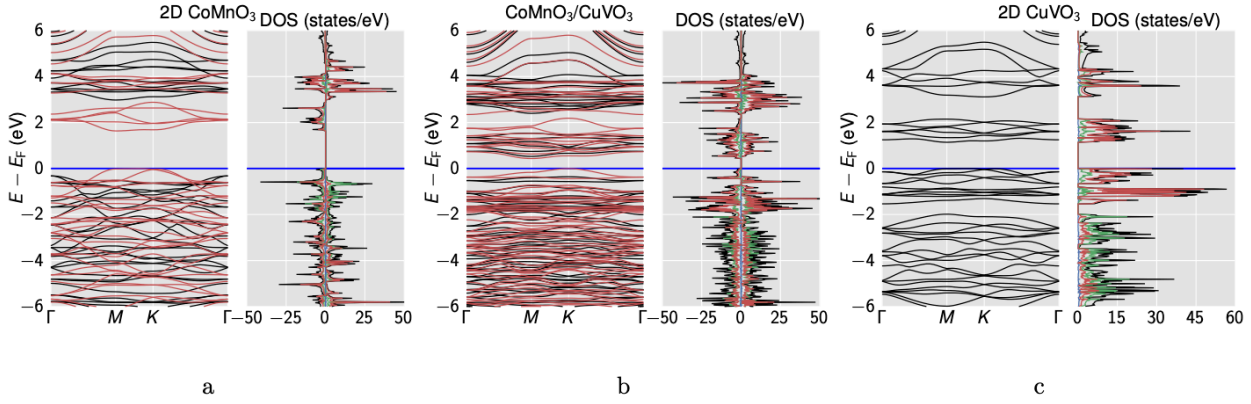


FIG. S27: Band structure and DOS for the individual 2D (a) CoMnO₃, (c) CuVO₃ systems, and (b) the HS. The energies are aligned at the respective Fermi energy E_F .

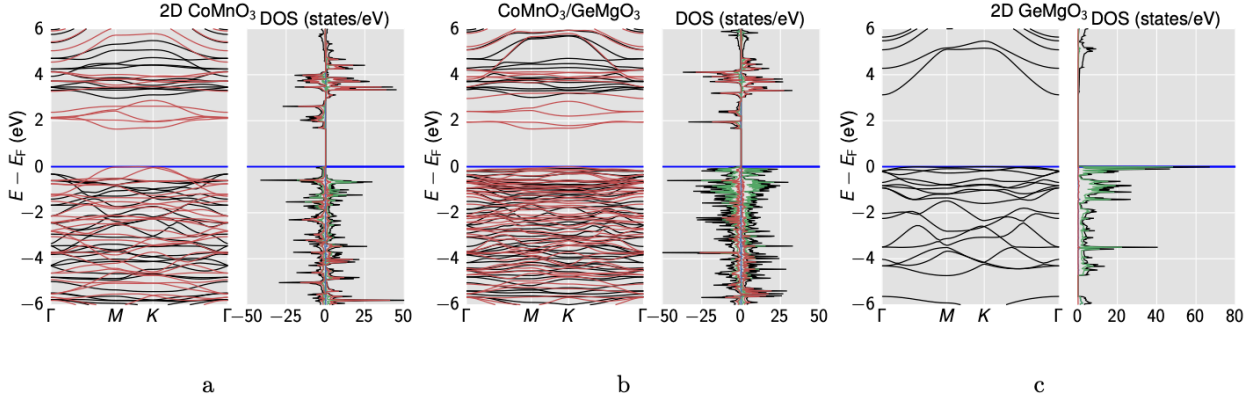


FIG. S28: Band structure and DOS for the individual 2D (a) CoMnO₃, (c) GeMgO₃ systems, and (b) the HS. The energies are aligned at the respective Fermi energy E_F .

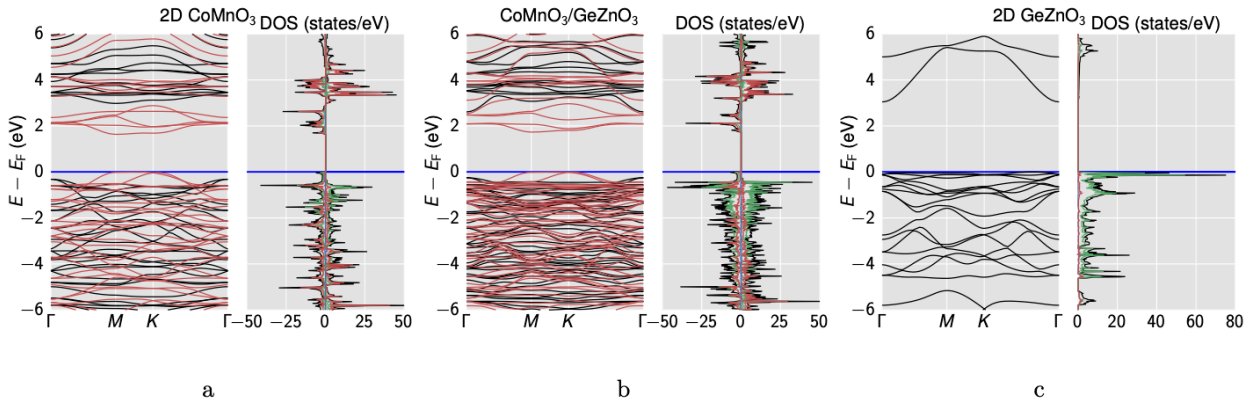


FIG. S29: Band structure and DOS for the individual 2D (a) CoMnO₃, (c) GeZnO₃ systems, and (b) the HS. The energies are aligned at the respective Fermi energy E_F .

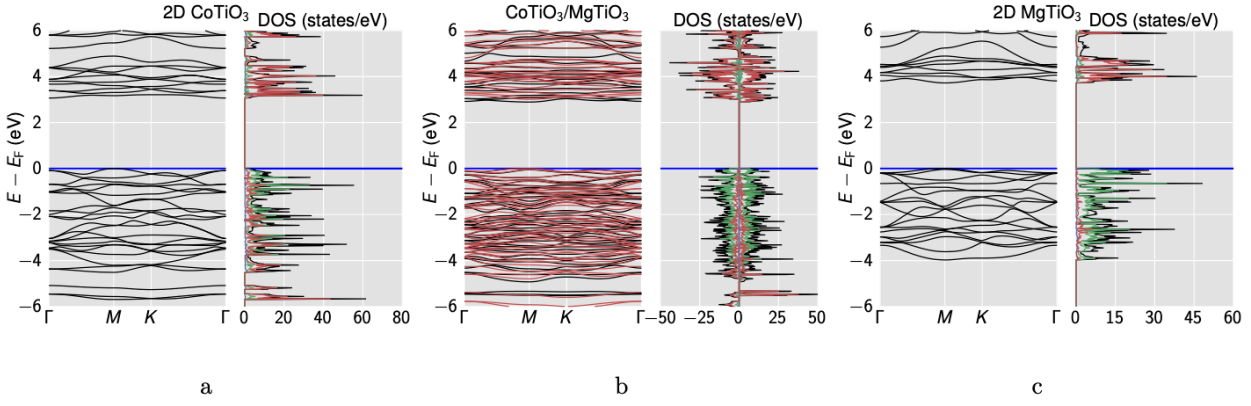


FIG. S30: Band structure and DOS for the individual 2D (a) CoTiO₃, (c) MgTiO₃ systems, and (b) the HS. The energies are aligned at the respective Fermi energy E_F .

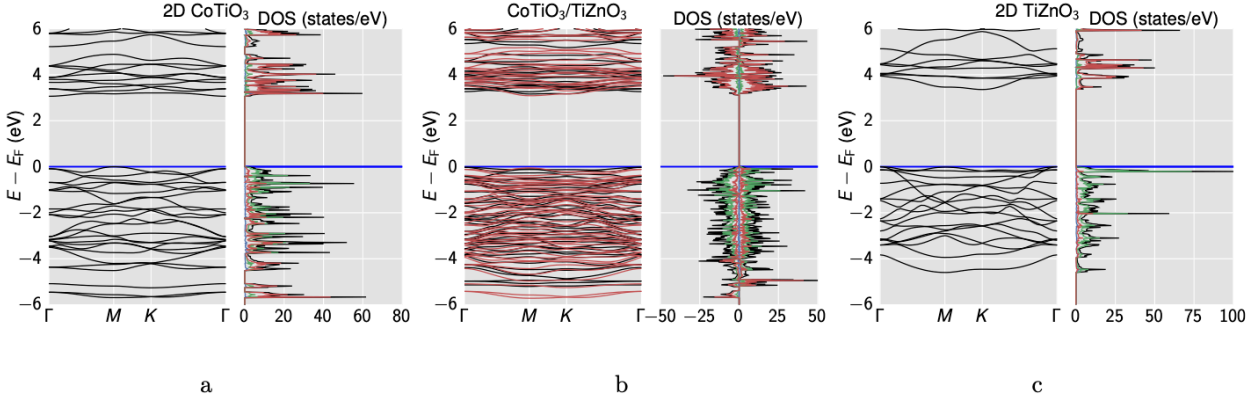


FIG. S31: Band structure and DOS for the individual 2D (a) CoTiO₃, (c) TiZnO₃ systems, and (b) the HS. The energies are aligned at the respective Fermi energy E_F .

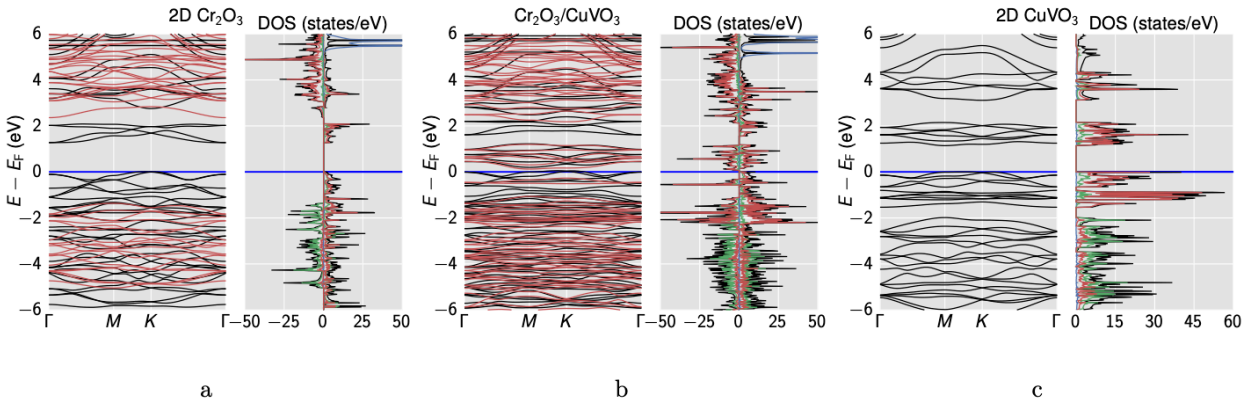


FIG. S32: Band structure and DOS for the individual 2D (a) Cr₂O₃, (c) CuVO₃ systems, and (b) the HS. The energies are aligned at the respective Fermi energy E_F .

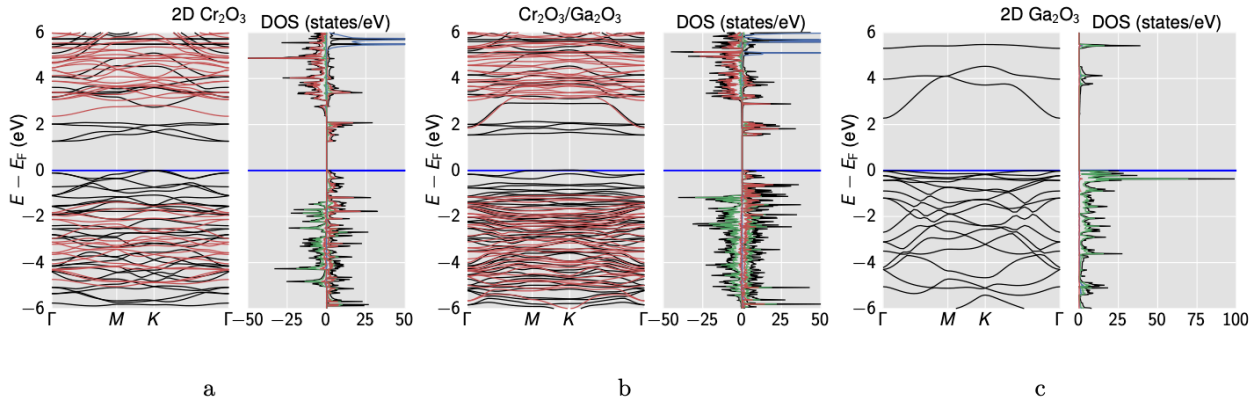


FIG. S33: Band structure and DOS for the individual 2D (a) Cr₂O₃, (c) Ga₂O₃ systems, and (b) the HS. The energies are aligned at the respective Fermi energy E_F .

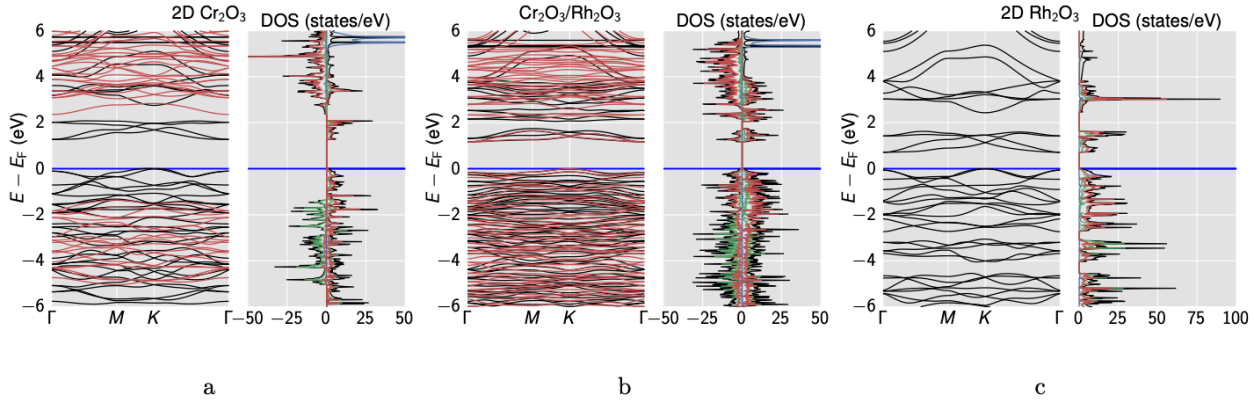


FIG. S34: Band structure and DOS for the individual 2D (a) Cr₂O₃, (c) Rh₂O₃ systems, and (b) the HS. The energies are aligned at the respective Fermi energy E_F .

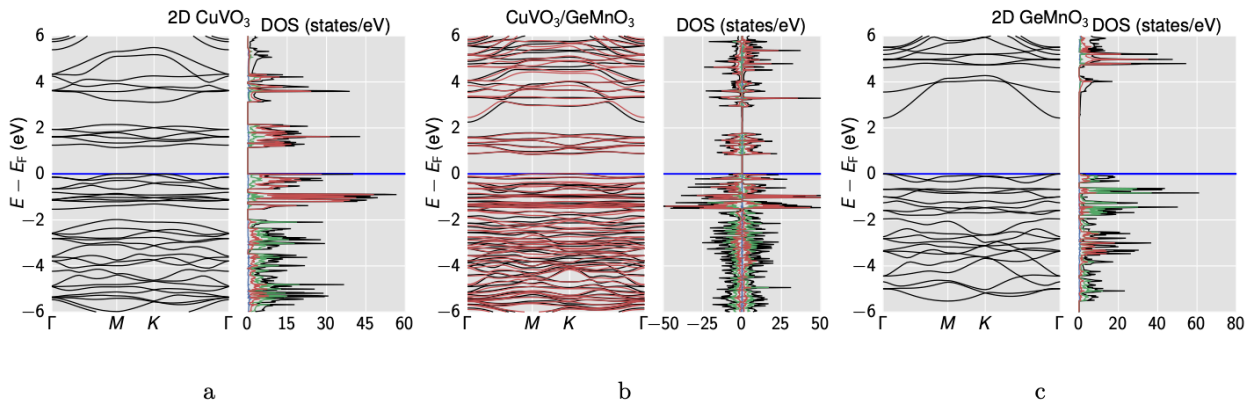


FIG. S35: Band structure and DOS for the individual 2D (a) CuVO₃, (c) GeMnO₃ systems, and (b) the HS. The energies are aligned at the respective Fermi energy E_F .

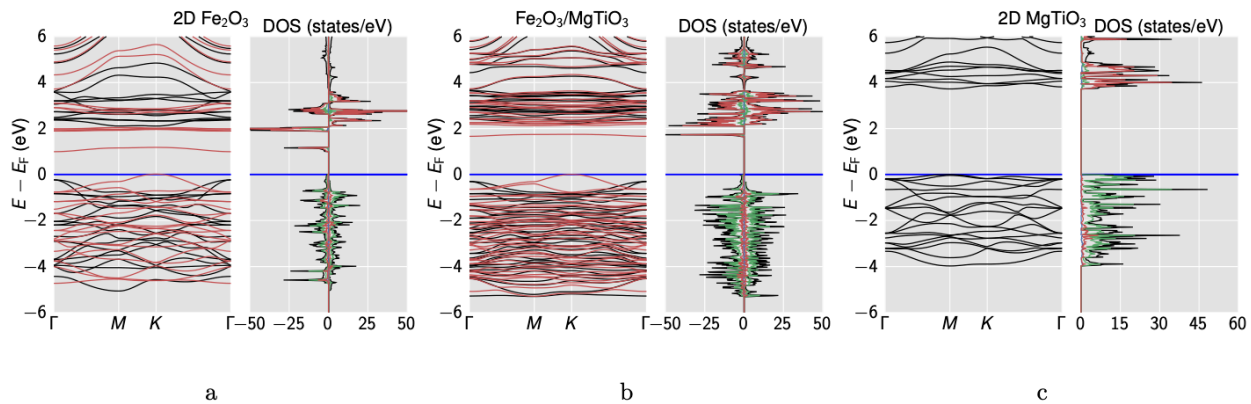


FIG. S36: Band structure and DOS for the individual 2D (a) Fe_2O_3 , (c) MgTiO_3 systems, and (b) the HS. The energies are aligned at the respective Fermi energy E_F .

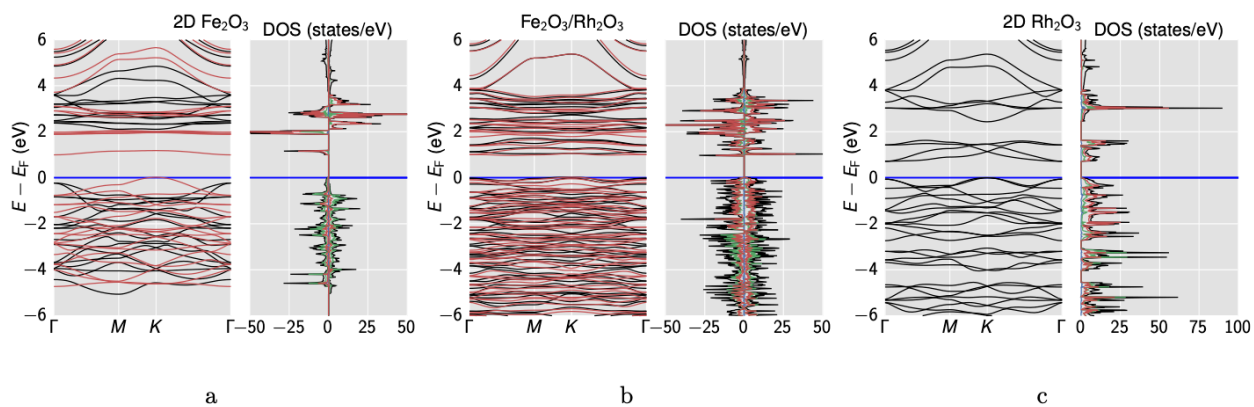


FIG. S37: Band structure and DOS for the individual 2D (a) Fe_2O_3 , (c) Rh_2O_3 systems, and (b) the HS. The energies are aligned at the respective Fermi energy E_F .

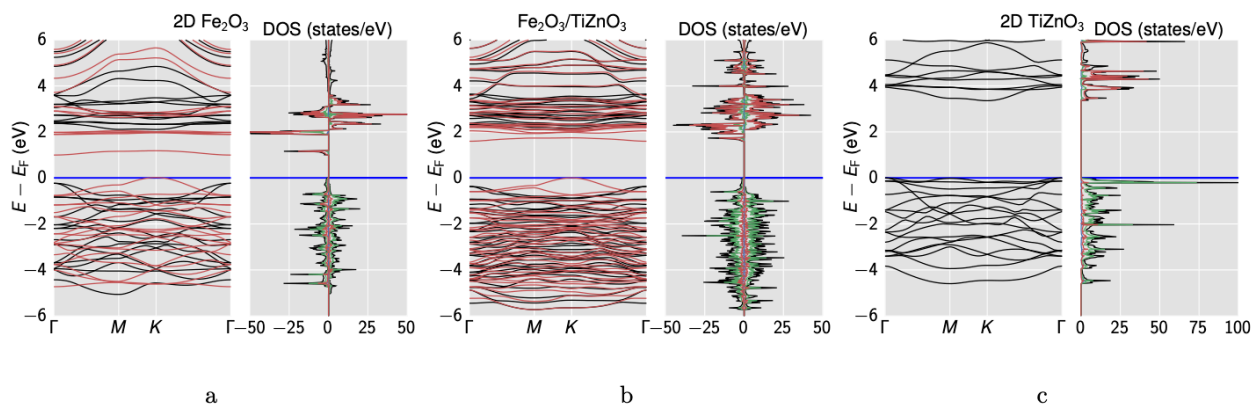


FIG. S38: Band structure and DOS for the individual 2D (a) Fe_2O_3 , (c) TiZnO_3 systems, and (b) the HS. The energies are aligned at the respective Fermi energy E_F .

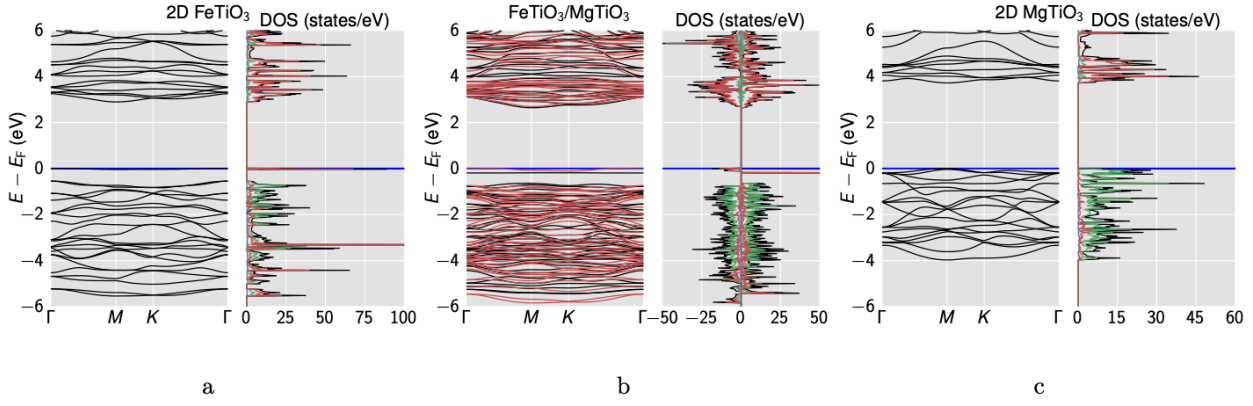


FIG. S39: Band structure and DOS for the individual 2D (a) FeTiO₃, (c) MgTiO₃ systems, and (b) the HS. The energies are aligned at the respective Fermi energy E_F .

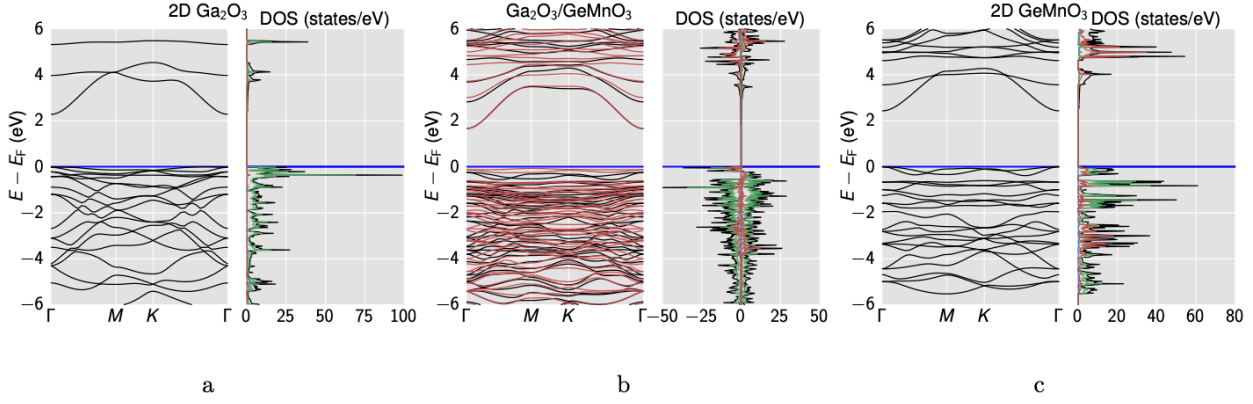


FIG. S40: Band structure and DOS for the individual 2D (a) Ga₂O₃, (c) GeMnO₃ systems, and (b) the HS. The energies are aligned at the respective Fermi energy E_F .

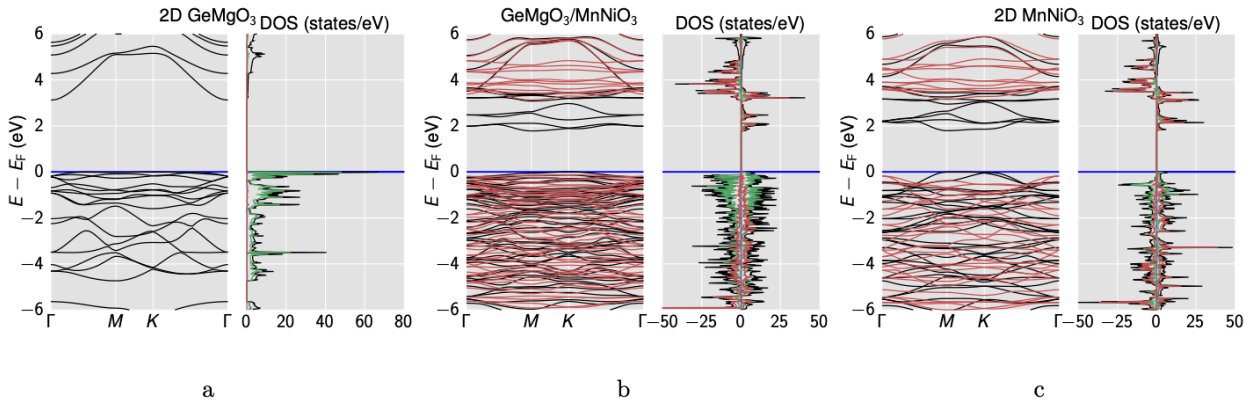


FIG. S41: Band structure and DOS for the individual 2D (a) GeMgO₃, (c) MnNiO₃ systems, and (b) the HS. The energies are aligned at the respective Fermi energy E_F .

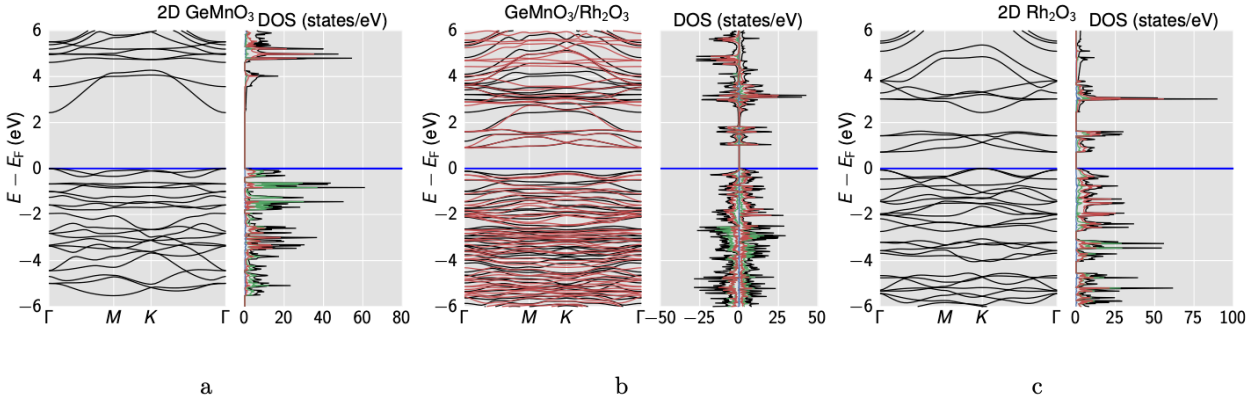


FIG. S42: Band structure and DOS for the individual 2D (a) GeMnO₃, (c) Rh₂O₃ systems, and (b) the HS. The energies are aligned at the respective Fermi energy E_F .

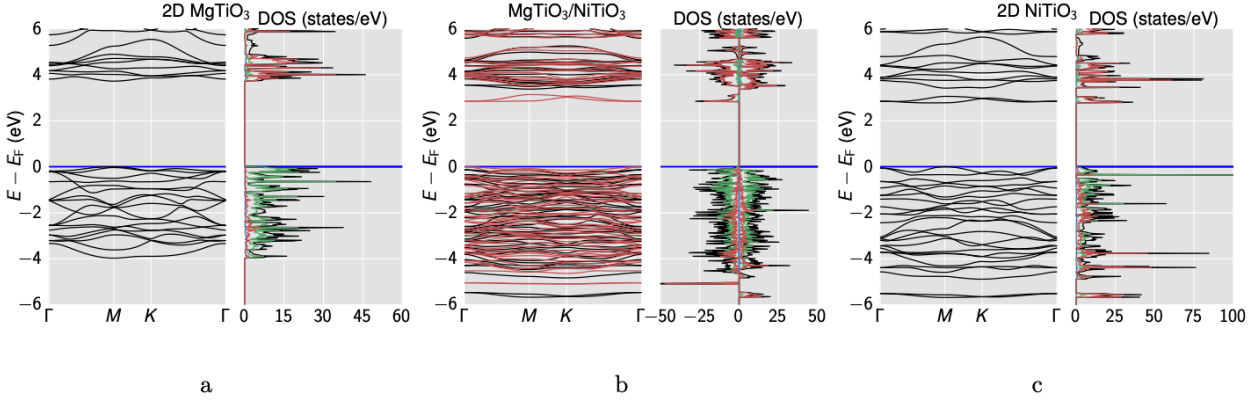


FIG. S43: Band structure and DOS for the individual 2D (a) MgTiO₃, (c) NiTiO₃ systems, and (b) the HS. The energies are aligned at the respective Fermi energy E_F .

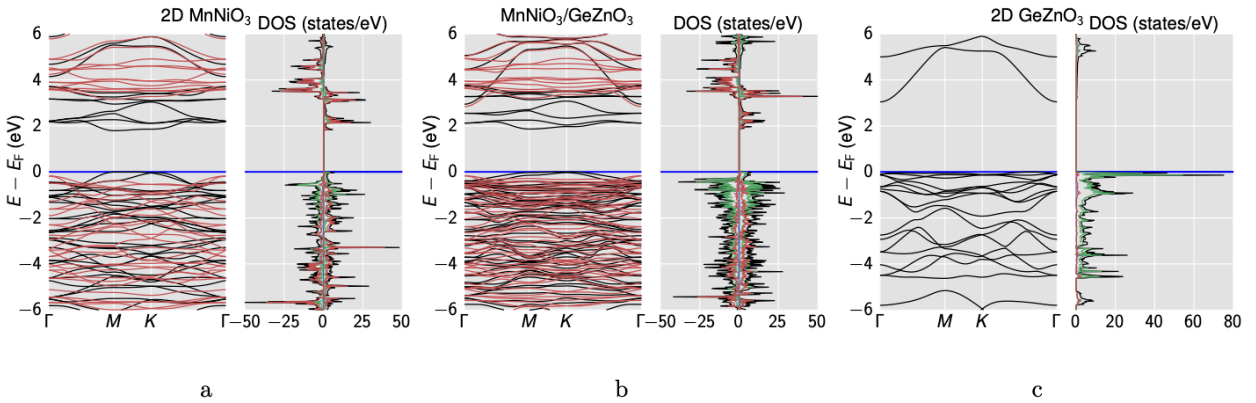


FIG. S44: Band structure and DOS for the individual 2D (a) MnNiO₃, (c) GeZnO₃ systems, and (b) the HS. The energies are aligned at the respective Fermi energy E_F .

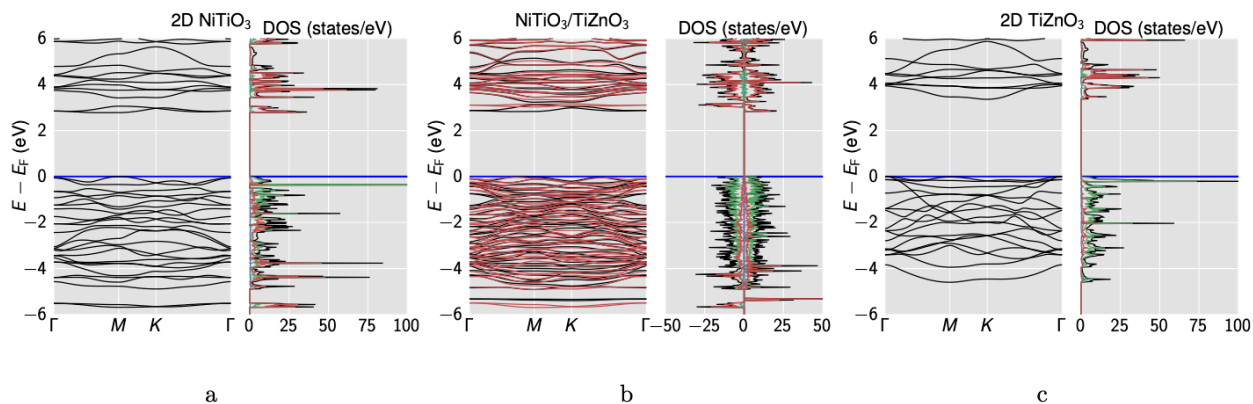


FIG. S45: Band structure and DOS for the individual 2D (a) NiTiO₃, (c) TiZnO₃ systems, and (b) the HS. The energies are aligned at the respective Fermi energy E_F .

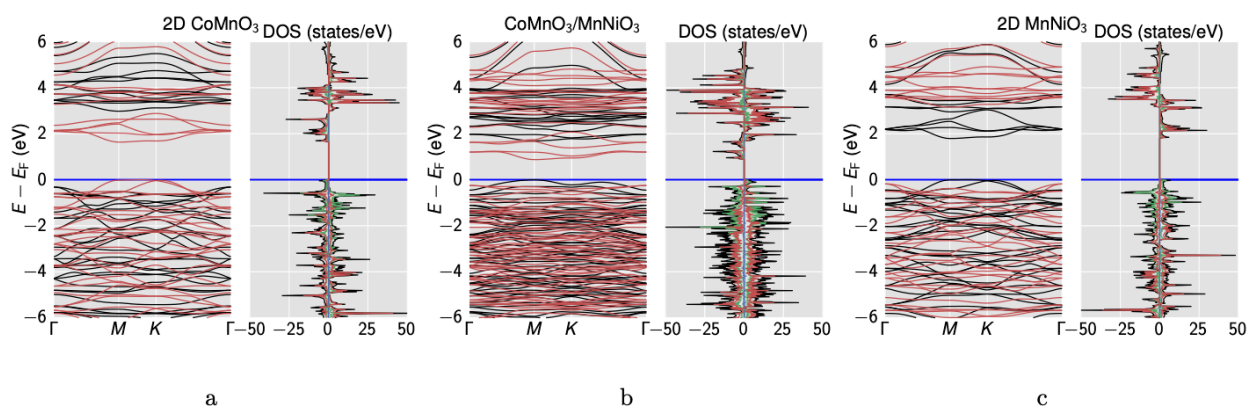


FIG. S46: Band structure and DOS for the individual 2D (a) CoMnO₃, (c) MnNiO₃ systems, and (b) the HS. The energies are aligned at the respective Fermi energy E_F .

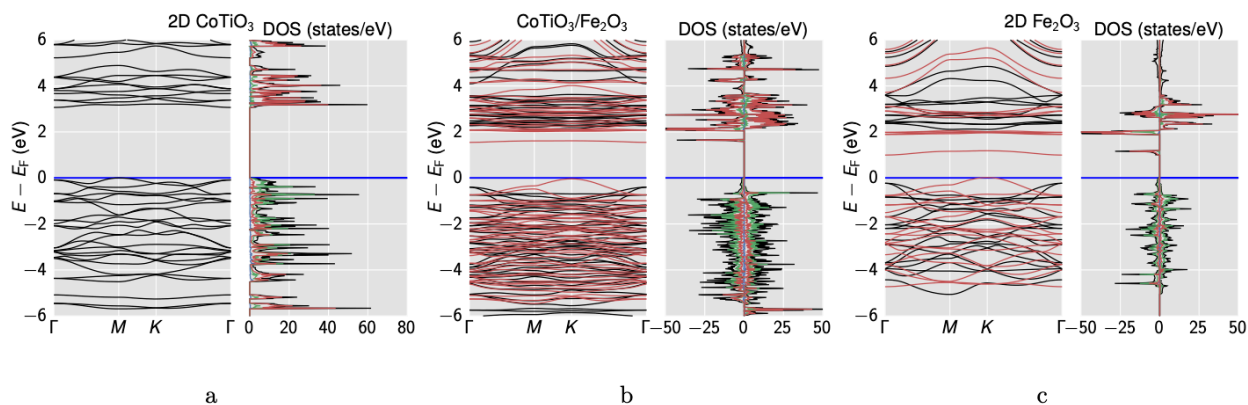


FIG. S47: Band structure and DOS for the individual 2D (a) CoTiO₃, (c) Fe₂O₃ systems, and (b) the HS. The energies are aligned at the respective Fermi energy E_F .

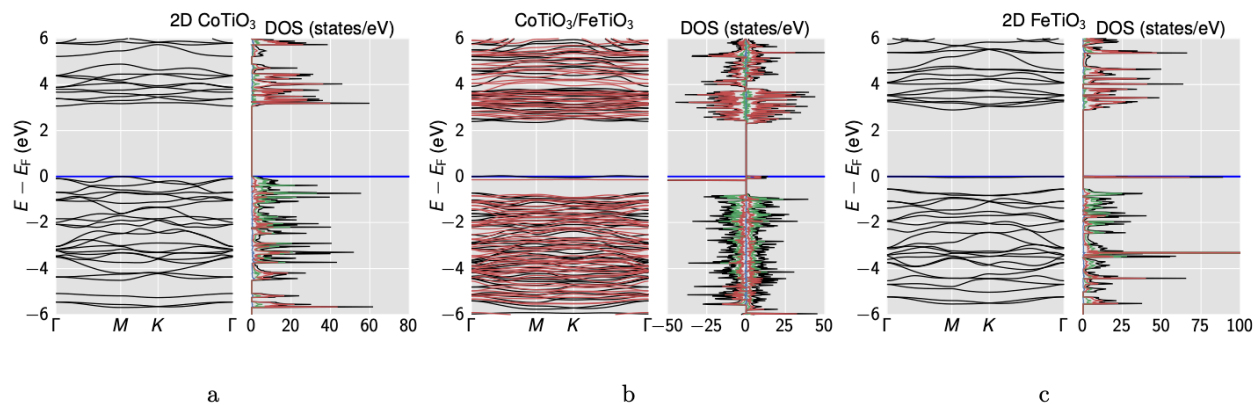


FIG. S48: Band structure and DOS for the individual 2D (a) CoTiO_3 , (c) FeTiO_3 systems, and (b) the HS. The energies are aligned at the respective Fermi energy E_F .

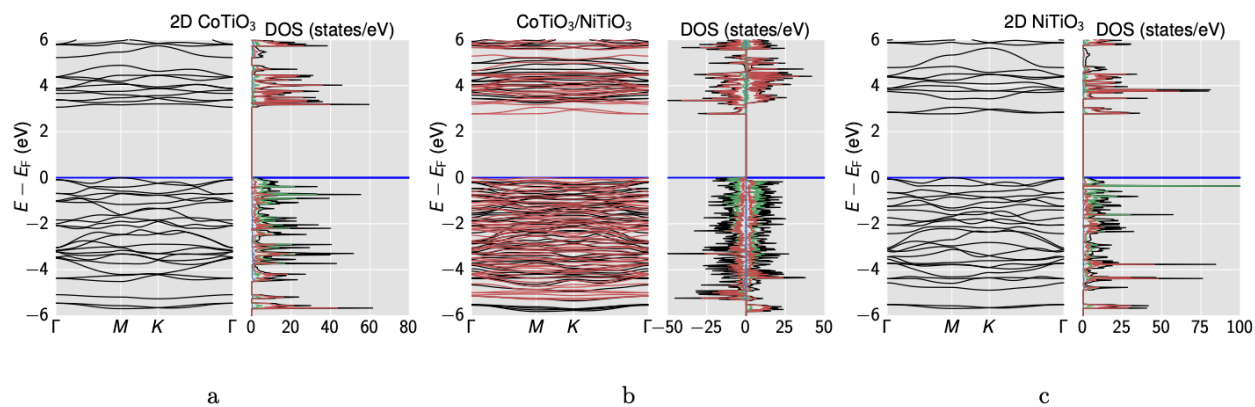


FIG. S49: Band structure and DOS for the individual 2D (a) CoTiO_3 , (c) NiTiO_3 systems, and (b) the HS. The energies are aligned at the respective Fermi energy E_F .

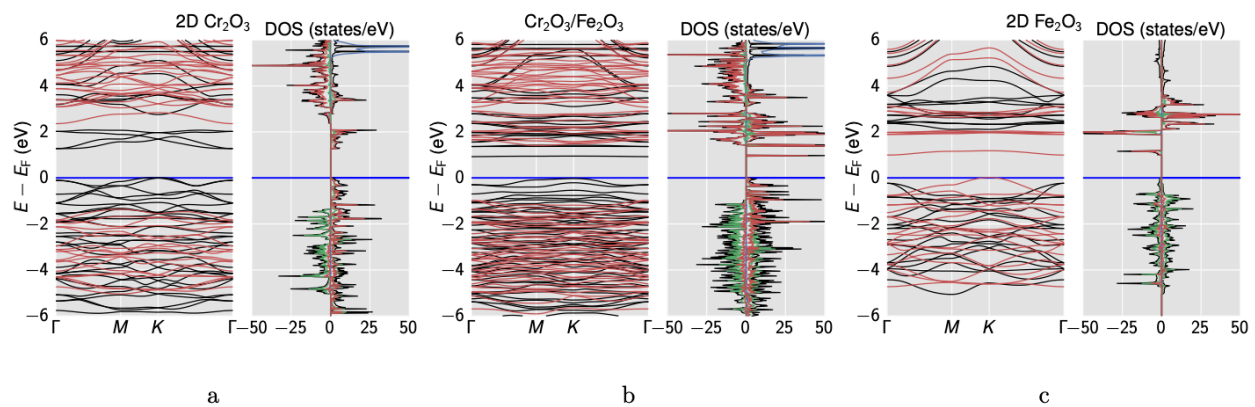


FIG. S50: Band structure and DOS for the individual 2D (a) Cr_2O_3 , (c) Fe_2O_3 systems, and (b) the HS. The energies are aligned at the respective Fermi energy E_F .

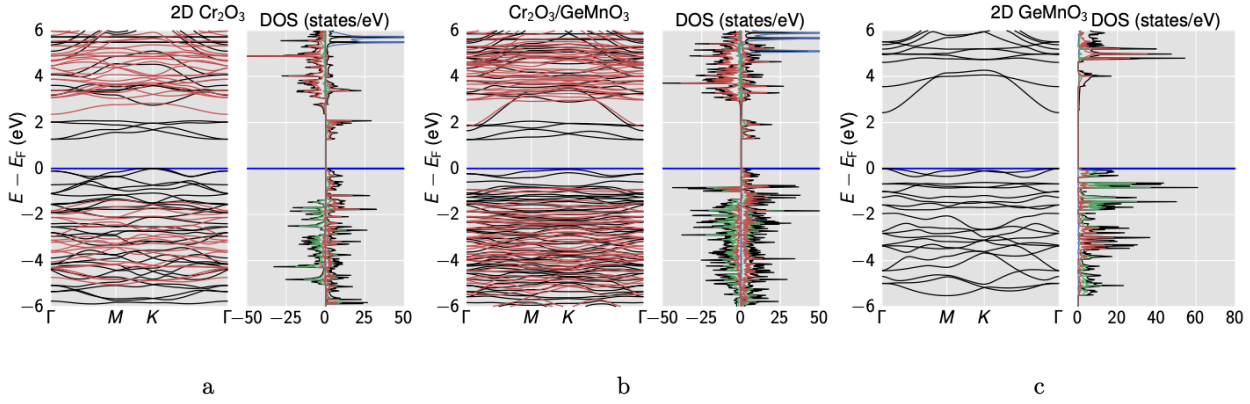


FIG. S51: Band structure and DOS for the individual 2D (a) Cr₂O₃, (c) GeMnO₃ systems, and (b) the HS. The energies are aligned at the respective Fermi energy E_F .

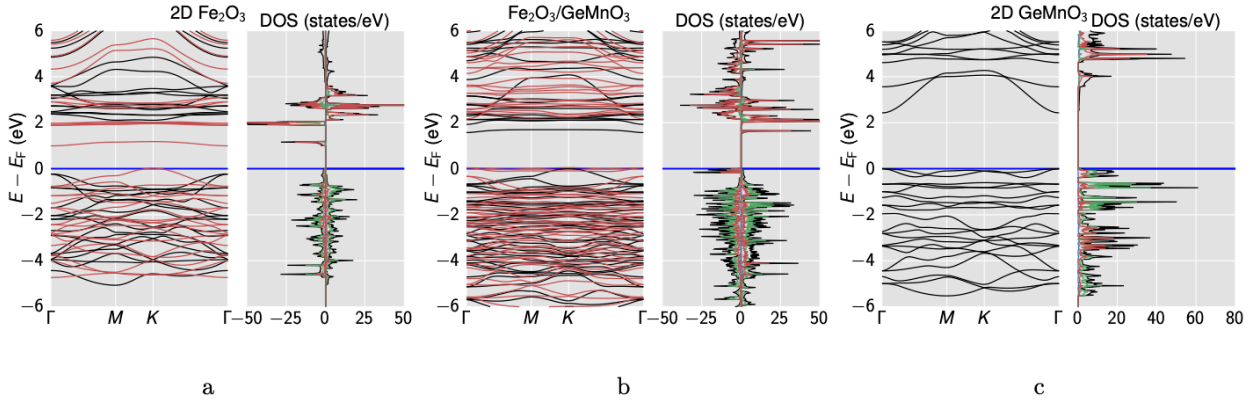


FIG. S52: Band structure and DOS for the individual 2D (a) Fe₂O₃, (c) GeMnO₃ systems, and (b) the HS. The energies are aligned at the respective Fermi energy E_F .

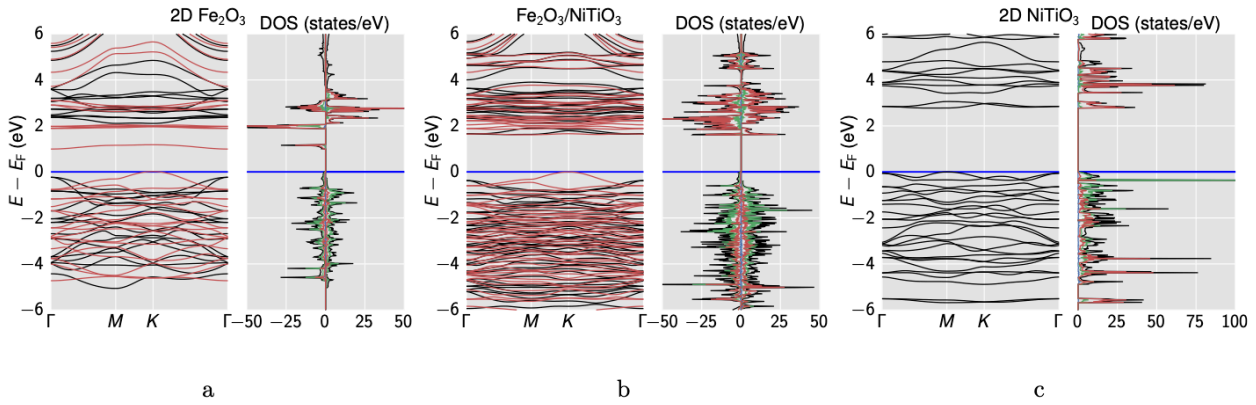


FIG. S53: Band structure and DOS for the individual 2D (a) Fe₂O₃, (c) NiTiO₃ systems, and (b) the HS. The energies are aligned at the respective Fermi energy E_F .

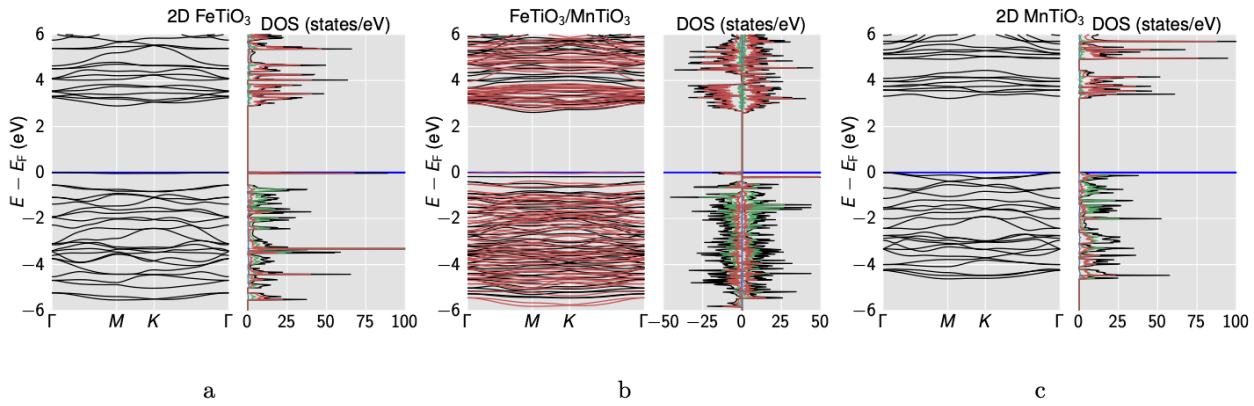


FIG. S54: Band structure and DOS for the individual 2D (a) FeTiO₃, (c) MnTiO₃ systems, and (b) the HS. The energies are aligned at the respective Fermi energy E_F .

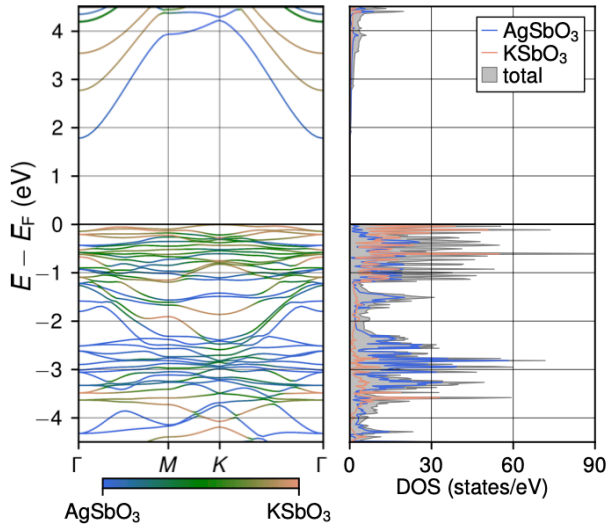


FIG. S55: Band structure and DOS with projection contributions from the atoms of each 2D sheet of AgSbO₃/KSbO₃. Note that the band structures are computed for geometries optimized with D3 dispersion correction.

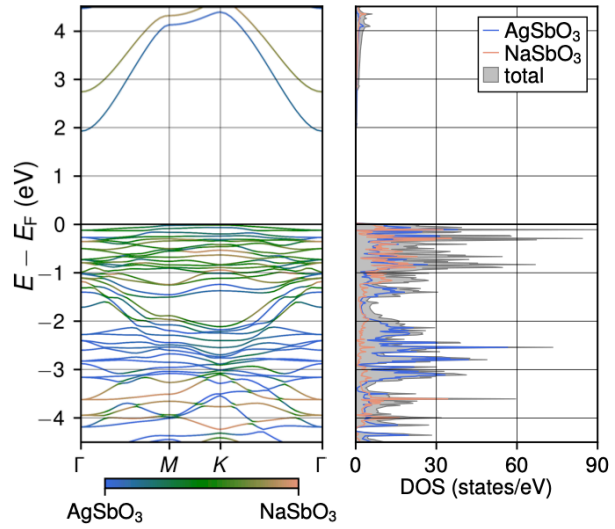


FIG. S56: Band structure and DOS with projection contributions from the atoms of each 2D sheet of AgSbO₃/NaSbO₃.

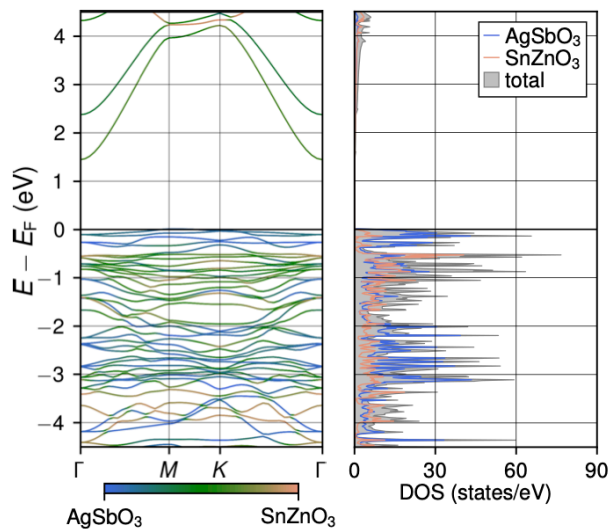


FIG. S57: Band structure and DOS with projection contributions from the atoms of each 2D sheet of $\text{AgSbO}_3/\text{SnZnO}_3$. Note that the band structures are computed for geometries optimized with D3 dispersion correction.

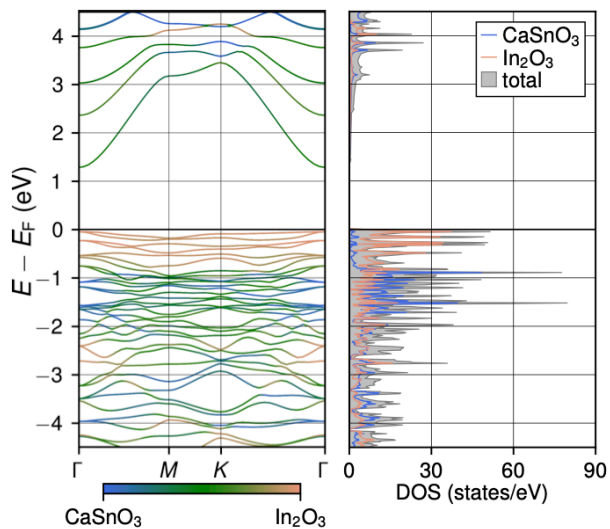


FIG. S59: Band structure and DOS with projection contributions from the atoms of each 2D sheet of $\text{CaSnO}_3/\text{In}_2\text{O}_3$.

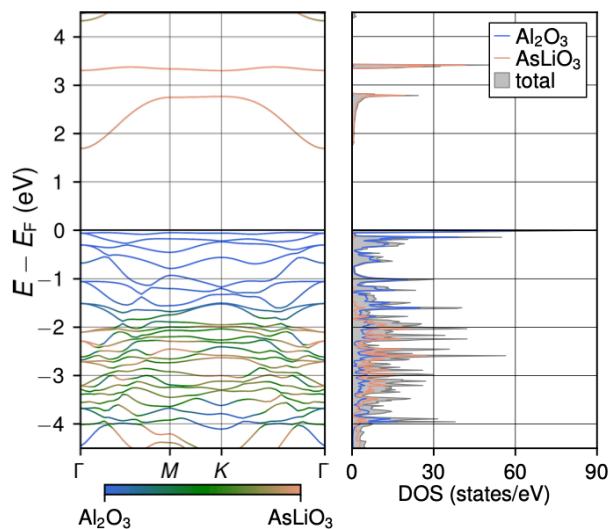


FIG. S58: Band structure and DOS with projection contributions from the atoms of each 2D sheet of $\text{Al}_2\text{O}_3/\text{AsLiO}_3$.

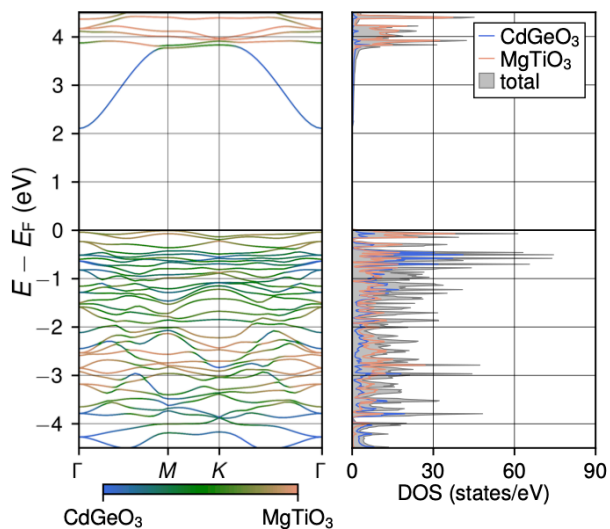


FIG. S60: Band structure and DOS with projection contributions from the atoms of each 2D sheet of $\text{CdGeO}_3/\text{MgTiO}_3$.

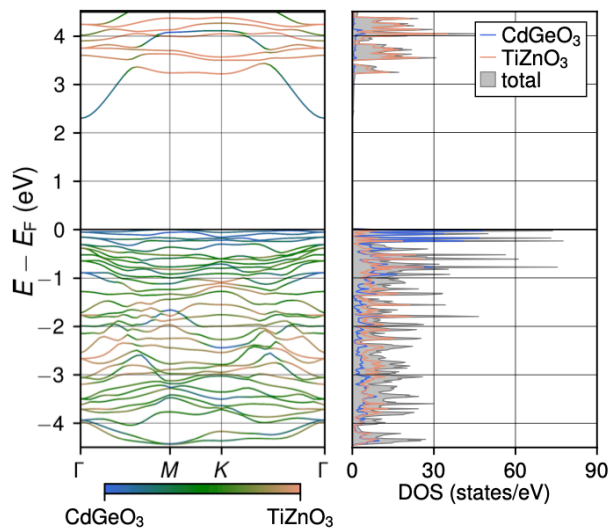


FIG. S61: Band structure and DOS with projection contributions from the atoms of each 2D sheet of CdGeO₃/TiZnO₃.

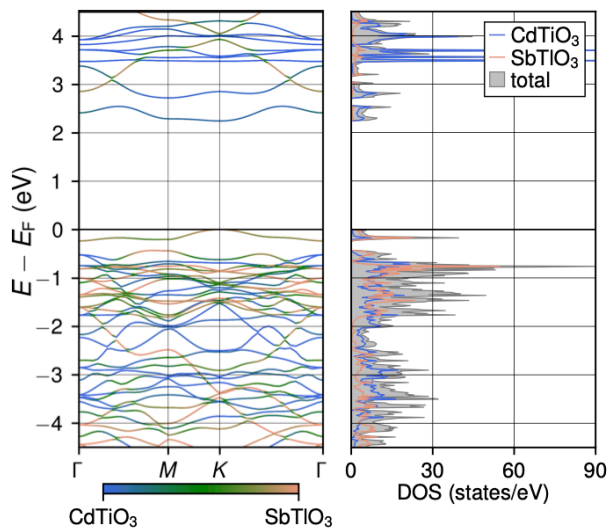


FIG. S63: Band structure and DOS with projection contributions from the atoms of each 2D sheet of CdTiO₃/SbTiO₃. Note that the band structures are computed for geometries optimized with D3 dispersion correction.

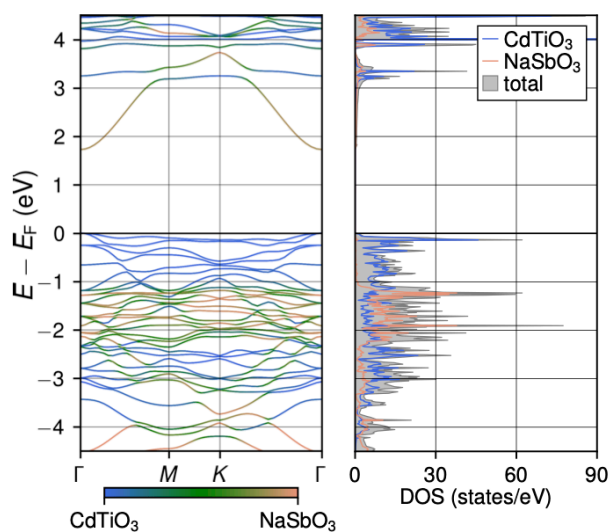


FIG. S62: Band structure and DOS with projection contributions from the atoms of each 2D sheet of CdTiO₃/NaSbO₃.

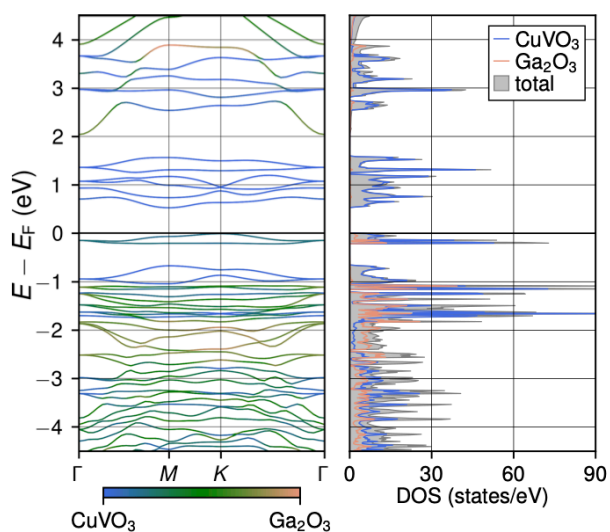


FIG. S64: Band structure and DOS with projection contributions from the atoms of each 2D sheet of CuVO₃/Ga₂O₃.

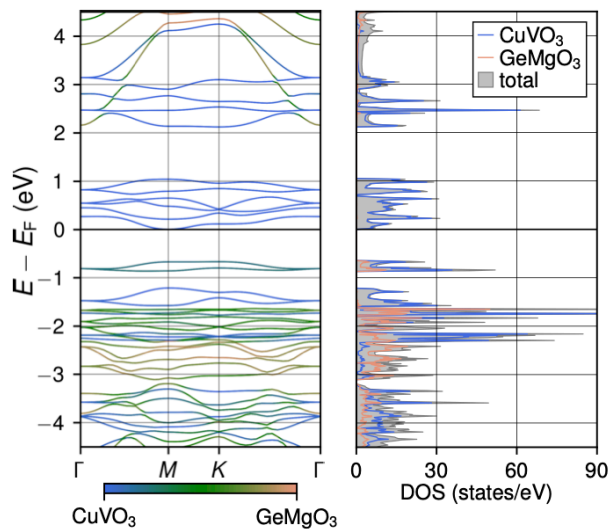


FIG. S65: Band structure and DOS with projection contributions from the atoms of each 2D sheet of $\text{CuVO}_3/\text{GeMgO}_3$.

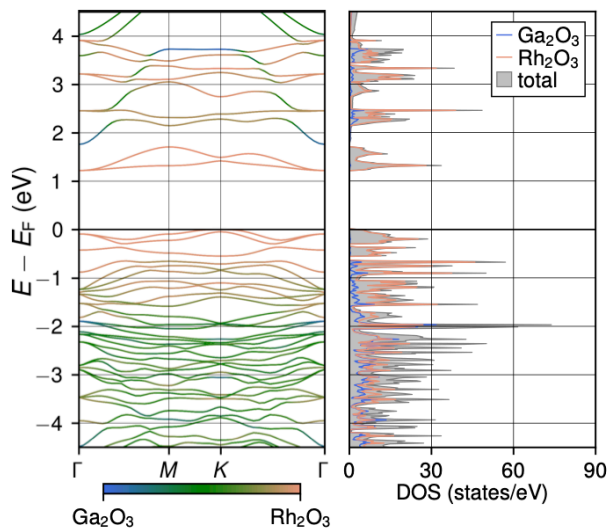


FIG. S67: Band structure and DOS with projection contributions from the atoms of each 2D sheet of $\text{Ga}_2\text{O}_3/\text{Rh}_2\text{O}_3$.

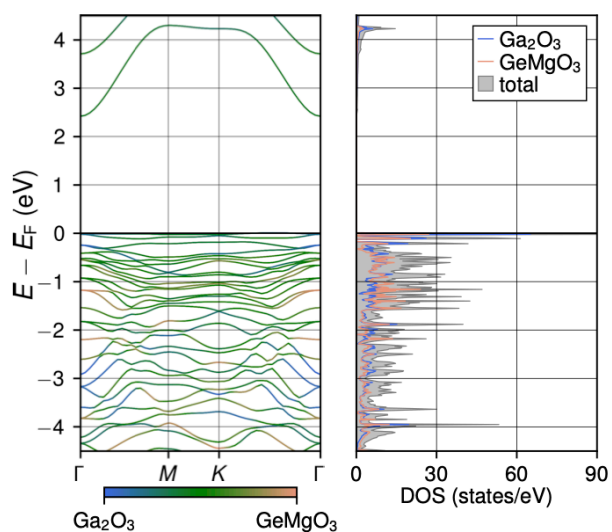


FIG. S66: Band structure and DOS with projection contributions from the atoms of each 2D sheet of $\text{Ga}_2\text{O}_3/\text{GeMgO}_3$.

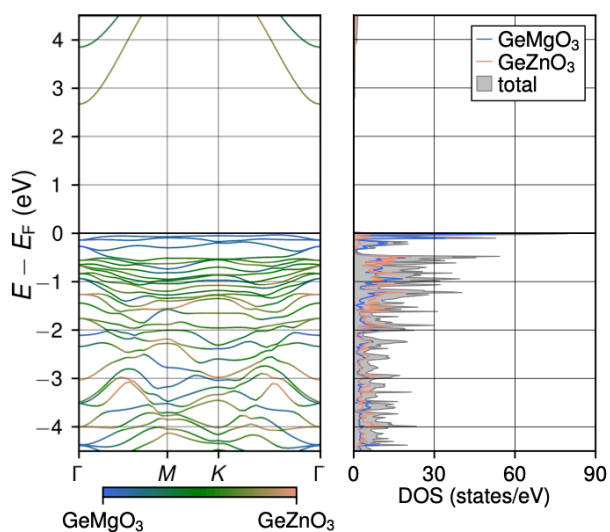


FIG. S68: Band structure and DOS with projection contributions from the atoms of each 2D sheet of $\text{GeMgO}_3/\text{GeZnO}_3$.

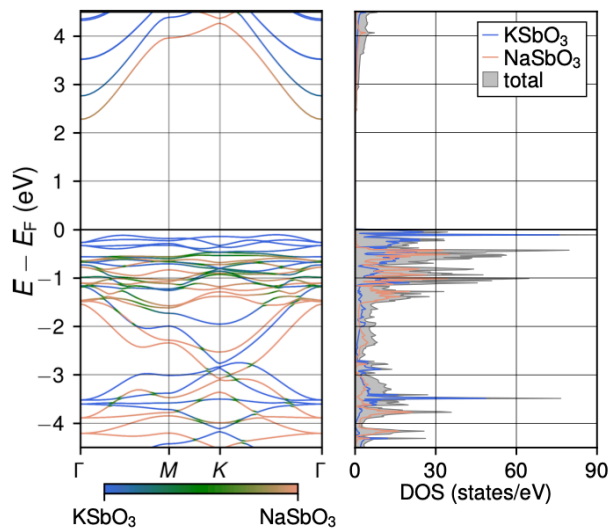


FIG. S69: Band structure and DOS with projection contributions from the atoms of each 2D sheet of $\text{KSbO}_3/\text{NaSbO}_3$.

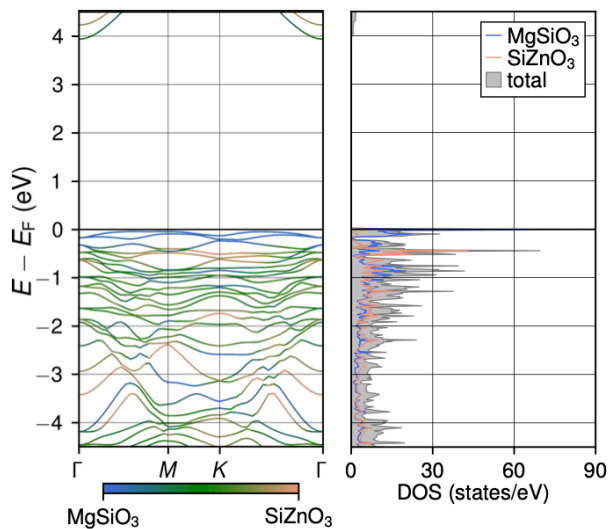


FIG. S71: Band structure and DOS with projection contributions from the atoms of each 2D sheet of $\text{MgSiO}_3/\text{SiZnO}_3$.

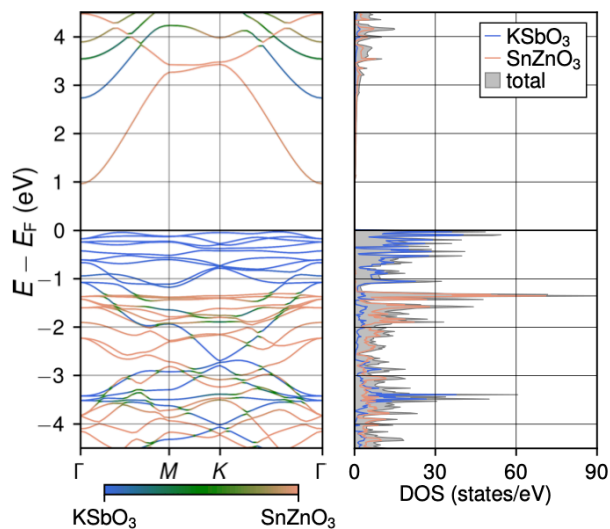


FIG. S70: Band structure and DOS with projection contributions from the atoms of each 2D sheet of $\text{KSbO}_3/\text{SnZnO}_3$. Note that the band structures are computed for geometries optimized with D3 dispersion correction.

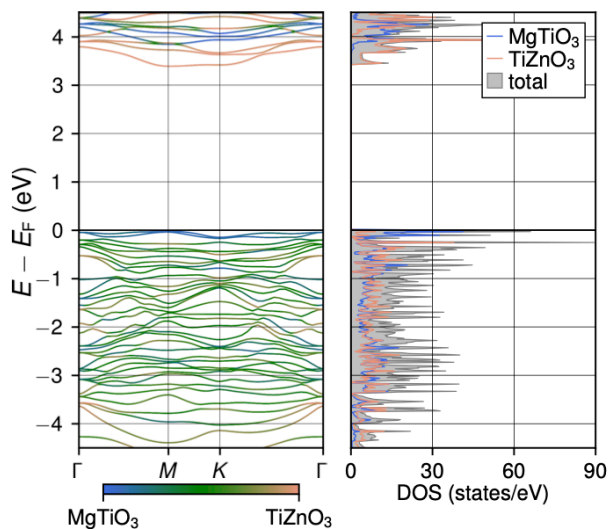


FIG. S72: Band structure and DOS with projection contributions from the atoms of each 2D sheet of $\text{MgTiO}_3/\text{TiZnO}_3$.

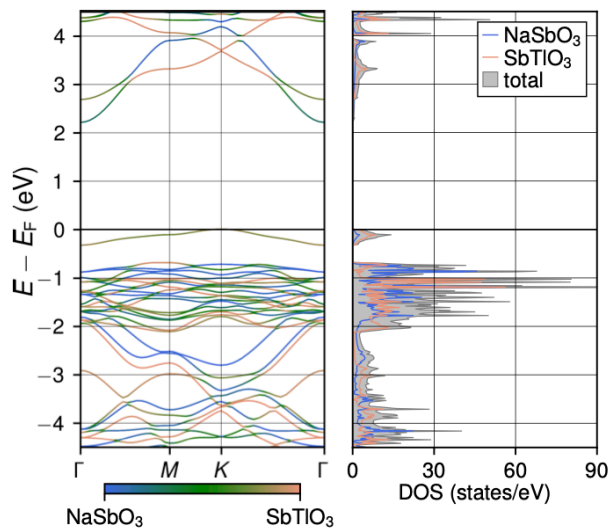


FIG. S73: Band structure and DOS with projection contributions from the atoms of each 2D sheet of NaSbO₃/SbTlO₃. Note that the band structures are computed for geometries optimized with D3 dispersion correction.

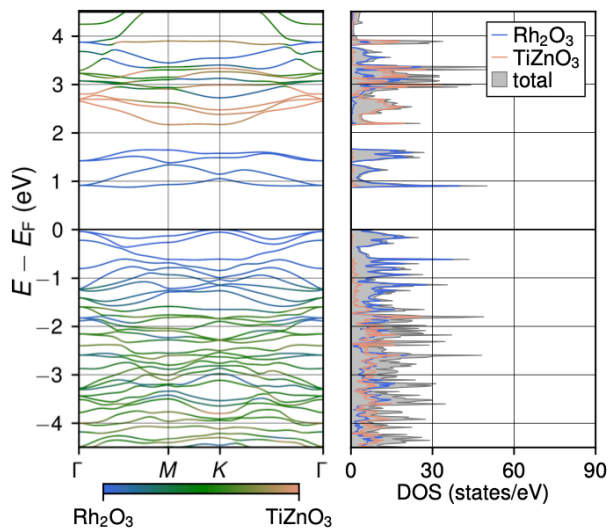


FIG. S75: Band structure and DOS with projection contributions from the atoms of each 2D sheet of Rh₂O₃/TiZnO₃. Note that the band structures are computed for geometries optimized with D3 dispersion correction.

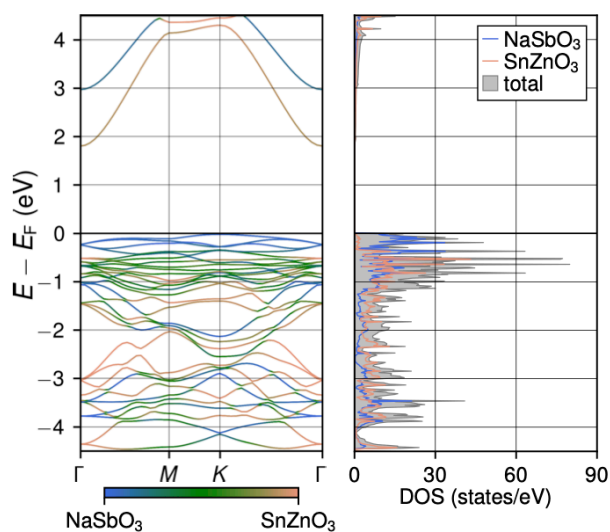


FIG. S74: Band structure and DOS with projection contributions from the atoms of each 2D sheet of NaSbO₃/SnZnO₃. Note that the band structures are computed for geometries optimized with D3 dispersion correction.

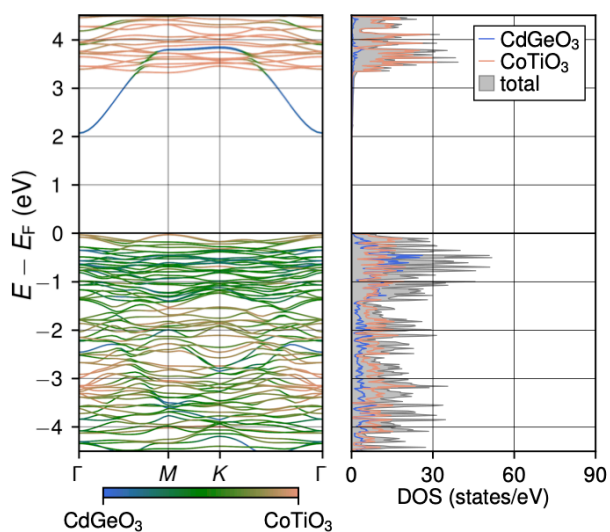


FIG. S76: Band structure and DOS with projection contributions from the atoms of each 2D sheet of CdGeO₃/CoTiO₃.

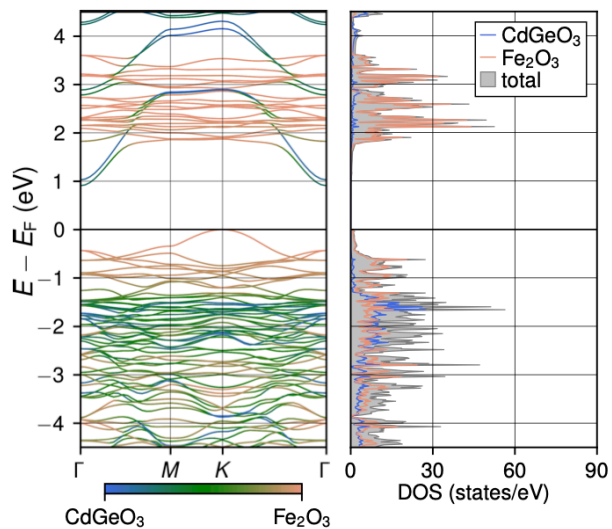


FIG. S77: Band structure and DOS with projection contributions from the atoms of each 2D sheet of CdGeO₃/Fe₂O₃.

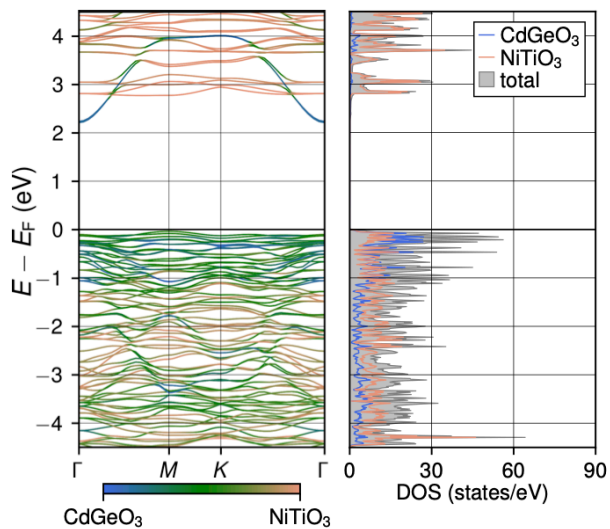


FIG. S79: Band structure and DOS with projection contributions from the atoms of each 2D sheet of CdGeO₃/NiTiO₃.

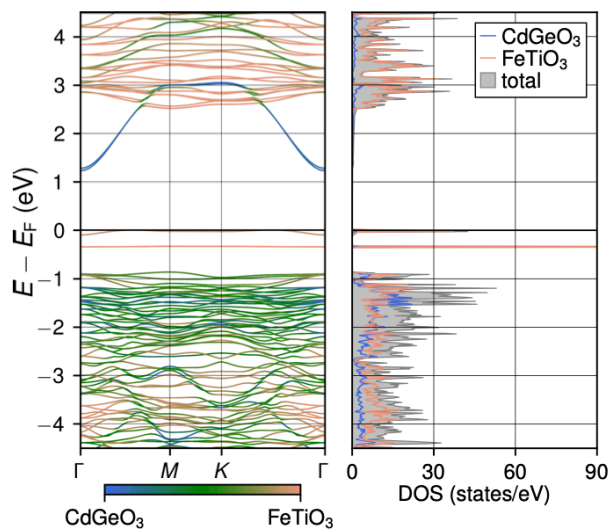


FIG. S78: Band structure and DOS with projection contributions from the atoms of each 2D sheet of CdGeO₃/FeTiO₃.

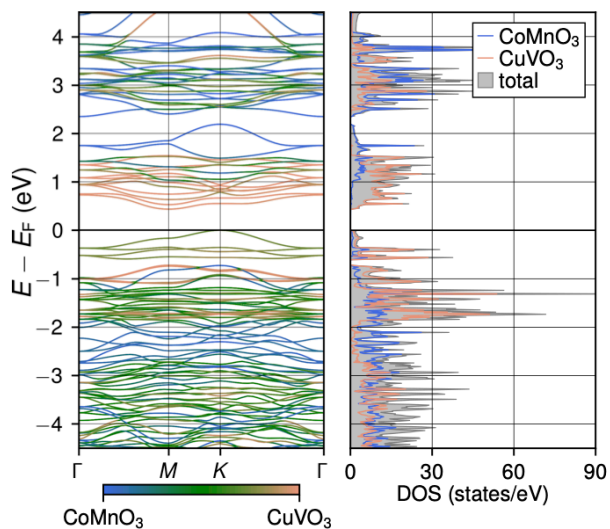


FIG. S80: Band structure and DOS with projection contributions from the atoms of each 2D sheet of CoMnO₃/CuVO₃.

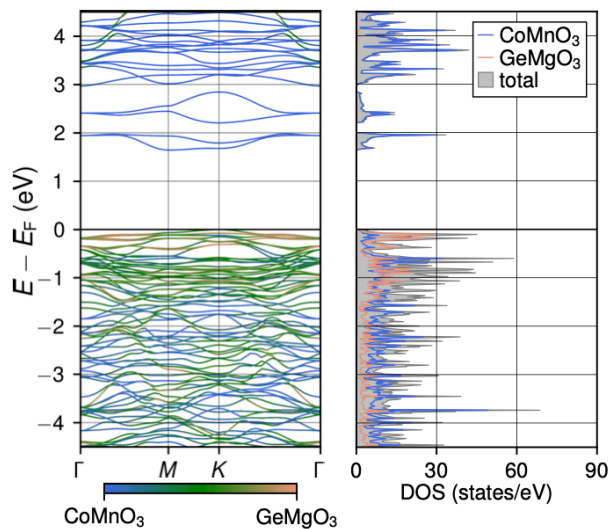


FIG. S81: Band structure and DOS with projection contributions from the atoms of each 2D sheet of CoMnO₃/GeMgO₃.

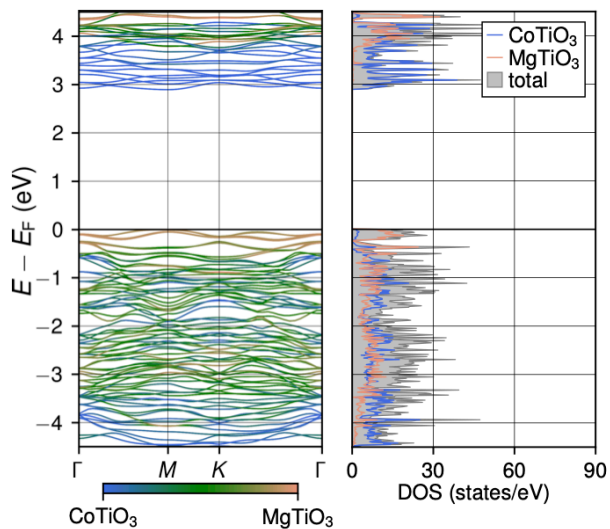


FIG. S83: Band structure and DOS with projection contributions from the atoms of each 2D sheet of CoTiO₃/MgTiO₃.

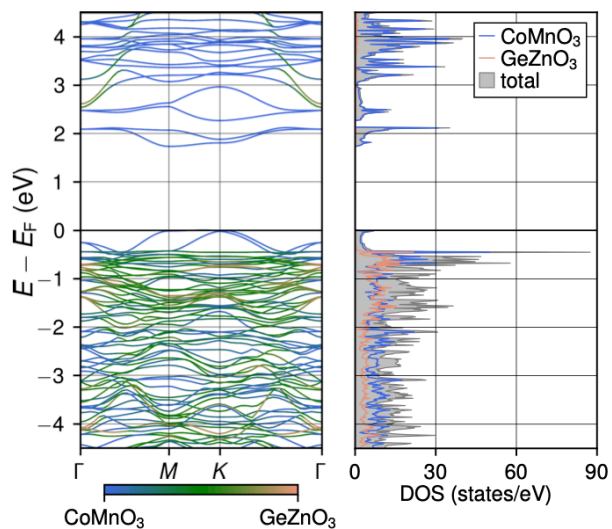


FIG. S82: Band structure and DOS with projection contributions from the atoms of each 2D sheet of CoMnO₃/GeZnO₃.

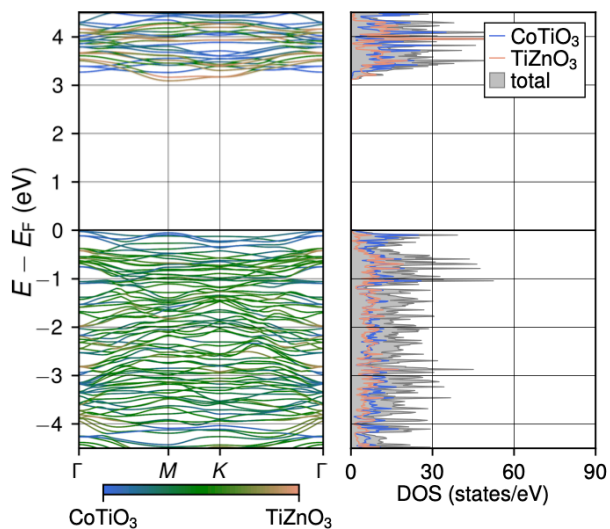


FIG. S84: Band structure and DOS with projection contributions from the atoms of each 2D sheet of CoTiO₃/TiZnO₃.

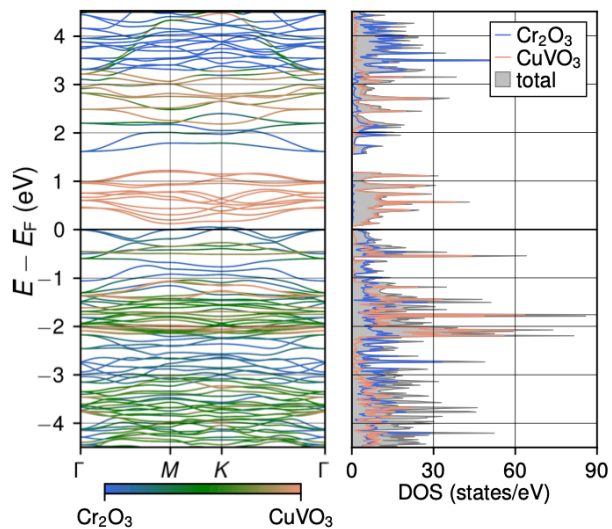


FIG. S85: Band structure and DOS with projection contributions from the atoms of each 2D sheet of $\text{Cr}_2\text{O}_3/\text{CuVO}_3$.

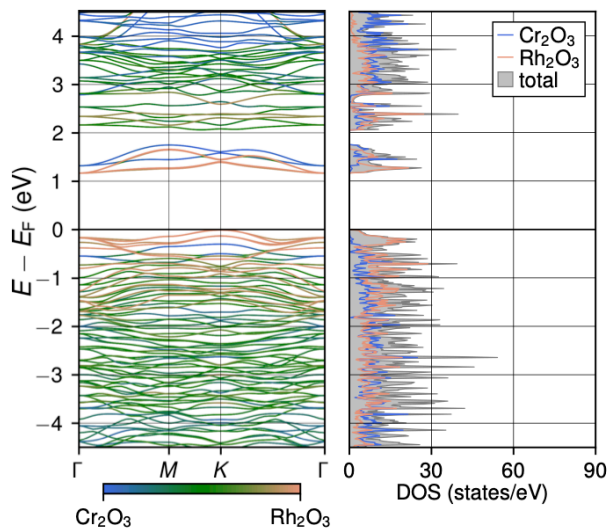


FIG. S87: Band structure and DOS with projection contributions from the atoms of each 2D sheet of $\text{Cr}_2\text{O}_3/\text{Rh}_2\text{O}_3$.

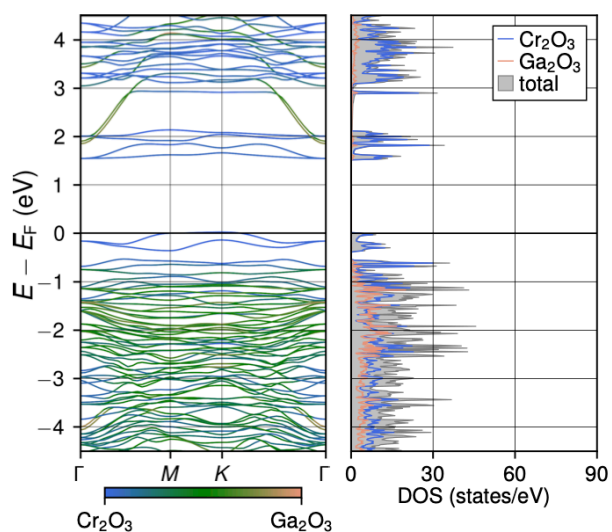


FIG. S86: Band structure and DOS with projection contributions from the atoms of each 2D sheet of $\text{Cr}_2\text{O}_3/\text{Ga}_2\text{O}_3$.

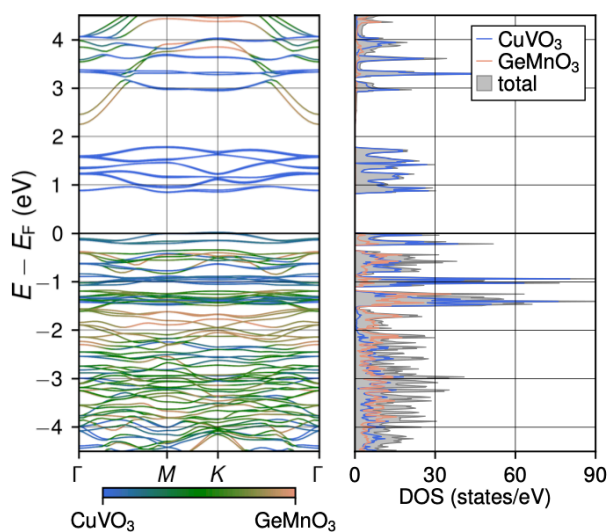


FIG. S88: Band structure and DOS with projection contributions from the atoms of each 2D sheet of $\text{CuVO}_3/\text{GeMnO}_3$.

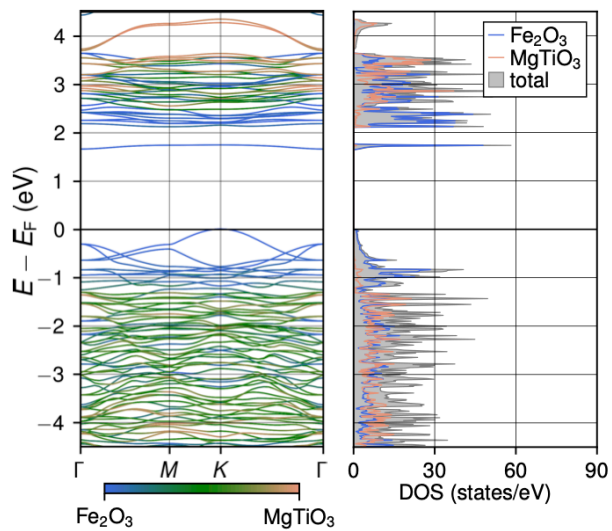


FIG. S89: Band structure and DOS with projection contributions from the atoms of each 2D sheet of Fe₂O₃/MgTiO₃.

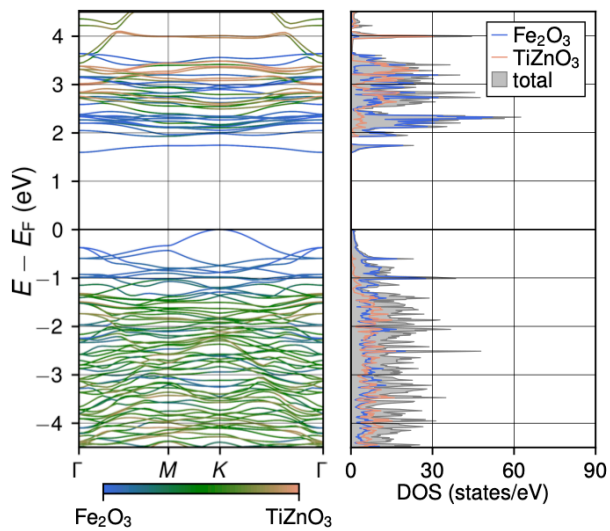


FIG. S91: Band structure and DOS with projection contributions from the atoms of each 2D sheet of Fe₂O₃/TiZnO₃.

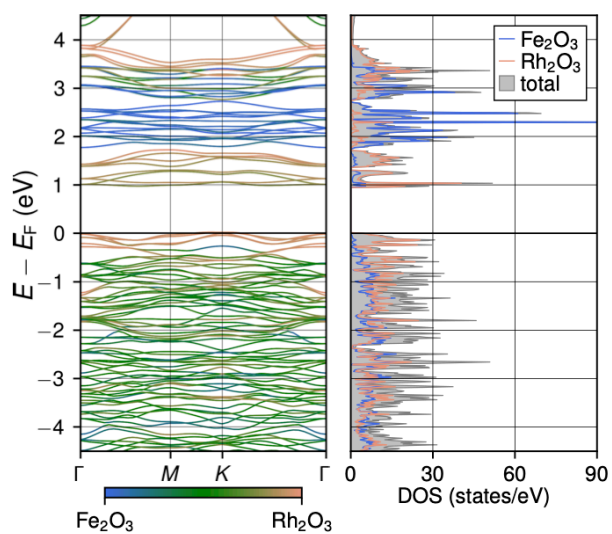


FIG. S90: Band structure and DOS with projection contributions from the atoms of each 2D sheet of Fe₂O₃/Rh₂O₃.

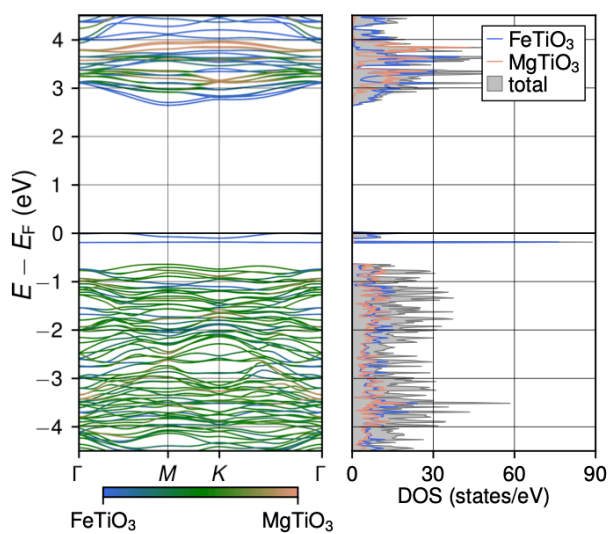


FIG. S92: Band structure and DOS with projection contributions from the atoms of each 2D sheet of FeTiO₃/MgTiO₃.

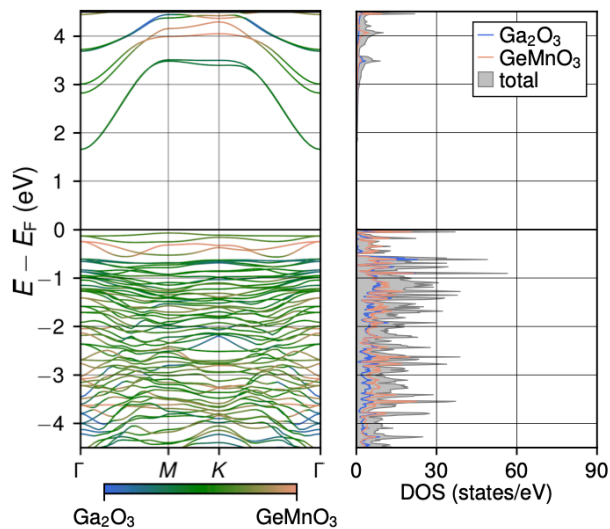


FIG. S93: Band structure and DOS with projection contributions from the atoms of each 2D sheet of $\text{Ga}_2\text{O}_3/\text{GeMnO}_3$.

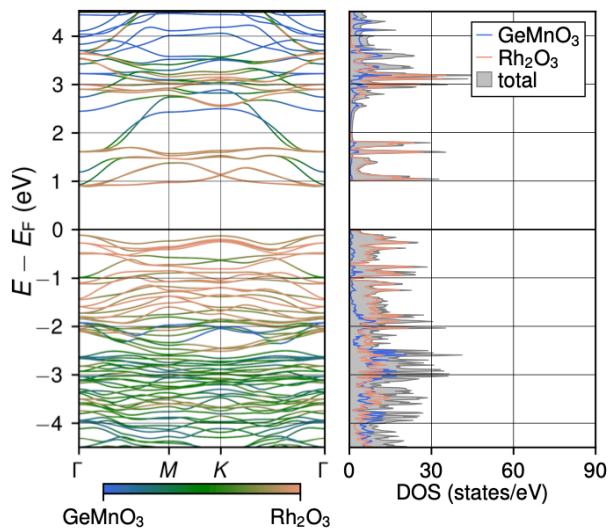


FIG. S95: Band structure and DOS with projection contributions from the atoms of each 2D sheet of $\text{GeMnO}_3/\text{Rh}_2\text{O}_3$.

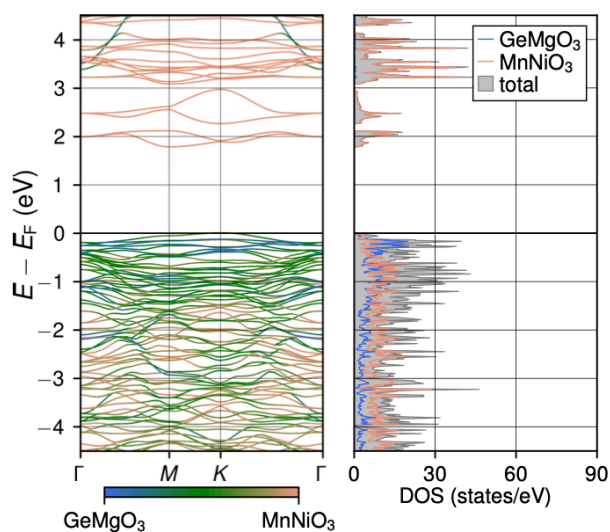


FIG. S94: Band structure and DOS with projection contributions from the atoms of each 2D sheet of $\text{GeMgO}_3/\text{MnNiO}_3$.

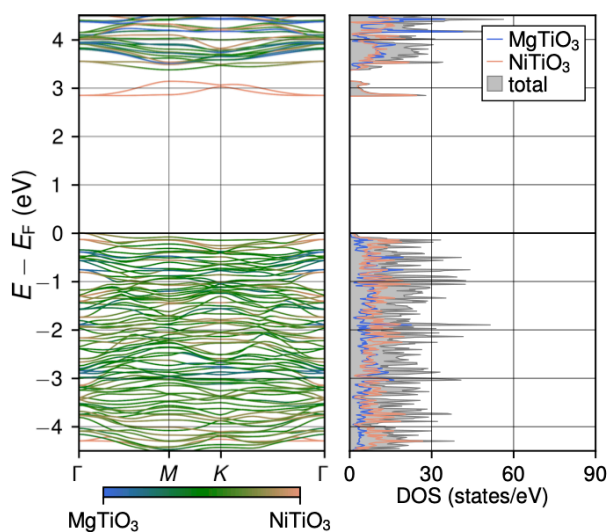


FIG. S96: Band structure and DOS with projection contributions from the atoms of each 2D sheet of $\text{MgTiO}_3/\text{NiTiO}_3$.

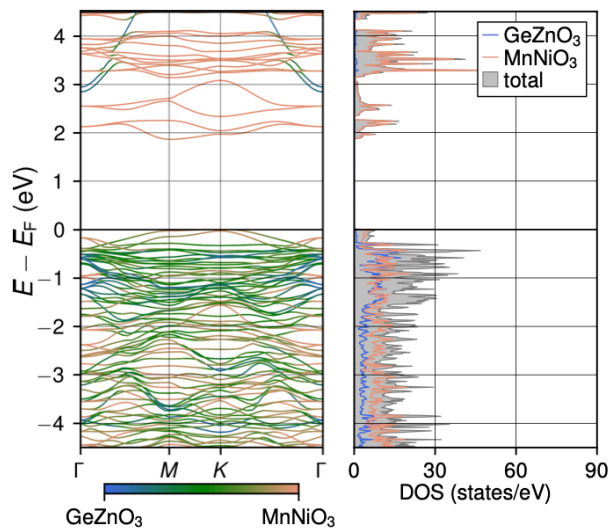


FIG. S97: Band structure and DOS with projection contributions from the atoms of each 2D sheet of MnNiO₃/GeZnO₃.

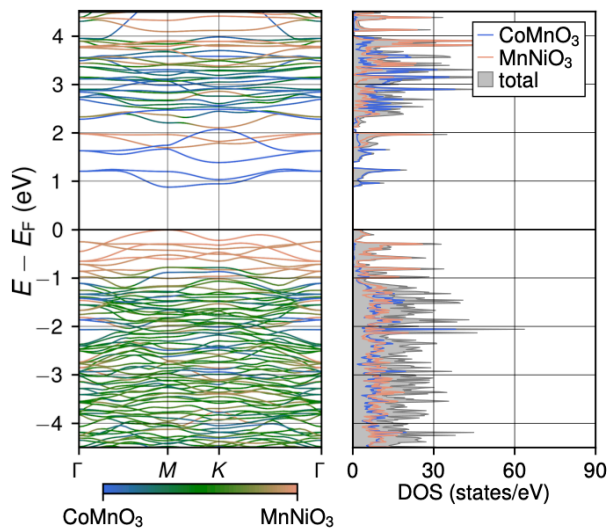


FIG. S99: Band structure and DOS with projection contributions from the atoms of each 2D sheet of CoMnO₃/MnNiO₃.

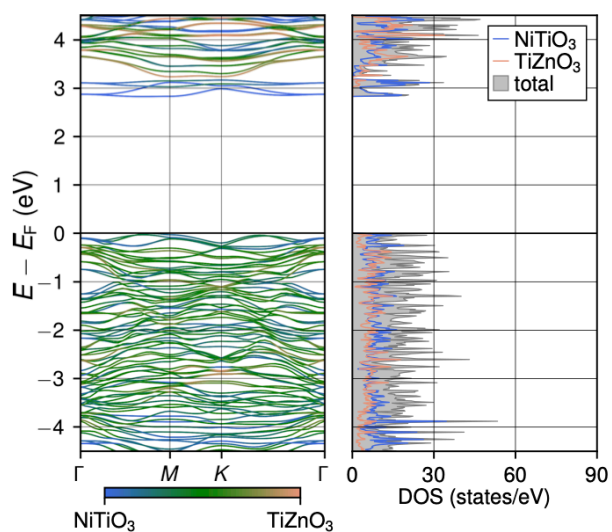


FIG. S98: Band structure and DOS with projection contributions from the atoms of each 2D sheet of NiTiO₃/TiZnO₃.

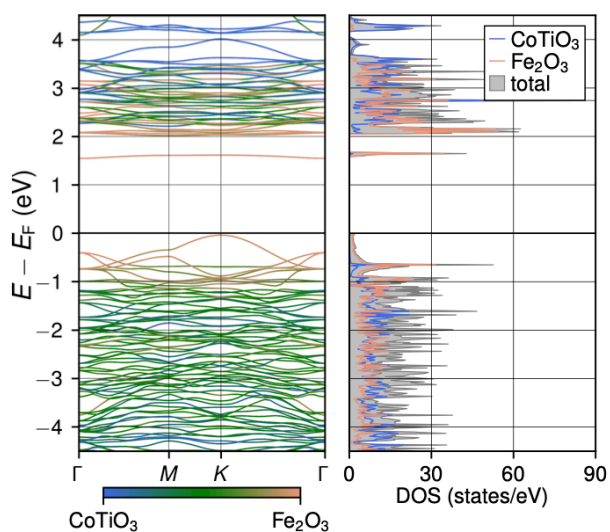


FIG. S100: Band structure and DOS with projection contributions from the atoms of each 2D sheet of CoTiO₃/Fe₂O₃.

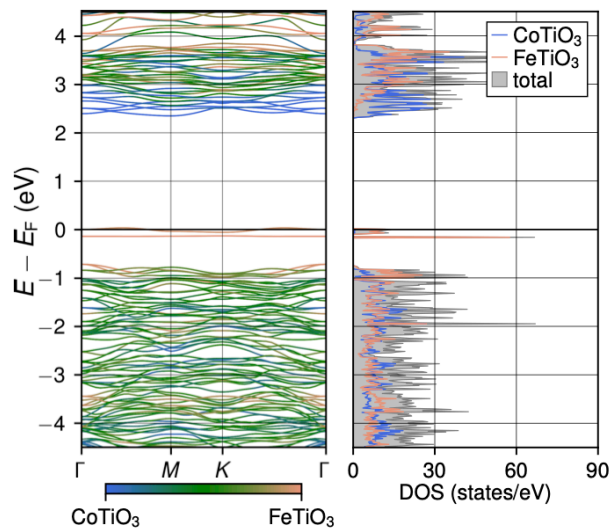


FIG. S101: Band structure and DOS with projection contributions from the atoms of each 2D sheet of CoTiO₃/FeTiO₃.

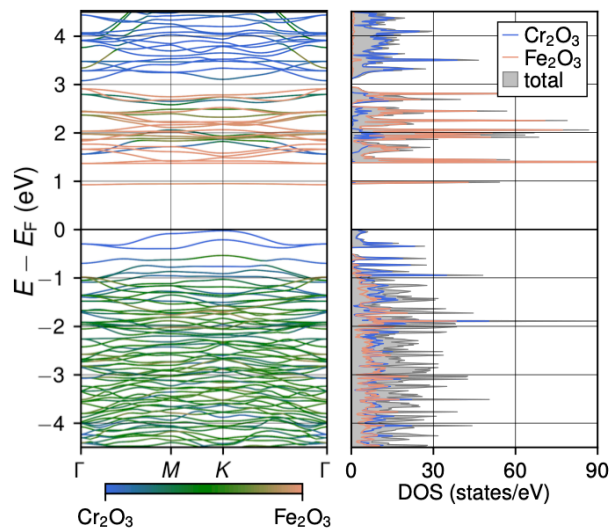


FIG. S103: Band structure and DOS with projection contributions from the atoms of each 2D sheet of Cr₂O₃/Fe₂O₃.

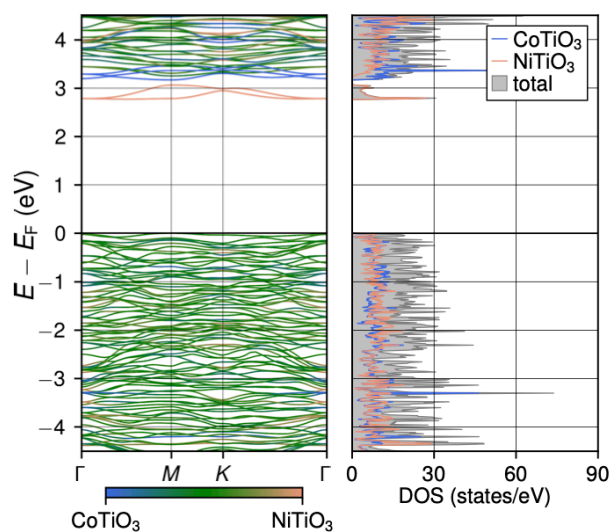


FIG. S102: Band structure and DOS with projection contributions from the atoms of each 2D sheet of CoTiO₃/NiTiO₃.

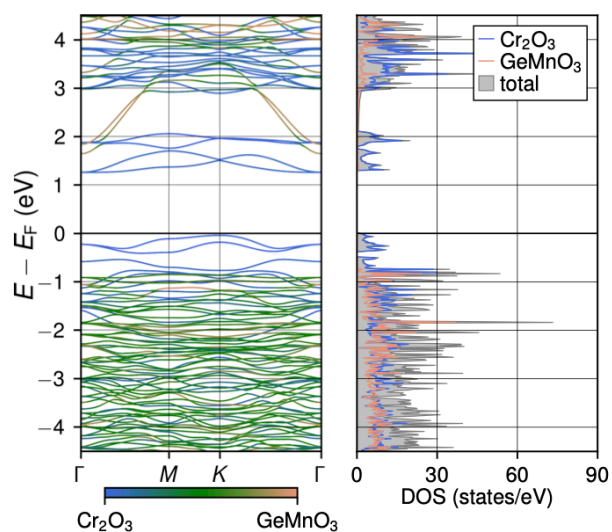


FIG. S104: Band structure and DOS with projection contributions from the atoms of each 2D sheet of Cr₂O₃/GeMnO₃.

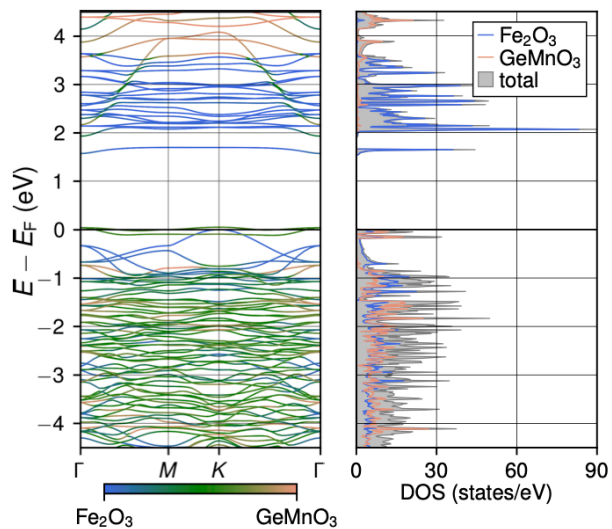


FIG. S105: Band structure and DOS with projection contributions from the atoms of each 2D sheet of $\text{Fe}_2\text{O}_3/\text{GeMnO}_3$.

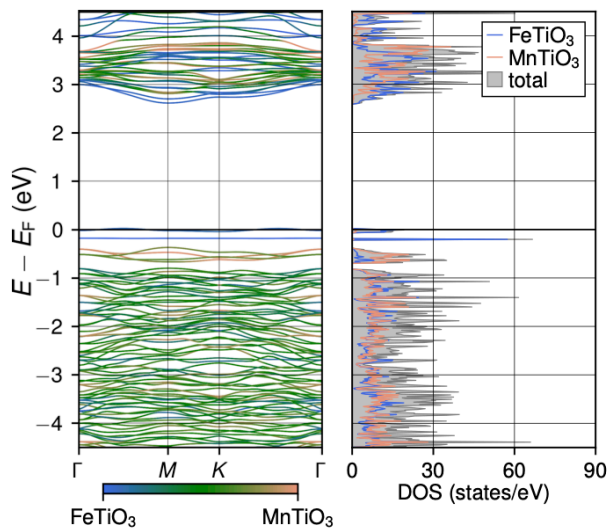


FIG. S107: Band structure and DOS with projection contributions from the atoms of each 2D sheet of $\text{FeTiO}_3/\text{MnTiO}_3$.

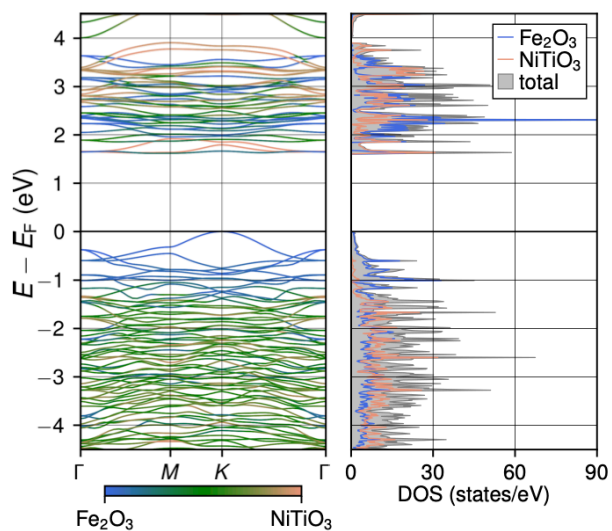


FIG. S106: Band structure and DOS with projection contributions from the atoms of each 2D sheet of $\text{Fe}_2\text{O}_3/\text{NiTiO}_3$.

IV. Charge density on the plane above the top surface for twisted HSs

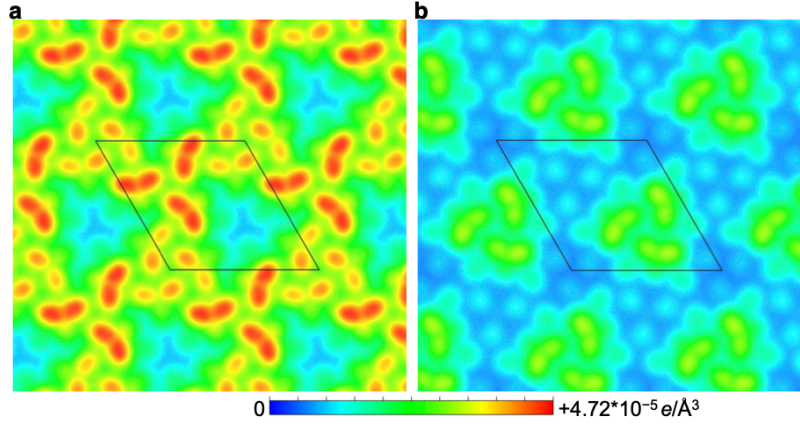


FIG. S108: (a/b) Top view of the charge density variation on a plane 3.18/3.23 Å above the top surface (above MgTiO₃) of Fe₂O₃/MgTiO₃ for 22/38°. The unit cell is indicated by the black frame.

V. Magnetisation density on the plane below the bottom surface for twisted HSs

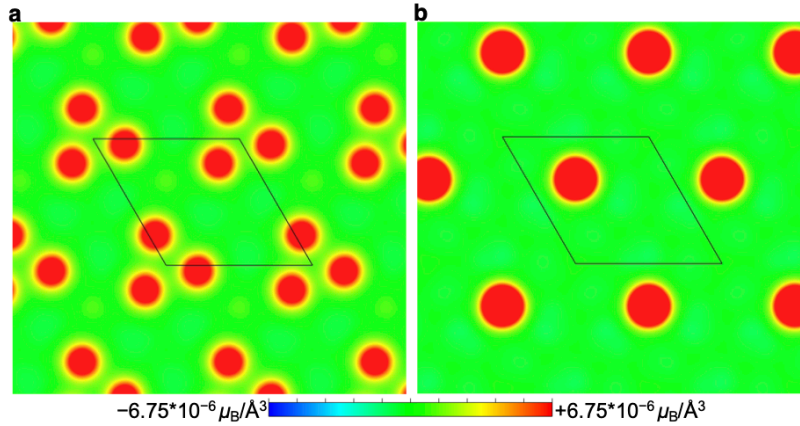


FIG. S109: (a/b) Top view of the magnetisation density variation on a plane 3.69/3.15 Å below the bottom surface (below Fe₂O₃) of Fe₂O₃/MgTiO₃ for 22/38°. The unit cell is indicated by the black frame.

-
- [1] S. Grimme, J. Antony, S. Ehrlich, and H. Krieg, *A consistent and accurate ab initio parametrization of density functional dispersion correction (DFT-D) for the 94 elements H-Pu*, J. Chem. Phys. **132**, 154104 (2010), [doi:10.1063/1.3382344](https://doi.org/10.1063/1.3382344).
- [2] J. P. Perdew, K. Burke, and M. Ernzerhof, *Generalized Gradient Approximation Made Simple*, Phys. Rev. Lett. **77**, 3865–3868 (1996), [doi:10.1103/PhysRevLett.77.3865](https://doi.org/10.1103/PhysRevLett.77.3865).
- [3] V. I. Anisimov, J. Zaanen, and O. K. Andersen, *Band theory and Mott insulators: Hubbard U instead of Stoner I*, Phys. Rev. B **44**, 943–954 (1991), [doi:10.1103/PhysRevB.44.943](https://doi.org/10.1103/PhysRevB.44.943).
- [4] A. I. Liechtenstein, V. I. Anisimov, and J. Zaanen, *Density-functional theory and strong interactions: Orbital ordering in Mott-Hubbard insulators*, Phys. Rev. B **52**, R5467–R5470 (1995), [doi:10.1103/PhysRevB.52.R5467](https://doi.org/10.1103/PhysRevB.52.R5467).
- [5] S. L. Dudarev, G. A. Botton, S. Y. Savrasov, C. J. Humphreys, and A. P. Sutton, *Electron-energy-loss spectra and the structural stability of nickel oxide: An LSDA+U study*, Phys. Rev. B **57**, 1505–1509 (1998), [doi:10.1103/PhysRevB.57.1505](https://doi.org/10.1103/PhysRevB.57.1505).
- [6] J. Sun, A. Ruzsinszky, and J. P. Perdew, *Strongly Constrained and Appropriately Normed Semilocal Density Functional*, Phys. Rev. Lett. **115**, 036402 (2015), [doi:10.1103/PhysRevLett.115.036402](https://doi.org/10.1103/PhysRevLett.115.036402).
- [7] H. Peng, Z.-H. Yang, J. P. Perdew, and J. Sun, *Versatile van der Waals Density Functional Based on a Meta-Generalized Gradient Approximation*, Phys. Rev. X **6**, 041005 (2016), [doi:10.1103/PhysRevX.6.041005](https://doi.org/10.1103/PhysRevX.6.041005).

- [8] T. Björkman, A. Gulans, A. V. Krasheninnikov, and R. M. Nieminen, *van der Waals Bonding in Layered Compounds from Advanced Density-Functional First-Principles Calculations*, Phys. Rev. Lett. **108**, 235502 (2012), [doi: 10.1103/PhysRevLett.108.235502](https://doi.org/10.1103/PhysRevLett.108.235502).